3-22-2012

FDTD Simulation of Novel Polarimetric and Directional Refelectance and Transmittance Measurements from Optical Nano- and Micro-Structured Materials

Spencer R. Sellers

FDTD SIMULATION OF NOVEL POLARIMETRIC AND DIRECTIONAL REFLECTANCE AND TRANSMITTANCE MEASUREMENTS FROM OPTICAL NANO- AND MICRO-STRUCTURED MATERIALS

THESIS

Spencer R. Sellers, Captain, USAF

AFIT/EE.ABET/ENP/12-M02

DEPARTMENT OF THE AIR FORCE
AIR UNIVERSITY

AIR FORCE INSTITUTE OF TECHNOLOGY

Wright-Patterson Air Force Base, Ohio

AFIT/EE.ABET/ENP/12-M02

FDTD SIMULATION OF NOVEL POLARIMETRIC AND DIRECTIONAL REFLECTANCE AND TRANSMITTANCE MEASUREMENTS FROM OPTICAL NANO- AND MICRO-STRUCTURED MATERIALS

THESIS

Presented to the Faculty

Department of Electrical and Computer Engineering

Graduate School of Engineering and Management

Air Force Institute of Technology

Air University

Air Education and Training Command

In Partial Fulfillment of the Requirements for the

Degree of Master of Science in Electrical Engineering

Spencer R. Sellers, BS

Captain, USAF

March 2012

AFIT/EE.ABET/ENP/12-M02

FDTD SIMULATION OF NOVEL POLARIMETRIC AND DIRECTIONAL REFLECTANCE AND TRANSMITTANCE MEASUREMENTS FROM OPTICAL NANO- AND MICRO-STRUCTURED MATERIALS

Spencer R. Sellers, BSEE
Captain, USAF

Approved:

//SIGNED//	
Michael A. Marciniak, PhD (Chairman)	Date
//SIGNED//	
Ronald A. Coutu, Jr., PhD (Member)	Date
//SIGNED//	
Milo W. Hyde, Maj (Member)	Date

Abstract

Unique scatter characteristics of nano-/micro-structured materials have been widely studied, but lacking is a focus on the off-normal incidence characteristics of this scatter. The measurements of off-normal spectral and angular scatter for a guided-mode resonant filter (GMRF) photonic crystal (PC) and a surface plasmon polariton (SPP) structure were compared to finite-difference time-domain (FDTD) simulations, as well as analytical PC and SPP theory. The GMRF is a 2-d refractive index-modulated square grating made of titanium-dioxide (TiO_2) and ultraviolet-cured polymer (UVCP) with the top and bottom covered by UVCP. Spectral off-normal un-polarized and linearly polarized transmission and bidirectional scatter distribution function (BSDF) measurements are compared to FDTD simulations to determine off-normal scatter characteristics of the filter. The GMRF is found to exhibit extraordinary angular scatter for guided-modes and off-normal incidence. An analytical expression was developed which accurately predicts the location of these modes in simulations and at the measured location for incident angle and wavelength. The SPP sample is a gold/titanium thin film (50 nm) with a 2-d square array of circular holes deposited on 1 μm of highly n-doped, n=2e18cm^{-3}, gallium-arsenide (GaAs) upon a semi-insulating GaAs substrate. Spectral extraordinary transmission measurements were made for various normal and off-normal incidence angles (θ_i) with linearly polarized and un-polarized light. The first- and second-order SPP modes and their dependence on θ_i, azimuthal angle with respect to alignment with the hole array (φ), polarization and the grating momentum vector were identified. The measurements and simulations corroborate the theoretical analysis, giving an analytical solution to the spectral location of lower-order modes. Full polarimetric spectral transmission was both measured and simulated, giving a Mueller matrix representation of the spectral transmission of the SPP structure at θ_i=0° and 20° and φ=0° and 45°, demonstrating that this structure is moderately depolarizing when resonant. These results

demonstrate the dependence on incident angle and polarization of the extraordinary characteristics of two classes of nano-/micro-structured materials.

To My Wife, My Two Daughters and My Son

Acknowledgments

First and foremost I would like to thank my wife for always believing in me and my ability to succeed in my scholastic endeavors. She has given me the motivation to succeed in ways I never thought possible. Next, I would like to thank MSgt Gary West, MSgt Whitman and TSgt Rueben Reyes for inspiring me to pursue education and helping me get accepted into the airman education commissioning program. I would also like to thank my advisor, Dr. Michael Marciniak for his guidance and mentorship. Capt. Jason Vap and Dr. Stephen Nauyoks made the measurements that enabled this research effort, their contribution was in momentous. Finally, I would like to thank my children for being patient with me during my studies.

Spencer Sellers

Table of Contents

List of Figures

Figure Page

FDTD SIMULATION OF NOVEL POLARIMETRIC AND DIRECTIONAL REFLECTANCE AND TRANSMITTANCE MEASUREMENTS FROM OPTICAL NANO- AND MICRO-STRUCTURED MATERIALS

I. Introduction

Recently, there has been a surge in nano- and micro-structured optical materials that offer special properties for the propagation, localization and control of electromagnetic (EM) radiation over a range of frequencies from the visible to the far-infrared. Among these structured materials are photonic crystals (PCs) and surface plasmon polariton (SPP) structures; these are the focus of this thesis.

PCs and SPP structures have been proposed for a variety of new concepts such as optical computing, optical communications, alternate energy and heat management. Waveguides are an application of these structures which provides the basis for optical computing. Optical computing utilizes photon, rather than electron, switching for logic processes. This form of computing is potentially much faster and offers a much broader bandwidth then current computing. These structures also provide the capability to make very fine line width and voltage-tunable optical filters. These are critical components in full optical communication applications. PCs and SPP structures can also be designed into selective thermal emitters which provide applications in heat management and improvement in harnessing solar energy. By designing a thermal emitter tuned to match

the absorption spectrum of photovoltaic cells, the efficiency of solar energy production can be improved over existing designs.

All these applications and others for which these structures have been proposed are listed among the essential focus areas for Air Force science and technology investment in the "Technology Horizons 2010-2030" report [1].

Problem Statement

If the phenomena of these structures can be generalized, it may be possible to extend these unique properties to the ultraviolet or even x-ray or gamma ray. However, while there are many theoretical publications on nano-/micro-structured materials, there are relatively few experimental papers discussing the performance of these structures in operational environments, and the behavior that is reported for fabricated structures is often only for very limited experimental conditions. Specifically, an area of research in the nano-/micro-structured materials field that has not been extensively considered is the hemispherical polarimetric scatter and scatter distribution of these materials, especially for off-normal incidence. Most literature presents an engineered material and gives normal incidence reflectance or transmittance measurements only [2-7]. Before war fighter applications of these materials can be considered, the basic physics of the structures proposed theoretically must be characterized through measurement and simulation to fully understand their scatter dependence on polarization and angle of incidence.

Methodology

This research effort reviews two optical nano-/micro-structured materials and simulates these structures using a finite difference time domain (FDTD) model to predict the off-normal incidence scatter. The rigorously determined scatter is then compared against specific measurements to validate the simulation. The simulations and measurements are then used to assign physical phenomena to the unique off-normal characteristics identified.

Overview

Chapter II gives a background for the theory and characteristics of PCs and SPP structures with an emphasis on the samples being examined in this thesis. Also included in the background is an explanation of the finite difference time domain (FDTD) and the commercial software, Lumerical Solution's FDTD solver, which was used as an analysis tool to determine off-normal scatter from these structures. Finally, an overview of the measurement instruments used is presented. Chapter III focuses on the analysis and measurements of a guided-mode resonant filter (GMRF) PC. The measurements and unique characteristics of this structure are presented, followed by the FDTD simulation and findings. Chapter IV focuses on the analysis and measurements of an SPP extraordinary transmission filter. The measurements are presented, an analytical expression is developed to describe the off-normal characteristics of this transmission, and FDTD simulations are utilized to complete analysis. Chapter V concludes this thesis and examines the areas of future work.

II. Background

This chapter provides a review of physical phenomena which describe both the design and behavior of the nano-/micro-structured materials studied in this research. An overview of photonic crystals (PCs), photonic bandgaps (PBGs) and surface plasmon polaritons (SPPs) is presented. The finite difference time domain (FDTD) method for electromagnetic (EM) modeling is reviewed and a description of Lumerical Solutions' FDTD software is given. The use of the bidirectional scatter distribution function (BSDF), which describes the full angular scatter characteristics of materials, was used heavily in this research; therefore, a review of it is provided, including that of fully polarimetric BSDF. Finally, the subset of AFIT's Optical Scatter Laboratory measuring instruments used in this research is described.

Photonic Crystals and Bandgaps

Photonic crystals (PCs) are dielectric structures with periodically modulated refractive indices. These structures are both naturally occurring and man-made. The refractive index distribution, $n(\vec{r}) = [\varepsilon(\vec{r})]^2$, where ε is the electric permittivity and $\vec{r}$ is the position vector, forms a lattice which is analogous to a crystal lattice in a semiconductor. Due to the periodicity, solutions to Maxwell's equations for a periodic ε describe the propagation of EM waves within the PC and provide the allowed wavelengths λ and propagation vectors $\vec{k}$. Wavelengths and propagation vectors that are allowed to propagate form modes and groups of modes form bands, referred to as pass bands. If a group of modes is forbidden from propagating through the structure, it is called a stop band. These band relations are usually represented in a band diagram as a

dispersion relation, or the dependence of the propagation vector, $\vec{k}$ or $\vec{\beta}$, on optical frequency, ω. The Maxwell-Faraday equation and Ampère's circuital law are used to describe the propagation of EM waves within a PC made up of non-magnetic, isotropic, periodically modulated dielectrics

$$\begin{aligned} \nabla \times \vec{E} &= -\frac{1}{c}\frac{\partial}{\partial t}\vec{H} = i\frac{\omega}{c}\vec{H} \\ \nabla \times \vec{H} &= \varepsilon(\vec{r})\frac{1}{c}\frac{\partial}{\partial t}\vec{E} = -i\frac{\omega}{c}\varepsilon(\vec{r})\vec{E} \end{aligned} \tag{2.1}$$

where $\vec{E}$ is the electric field, $\vec{H}$ is the magnetic field, c is the speed of light and t is time. Combining these yields

$$\nabla \times \frac{1}{\varepsilon(\vec{r})}\nabla \times \vec{H} = \left(\frac{\omega}{c}\right)^2 \vec{H} \tag{2.2}$$

referred to as the Helmholtz equation. $\nabla \times \frac{1}{\varepsilon(\vec{r})}\nabla \times$ is the eigen-operator and is a Hermetian for lossless media, $(\omega/c)^2$ is the eigen-value and $\vec{H}$ is the eigen-state. There is also a constraint on the Helmholtz equation given by Gauss' law

$$\nabla \cdot \vec{H} = 0 \tag{2.3}$$

If an eigen-operator is periodic, like this one is, then the Bloch-Floquet theorem applies, given by

$$\vec{H}(\vec{r},t) = e^{i(\vec{k}\cdot\vec{r}-\omega t)}\vec{u}_{\vec{k}}(\vec{r}) \tag{2.4}$$

where $\vec{u}_{\vec{k}}(\vec{r}) = \vec{u}_{\vec{k}}(\vec{r}+\Lambda_{\vec{r}})$ is the periodic envelope and $\Lambda_{\vec{r}}$ is the period in the direction of $\vec{r}$. The first Brillouin zone is a uniquely defined primitive cell in $\vec{k}$ space surrounding the $\vec{k}=0$ point. The Bloch-Floquet theorem implies that any wave vector $\vec{k}'$ outside the

first Brillouin zone is equivalent to some wave vector $\vec{k}$ inside the zone translated by the reciprocal lattice vector $\vec{G} = \hat{r}\frac{2\pi}{\Lambda_{\vec{r}}}$ where $\hat{r}$ is the unit vector in the direction of $\vec{r}$, *i.e.*

$$\vec{k}' = \vec{k} + \vec{G} \tag{2.5}$$

Inserting Equation (2.4) into (2.2) and neglecting the time harmonic terms gives

$$(i\vec{k} + \nabla) \times \left[\frac{1}{\varepsilon(\vec{r})} \left(i\vec{k} + \nabla \right) \right] \times \vec{u}_{\vec{k}} = \bar{\omega}^2 \vec{u}_{\vec{k}} \tag{2.6}$$

where $\bar{\omega} = \omega / c$ is the normalized frequency. This eigenvalue equation can be solved for the dispersion relation of a PC [8]. Figure 1 shows an example of the dispersion relation of a 1-d PC made up of two different dielectrics of the same thickness. The bottom diagram shows a schematic of the structure. The shaded regions are stop bands and the white region is the pass band, defining where a photon with specific λ and $\vec{k}_z$ can propagate within the PC. The ability to engineer these pass bands and stop bands allows PCs to be used in many optical device applications.

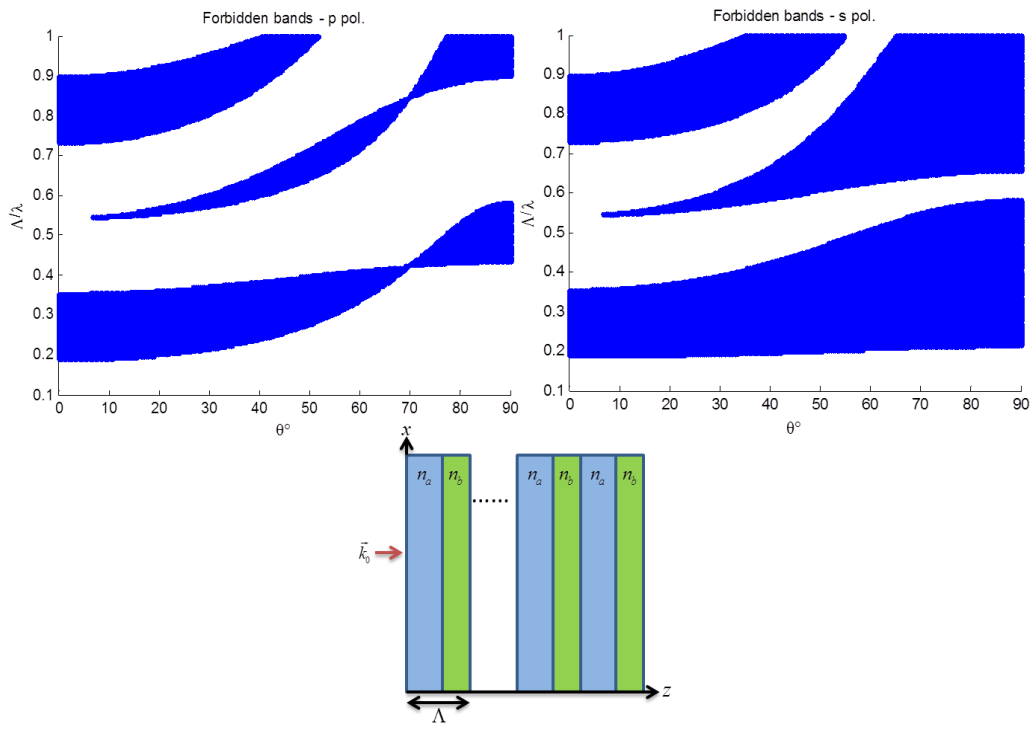

Figure 1. Example Bandgap diagram for 1-d photonic crystal with modulated dielectrics. The plot on the left is for p-polarization, the right plot is for s-polarization and the bottom diagram shows a schematic of the 1-d PC [9]**.**

Surface Plasmon Polaritons

Surface plasmon polaritons (SPPs) are EM surface waves that are evanescently confined to the surface of a metal-dielectric interface. To present this discussion in a general form, it is best to start with a cursory review of Maxwell's equations and the wave equation. Maxwell's equations in differential form are

$$\nabla \cdot \vec{D} = \rho_{ext} \tag{2.7}$$

$$\nabla \cdot \vec{B} = 0 \tag{2.8}$$

$$\nabla \times \vec{E} = -\frac{\partial \vec{B}}{\partial t} \tag{2.9}$$

$$\nabla \times \vec{H} = \vec{J}_{ext} + \frac{\partial \vec{D}}{\partial t} \tag{2.10}$$

The four macroscopic fields linked by these equations are the dielectric displacement $\vec{D}$, the electric field $\vec{E}$, the magnetic field $\vec{H}$ and the magnetic flux density $\vec{B}$. Consider two semi-infinite nonmagnetic media with local, frequency-dependent dielectric functions ε_1 and ε_2 separated by a planar surface at $z = 0$, shown in Figure 2. In the absence of external forces, Equations (2.7)-(2.10) can be expressed as

$$\nabla \times \vec{H}_j = \varepsilon_j \frac{1}{c} \frac{\partial}{\partial t} \vec{E}_j \tag{2.11}$$

$$\nabla \times \vec{E}_j = -\frac{1}{c} \frac{\partial}{\partial t} \vec{H}_j \tag{2.12}$$

$$\nabla \cdot (\varepsilon_j \vec{E}_j) = 0 \tag{2.13}$$

$$\nabla \cdot \vec{H}_j = 0 \tag{2.14}$$

where $j = 1$ for $z < 0$ and 2 for $z > 0$. Equations (2.11)-(2.14) can be classified into TM polarized and TE polarized modes.

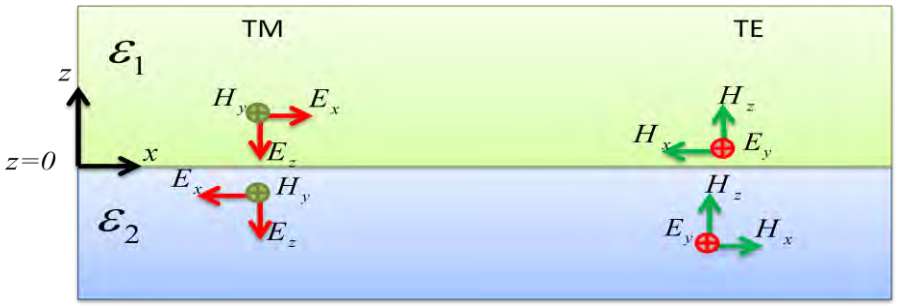

Figure 2. SPP graphical representation of interface between two media with dielectric functions ε_1 and ε_2 separated by a planar interface at $z = 0$.

For TM polarized modes, the electric field is perpendicular to the interface. It is parallel for TE polarized modes. If the interface is assumed to be ideal, then for wave propagation along it, there must be an electric field component normal to the surface; therefore, TE polarized surface oscillations do not exist. To find conditions that allow propagation along the interface (along the x-axis), consider TM polarized modes where the magnetic field is parallel to the interface.

$$\vec{E}_j = (E_{x,j}, 0, E_{z,j}) e^{-k_j|z|} e^{i(\beta_j x - \omega t)} \tag{2.15}$$

$$\vec{H}_j = (0, H_{y,j}, 0) e^{-k_j|z|} e^{i(\beta_j x - \omega t)} \tag{2.16}$$

where $E_{x/z,j}$ is the component of $\vec{E}_j$ in the x/z direction, $H_{y,j}$ is the component of $\vec{H}_j$ in the y direction and $\beta_j \equiv k_{x,j} (j = 1,2)$ is the propagation constant that represents the magnitude of the wave vector parallel to the surface; and $k_j \equiv k_{z,j}$ is the component of the wave vector perpendicular to the surface and its reciprocal defines the evanescent decay length, quantifying the confinement of the waves to the surface. Inserting (2.15) and (2.16) into (2.11)-(2.14) yields

$$ik_1 H_{y,1} = \frac{\omega}{c} \varepsilon_1 E_{x,1} \tag{2.17}$$

$$ik_2 H_{y,2} = -\frac{\omega}{c} \varepsilon_2 E_{x,2} \tag{2.18}$$

where $k_j = \sqrt{\beta_j^{\,2} - \varepsilon_j \frac{\omega^2}{c^2}}$. Applying boundary conditions at the interface which demand that the electric and magnetic fields are continuous across it gives

$$\frac{k_1}{\varepsilon_1} H_{y,1} + \frac{k_2}{\varepsilon_2} H_{y,2} = 0 \tag{2.19}$$

$$H_{y,1} - H_{y,2} = 0 \tag{2.20}$$

which only have a solution if

$$\frac{\varepsilon_1}{k_1} + \frac{\varepsilon_2}{k_2} = 0 \tag{2.21}$$

This is the surface-plasmon condition [10]. From the boundary conditions, it also follows that $\beta_1 = \beta_2 = \beta$ which yields

$$\beta(\omega) = \frac{\omega}{c}\sqrt{\frac{\varepsilon_1 \varepsilon_2}{\varepsilon_1 + \varepsilon_2}} \tag{2.22}$$

Now consider the Drude model for a semi-infinite metal in a vacuum (*i.e.* $\varepsilon_2 = 1$) [11]

$$\varepsilon_1 = 1 - \frac{{\omega_p}^2}{\omega(\omega + i\omega_\tau)} \tag{2.23}$$

where ω_p is the plasma frequency of the metal and ω_τ is the collision frequency and is much smaller than the plasma frequency. For this case, using Equation (2.22), the dispersion relation is

$$\beta(\omega) = \frac{\omega}{c}\sqrt{\frac{\omega^2 - {\omega_p}^2}{2\omega^2 - {\omega_p}^2}} \tag{2.24}$$

shown in Figure 3 for $\omega_p = 15eV$ [6]. The green dashed line represents the light line at $\omega = c\beta$ and the dotted line represents the classical non-dispersive, or non-retarding, surface plasmon frequency ($\omega_s = \omega_p / \sqrt{2}$). The lower line is the SPP frequency,

$$\omega^2(\beta) = \frac{{\omega_p}^2}{2} + c^2\beta^2 - \sqrt{\frac{{\omega_p}^4}{4} + c^4\beta^4} \tag{2.25}$$

which, in the retarded region of $\beta < \omega_s / c$, can couple with the free EM field.

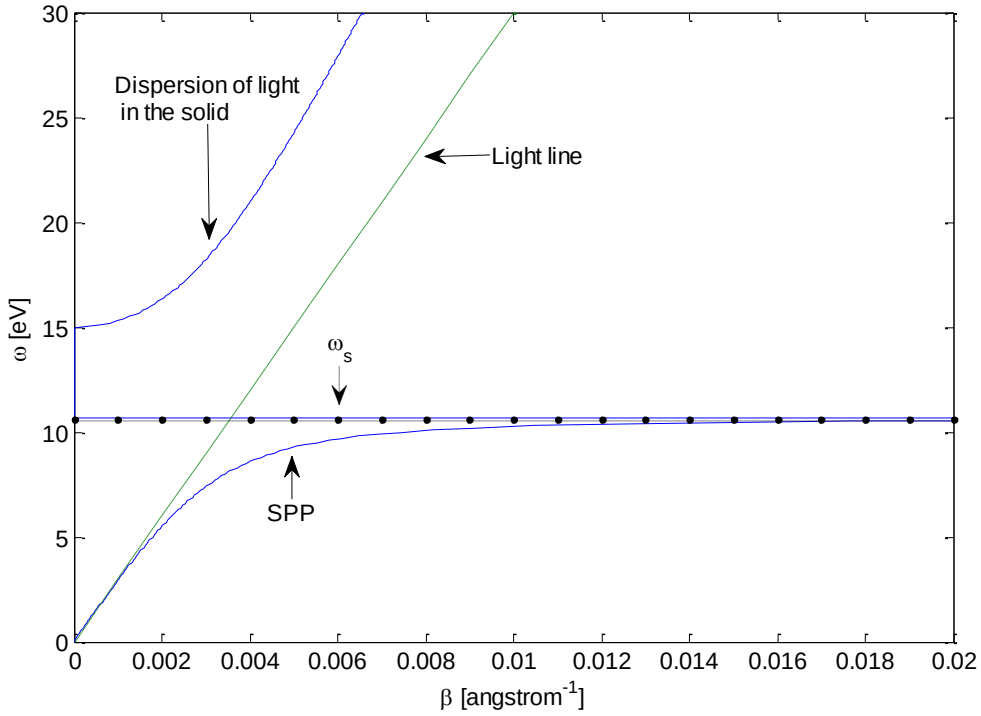

Figure 3. Dispersion diagram for a metal with plasma frequency (ω_p), 15eV. The dashed green line is the light line. The dotted line represents the non-dispersive plasma frequency (ω_s). The upper line is the dispersion of light in the solid and the lower line is the SPP frequency.

Note that the wave vector $\vec{\beta}$ is a two dimensional wave vector in the plane of the surface; when entered into Equation (2.25), the dispersion relation for SPPs is defined. Hence, if the light hits the surface in any direction, the external radiation dispersion line will always lay between the light line and the horizontal ω_s line in such a way that it will never intersect the SPP line. Light incident on an ideal surface cannot excite SPP modes [10]. However, there are two mechanisms in which SPP modes can be excited. Surface roughness or gratings can provide the requisite momentum via the Umklapp process, or the translation of the plasmon frequency wave vector into another Brillouin zone [12]. The second is attenuated total reflection (ATR) via total internal reflection through a

prism, sometimes referred to as prism coupling [13]. For this research, the focus will be on the former.

Consider a thin metal film on a dielectric substrate with a square array of holes as shown in Figure 4. $\left|\vec{k}_0\right| = 2\pi / \lambda$ is the propagation constant of the incident radiation and $\vec{k}_x = \left|\vec{k}_0\right| \sin(\theta_i)$ is the component of the wave vector of the incident radiation that is in-plane with the surface. For this arrangement, the incident photon and grating momentum match the SPP momentum when

$$\vec{k}_{spp} = \vec{k}_x \pm i\vec{G}_x \pm j\vec{G}_y \tag{2.26}$$

where $\vec{k}_{spp}$ is the SPP wave vector and is the same as $\vec{\beta}$ described above, $\vec{G}_x$ and $\vec{G}_y$ are the grating lattice vectors, $\left|\vec{G}_x\right| = \left|\vec{G}_y\right| = 2\pi / \Lambda$, where Λ is the period of the hole array and i, j are integers [14] . Therefore, due to the corrugated surface, this type of structure will support SPP modes.

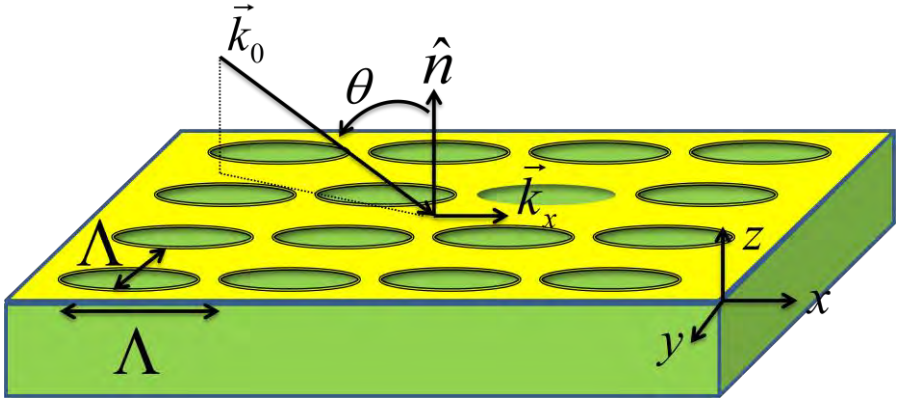

Figure 4. Graphical representation of a thin metal film with a periodic lattice of holes with period Λ for the excitation of SPPs. $\vec{k}_0$ is the wave vector of the incident light, $\vec{k}_x$ and $\vec{k}_y$ are the components of the incident radiation parallel to the surface interface.

The frequency of these SPP modes depends on the angle of incidence, the grating momentum vector and the complex index of refraction of the surrounding medium and the metal layer.

From Equations (2.26) and (2.22), an angle dependent representation of the resonant modes can be shown as

$$\lambda_{i,j}(\theta_{inc}) = \frac{\Lambda \left| \sqrt{\frac{\varepsilon_m(\lambda_{i,j})\varepsilon_d(\lambda_{i,j})}{\varepsilon_m(\lambda_{i,j}) + \varepsilon_d(\lambda_{i,j})}} \right|}{\sqrt{\left(i \pm \frac{\Lambda}{\lambda_{i,j}} \sin\theta_{inc} \right)^2 + j^2}} \tag{2.27}$$

where $\varepsilon_m(\lambda)$ is the permittivity of the metal film and $\varepsilon_d(\lambda)$ is the permittivity of the dielectric of the interface. The wavelength dependence of $\varepsilon_d(\lambda)$ can be neglected and it can be approximated as

$$n_{d,eff} = \sqrt{\varepsilon_d'} \approx \frac{\lambda_{1,0}}{\Lambda} \tag{2.28}$$

since $|\varepsilon_m'| \gg \varepsilon_d', \varepsilon_m'' \gg \varepsilon_d''$ and $\varepsilon_d' \gg \varepsilon_d''$ where $\varepsilon = \varepsilon' + i\varepsilon''$ [15].

If the structure coordinates are aligned with spherical coordinates such that the x-axis is aligned with $\phi_{inc} = 0$, then if $\phi_{inc} = 45°$, the incident wave vector also includes a y component, *i.e.*

$$\vec{k}_{spp} = \vec{k}_x + \vec{k}_y \pm i\vec{G}_x \pm j\vec{G}_y \tag{2.29}$$

where

$$\vec{k}_x = \hat{x}\,|\vec{k}_0|\,\frac{\sqrt{2}}{2}\sin\theta_{inc}$$
$$\vec{k}_y = \hat{y}\,|\vec{k}_0|\,\frac{\sqrt{2}}{2}\sin\theta_{inc} \qquad (2.30)$$
$$\vec{G}_x = \hat{x}\,\frac{2\pi}{\Lambda}, \text{and}\, \vec{G}_y = \hat{y}\,\frac{2\pi}{\Lambda}$$

where $\hat{x}$ and $\hat{y}$ are unit vectors in the x and y directions, respectively. For this orientation, the resonant modes are

$$\lambda_{i,j|\phi_{inc}=45^\circ}(\theta_{inc}) = \frac{2\left|\sqrt{\frac{\varepsilon_m(\lambda_{i,j})\varepsilon_d}{\varepsilon_m(\lambda_{i,j})+\varepsilon_d}}\right|}{\sqrt{\left(\frac{\sqrt{2}}{\lambda_{i,j}}\sin\theta_{inc} \pm i\frac{2}{\Lambda}\right)^2 + \left(\frac{\sqrt{2}}{\lambda_{i,j}}\sin\theta_{inc} \pm j\frac{2}{\Lambda}\right)^2}} \qquad (2.31)$$

Another phenomenon that adds to the spectral transmission of SPP structures is the Wood's anomaly described by

$$\lambda_R = \frac{\Lambda}{m}(n_{eff}(\lambda) \pm \sin\theta_{inc}),\ m = 1,2,3... \qquad (2.32)$$

The Wood's anomaly takes place when, for certain diffraction orders and incident angles, the diffracted light lies in the plane of the surface. Since the radiation cannot be scattered into this forbidden region, it is redistributed into allowed diffraction orders [16].

It has been observed that arrays of subwavelength sized holes in otherwise optically thick metal films exhibit peaks in the transmission spectra. At these maxima, the transmission efficiency is orders of magnitude greater than that predicted by standard aperture theory at wavelengths up to ten times the size of the holes [17]. This highly unusual zero-order transmission spectrum has been named extraordinary transmission.

Also included in the spectral transmission of a metal-dielectric structure such as that depicted in Figure 4 is the propagation of the incident radiation through the holes. It has been shown that the holes will always support a propagating mode near the surface plasmon frequency [18]. These modes can be found by solving the circular waveguide equations. This contribution is not detailed here because the main focus of this research will be on extraordinary transmission at frequencies well below the surface plasmon frequency. However, these phenomena can be combined via superposition to form the extraordinary transmission spectra for SPP structures, making is difficult to determine the location of higher-order modes. Since the lowest order modes take place at the longest wavelength, far away from the surface plasmon frequency, they can usually be determined. The extraordinary transmission of these structures makes them very attractive for various applications including spectrally selective emitters, interfacing between external optics and focal plane arrays, and enhancing the surface sensitivity of spectroscopic measurement systems.

Finite Difference Time Domain (FDTD) Analysis

To fully describe the physics inherent in a finite difference time domain (FDTD) Maxwell's equations solving algorithm, consider a full representation of Maxwell's equations,

$$\nabla \times \vec{E} = -\vec{M}_i - \frac{\partial \vec{B}}{\partial t} \tag{2.33}$$

$$\nabla \times \vec{H} = \vec{J}_i + \vec{J}_c + \frac{\partial \vec{D}}{\partial t} \tag{2.34}$$

$$\nabla \cdot \vec{D} = q_{ev} \tag{2.35}$$

$$\nabla \cdot \vec{B} = q_{mv} \tag{2.36}$$

where $\vec{M}_i$ is the impressed magnetic current density, $\vec{J}_i$ is the impressed electric current density, $\vec{J}_c$ is the conduction electric current density, q_{ev} is the electric charge density and q_{mv} is the magnetic charge density [19]. FDTD uses a discrete definition of geometry for a given EM problem in both time and space. The EM fields and material geometries are described on discrete Yee mesh cells, as shown in Figure 5. The Equations (2.33)-(2.36) can be described discretely in time where the time step is related to the mesh size through the speed of light. This technique is an exact solution to Maxwell's equations in the limit that the mesh cell size goes to zero.

For this research effort, Lumerical's commercially available FDTD software is used. Since this algorithm directly solves Maxwell's equations, the solution are assumed to be correct as long as the boundary conditions and solver mesh are correctly established.

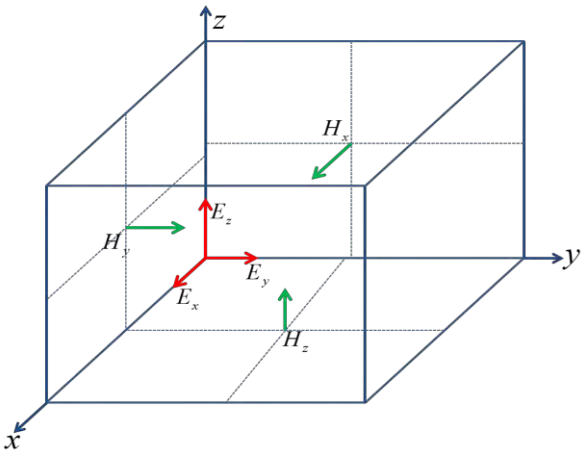

Figure 5. Yee cell representation as used by FDTD to solve Maxwell's equations.

Lumerical's software has a pre-loaded material database with material characteristic definitions from widely accepted publications like Edward Palik's "Handbook of Optical Constants" and the "CRC Materials Science and Engineering Handbook" [20, 21]. If a material that is to be modeled is not in the materials database, the user can define it and load it into the simulation via a materials definition script. Depending on the simulation bandwidth, the software interpolates the materials' complex refractive index data points to continuous functions. If using sampled or user defined materials data, this interpolation can be checked and adjusted to ensure good fits across the simulation bandwidth. This becomes especially important when modeling dispersive materials. A badly interpolated function for material characteristics will cause the simulation to diverge.

Since FDTD is a time-domain method, the EM fields are calculated as a function of time. The time signal of the source is a pulse defined by

$$s(t) = \sin[\omega_o(t - t_o)]e^{-\frac{(t-t_0)^2}{2(\Delta t)^2}} \tag{2.37}$$

where t_0 is the initial time, ω_o is the initial angular frequency and Δt is the time step. The Fourier transform of $s(t)$ is

$$s(\omega) = \int e^{i\omega t} s(t) dt \tag{2.38}$$

Ideally, $s(t)$ would be a Dirac delta function; this would give the system's response for all frequencies. It is more efficient and numerically accurate to excite the system with a short pulse such that $|s(\omega)|^2$ has a reasonably large value over all frequencies of interest [22].

Lumerical's FDTD has several boundary condition (BC) definitions. The two used in this research were the Perfectly Matched Layer (PML) and the Bloch BC. The PML acts as a perfect absorber, allowing the fields to decay in the defined direction, and is useful in confining the system's response to the physical structure being modeled. This is implemented by multiplying the curl component in the defined direction of Equations (2.33) and (2.34) with a term that allows the fields to exponentially decay. For example

$$\nabla \times \vec{E} = \left(\frac{\partial}{\partial y} \vec{E}_z - \frac{\partial}{\partial z} \vec{E}_y \right) \hat{x} + \left(\frac{\partial}{\partial z} \vec{E}_x - \frac{\partial}{\partial x} \vec{E}_z \right) \hat{y} + \left(\frac{\partial}{\partial x} \vec{E}_y - \frac{\partial}{\partial y} \vec{E}_x \right) \hat{z}$$
$$\frac{\partial}{\partial x} \rightarrow \frac{1}{1 + i \frac{\sigma_x(x)}{\omega}} \frac{\partial}{\partial x} \tag{2.39}$$

will cause the electric field to decay in the x-direction. $\sigma_x(x)$ is a term that quadratically or cubically increases from zero at the defined boundary [23].

Bloch BCs are used in simulating periodic structures when a phase shift between periodic unit cells in the model structure exists. This applies when using a plane wave source at off-normal incidence or when using dipole sources to simulate the dispersion relation of a periodic structure. This BC is based on Bloch-Floquet theorem mentioned in Equation (2.4).

There are many radiation sources available in the Lumerical software package. The one most often used for this research is the plane wave source. This source must only be used with periodic BCs placed normal or at less than 90 degrees to the propagation vector and PML BCs in the positive and negative propagation direction. The source should be extended outside the periodic boundary. In other words, a plane wave source is assumed to have infinite width (1-d) or area (2-d) propagating into an absorbing BC.

In general, the plane wave source in FDTD is always linearly polarized. However, different polarization states can be simulated using the superposition of two or more sources. For example, to simulate un-polarized light, an average can be taken from all possible input polarizations

$$\left|\vec{E}\right|^2_{ave} = \frac{1}{2\pi}\int_0^{2\pi} |\vec{E}(\alpha)|^2 \, d\alpha \tag{2.40}$$

where α is the polarization angle measured from the plane of incidence. Due to linearity, $\vec{E}(\alpha)$ can be expressed as

$$\vec{E}(\alpha) = \vec{E}_s \sin(\alpha) + \vec{E}_p \cos(\alpha) \tag{2.41}$$

where $\vec{E}_s$ and $\vec{E}_p$ are s-polarized and p-polarized electric fields. Inserting Equation (2.41) into (2.40) gives

$$\left|E\right|^2_{ave} = \frac{1}{2}\left(\left|\vec{E}_s\right|^2 + \left|\vec{E}_p\right|^2\right) \tag{2.42}$$

Therefore, to simulate un-polarized light, two sources can be used, one with p-polarization, the other with s-polarization, by defining their phases to be equal. Similarly, circular polarization can be simulated by the superposition of a s-polarized source and a p-polarized source with their phase differing by 90 degrees. By adjusting α and the phase of two sources, any polarization state can be simulated.

One limitation of FDTD is when a broadband source is simulated for an off-normal incidence angle with Bloch BCs; the source angle varies as a function of wavelength. Broadband sources inject fields that must have a constant in-plane wave vector at all wavelengths given by

$$k_{in-plane} = \frac{2\pi}{\lambda_c}\sin(\theta_d) \tag{2.43}$$

where λ_c is the center wavelength and θ_d is the user defined incident elevation angle. Because this value must be constant for all λ,

$$\begin{aligned} \sin[\theta_i(\lambda)] &= \frac{k_{in-plane}}{|k(\lambda)|} \\ \Rightarrow \theta(\lambda) &= \sin^{-1}\left(\frac{\sin(\theta_d)\lambda}{\lambda_c}\right) \end{aligned} \tag{2.44}$$

Therefore, if a broadband source is going to be used at off normal incident elevation angles with Bloch BCs, then θ_i will vary with λ as shown in Figure 6.

If a system response is desired with dependences on θ_i and λ, like a dispersion relation, then this limitation presents a challenge. There are two options for overcoming this. First, a two dimensional sweep can be formed where a simulation is run for each $\theta_i - \lambda$ combination; this technique gives good results but is time consuming. The second option is to perform a broadband sweep in θ_i and then interpolate the data points post-simulation into a common source injection angle. This technique is easy to implement since the data points are present for each θ_i and λ; they just need to be aligned and interpolated into a common step size. Figure 7 shows the results of this algorithm. The plot on the left shows the data points prior to interpolation, and on the right, data points afterwards. One drawback of this technique is the constraint placed on θ_d given by

$$\max(\theta_d) = \sin^{-1}\left(\frac{\lambda_c}{\lambda_{\max}}\right) \tag{2.45}$$

So the range of θ_d depends on the bandwidth of interest, and a full angle range, $\theta_d = [0°, 90°]$, cannot be evaluated using this method.

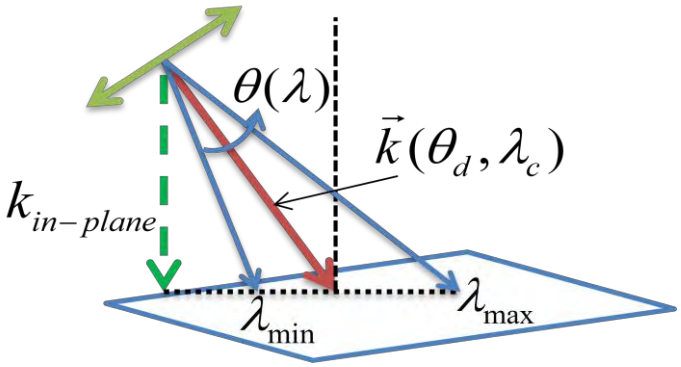

Figure 6. Definition of the incident elevation angle's, θ_i , dependency on λ in FDTD simulations when using Bloch BCs.

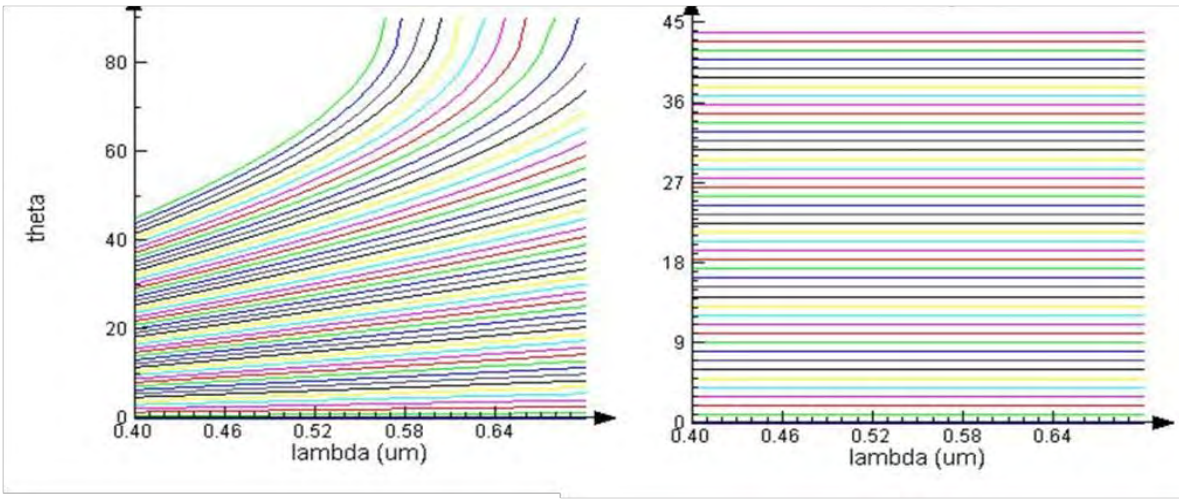

Figure 7. (left) Data points prior to interpolation with the described $\theta_i(\lambda)$ dependence. (right) Data points after interpolation where the data for each λ has a common source incident elevation angle [22].

The system's response is measured by monitors. There are multiple monitors available in Lumerical but the only one used in this research was the frequency domain power monitor (FDPM). The FDPM collects the time signal at a specified location, a line for 2-d simulations and a plane for 3-d, and performs a Fourier transform, returning the complex field values at the specified location. Analysis groups are collections of monitors and defined functions to return desired simulation characteristics. Users can define their own analysis groups, which was done for the Mueller matrix simulation and will be described in Chapter 4.

Lumerical's FDTD software package provides a very powerful design and modeling capability. The user interface is easy to use and there is extensive documentation available on Lumerical's website [22]. This software is also available on high performance computing (HPC) clusters worldwide. In the United States, Lumerical is available on Harvard's National Nanotechnology Infrastructure Network Computation Project. This cluster is available to academic researchers in the U.S. and was accessed to simulate some of the largest model definitions for this research.

Bidirectional Distribution Scatter Function

EM scatter may be described by the bidirectional scatter distribution function (BSDF), defined in radiometric terms as the scattered radiance divided by the incident irradiance.

$$BSDF = \frac{dL_s(\theta_s, \phi_s)}{dE_i(\theta_i, \phi_i)} \tag{2.46}$$

where θ is the elevation angle in spherical coordinates with respect to the surface normal, ϕ is the azimuthal angle, and the subscripts i and s refer to incident and scattered, respectively. This function describes the power scattered per unit solid angle by a sample as shown in Figure 8. The BSDF can be segmented into two contributions, the reflected radiance as a bidirectional reflection distribution function (BRDF), and the transmitted radiance as a bidirectional transmission distribution function (BTDF).

$$BSDF = BRDF + BTDF \tag{2.47}$$

Electromagnetic scatter from a surface can be described deterministically by defining boundary conditions for the surface profile and solving Maxwell's equations, but for optical surfaces, the features that make up the surface profile that must be considered are on the nanometer scale due to the small wavelength of light. If measured using a laser beam, the area illuminated is typically thousands of times larger than a wavelength. Although this technique has been done for 2-d surfaces [25], this approach becomes computationally challenging. Rather, BSDF models used to describe scatter are based on physical theory, that is to say they follow basic physical laws, but use measured data to specify parameters and fit the model to the data. These models use statistical descriptions to describe the surface profiles based on measured data. When light is scattered from a surface, even a very smooth surface like a mirror, some light is scattered in every direction and some is scattered such that the angle of reflection equals the angle of incidence, or into the specular direction. BSDF models attempt to describe the different contribution from both phenomena at all scatter angles. Many of these models describe the surface as micro-facets that are oriented according to some statistical distribution function or surface distribution function (SDF), but are themselves perfectly smooth.

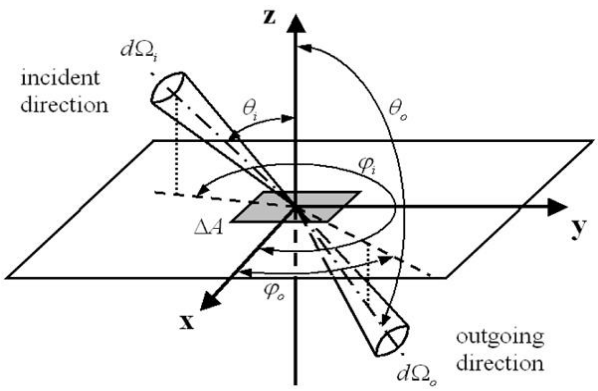

Figure 8. BSDF Definition [24].

The reflection and transmission from each facet is then described by Fresnel reflection; the angle of incidence equals the angle of reflection and the angle of transmission depends on the index of refraction of the material. Micro-facet models result in a computationally fast method to predict scatter, and do a fairly good job of describing it for many surfaces. If there are scatterers present on the surface that are much smaller than a wavelength, then Rayleigh scatter can be used to effectively describe the scatter by describing the surface roughness as a power spectrum distribution (PSD) function and performing a Fourier transform. Spherical scatterers can be described by Mie scatter for above surface structures or particles; non-spherical scatterers are often approximated the same way.

Many BSDF models have been developed to describe the scatter from surfaces. Dr. Thomas Germer at the National Institute of Standards and Technology (NIST) has developed a BSDF library in C++ called ScatMech [26]. A subset of these models is shown in Figure 9.

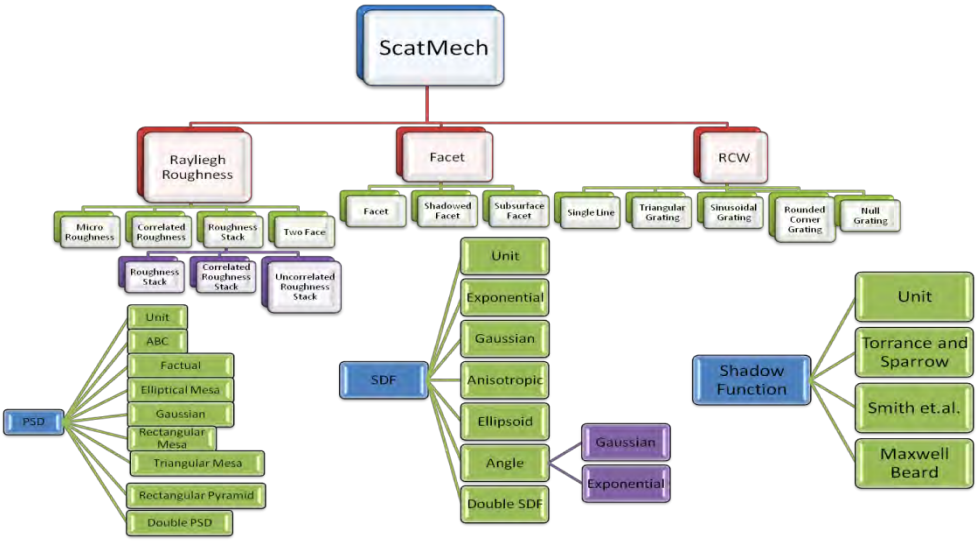

Figure 9. Hierarchy representation of a subset of ScatMech BSDF library model classes.

This library contains several BSDF model classes and sub-classes that include facet models, Rayleigh-Rice approximation models, Mie scattering models and an effective rigorous coupled-wave BSDF model. ScatMech also contains several PSD, SDF and grating profile functions, providing an expansive range for fitting BSDF data to a model. Due to ScatMech's BSDF fitting range, it could be used to fit models to scatter from nano- and micro-structured materials. An investigation of this potential is outlined in Appendix A, where a fitting algorithm was developed to search ScatMech for model fits. The ability to efficiently search and fit ScatMech models to measured BSDFs would be valuable in predicting scatter from this new class of materials.

A more complete method for characterizing scatter is described in a polarimetric BSDF (pBSDF) model, which uses the Mueller matrix (Mm). A Mm is a four by four matrix that describes the transformation of an incident Stokes vector, $\vec{s}_i$, into the

reflected or transmitted Stokes vector, $\vec{s}_o$, for a specified incident solid angle Ω_s and elevation angle θ_s, *i.e.*

$$\vec{s}_o = \bar{M}m\,\vec{s}_i\,\Omega_s \cos\theta_s \tag{2.48}$$

where

$$\bar{M}m = \begin{bmatrix} m_{00} & m_{01} & m_{02} & m_{03} \\ m_{10} & m_{11} & m_{12} & m_{13} \\ m_{20} & m_{21} & m_{22} & m_{23} \\ m_{30} & m_{31} & m_{23} & m_{33} \end{bmatrix} \tag{2.49}$$

Stokes vectors describe the polarized intensity and can be expressed in terms of the electric field by

$$\vec{s} = \begin{bmatrix} s_0 \\ s_1 \\ s_2 \\ s_3 \end{bmatrix} = \begin{bmatrix} |E_x|^2 + |E_y|^2 \\ |E_x|^2 - |E_y|^2 \\ 2\,\mathrm{Re}(E_x E_y^*) \\ 2\,\mathrm{Im}(E_x E_y^*) \end{bmatrix} \tag{2.50}$$

where $s_0, s_1, s_2,$ and s_3 are elements of the Stokes vector corresponding to total intensity, linear polarization to either the *x*- or *y*-directions, linear polarization at ±45° from the *x*- or *y*-directions, and left- or right-hand circular polarizations, respectively, and E_x and E_y are the *x*- and *y*-components of the complex electric field of an EM wave traveling in the *z*-direction in Cartesian coordinates. The most general state of polarization is elliptical, of which linear and circular are special cases. A Stokes vector can also be defined in terms of intensity and parameters of the polarization ellipse (shown in Figure 10), giving measurable quantities to all its elements. The elements defined in this manner are

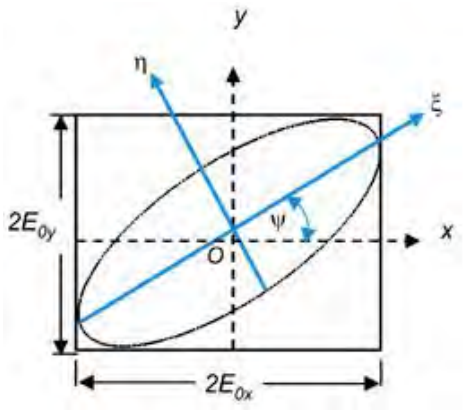

Figure 10. Polarization ellipse [27].

$$\begin{aligned} s_0 &= I \\ s_1 &= p\,I\cos(2\psi)\cos(2\chi) \\ s_2 &= p\,I\sin(2\psi)\cos(2\chi) \\ s_3 &= p\,I\sin(2\chi) \end{aligned} \tag{2.51}$$

where I is the intensity, p is the degree of polarization,

$$p = \frac{1}{s_0}\sqrt{s_1^{\,2} + s_2^{\,2} + s_3^{\,2}} \tag{2.52}$$

ψ is the angle of polarization or the major axis angle from the polarization ellipse and

$$2\chi = \tan^{-1}\left(\frac{s_3}{\sqrt{s_1^{\,2} + s_2^{\,2}}}\right) \tag{2.53}$$

Given these definitions, the polarization response for any optical system can be determined. ScatMech also provides the capability to model pBSDFs by incorporating a Mm into the definition of the models. More information about this ScatMech capability can be found at the NIST website [26].

If an optical system is polarization preserving the Mm is defined by

$$\bar{M}m_{preserving} = \begin{bmatrix} 1 & 0 & 0 & 0 \\ 0 & 1 & 0 & 0 \\ 0 & 0 & 1 & 0 \\ 0 & 0 & 0 & 1 \end{bmatrix} \tag{2.54}$$

while a completely depolarizing optical system will have a Mm defined by

$$\bar{M}m_{non-preserving} = \begin{bmatrix} 1 & 0 & 0 & 0 \\ 0 & 0 & 0 & 0 \\ 0 & 0 & 0 & 0 \\ 0 & 0 & 0 & 0 \end{bmatrix} \tag{2.55}$$

These definitions are useful when determining the degree of polarization by examining the Mm. As can be seen, the *p* of Mm (2.54) is equal to 1 and p of Mm (2.55) is equal to zero.

AFIT Optical Scatter Laboratory

The basis of this research effort was measured data taken in AFIT's Optical Scatter Laboratory. AFIT has a Schmitt Measurement Services complete angle scatter instrument (CASI) that has been upgraded into an automated Dual-Rotating-Retarder (DRR) Mm polarimeter. A CASI has the capability to make complete BSDF measurements and the DRR Mm polarimeter can provide complete pBSDF measurements as shown in Figure 11.

Another device used to characterize the structures researched was a Fourier transform spectrometer. Fourier transform spectroscopy uses a Michelson interferometer to split the light from a source into two beams. One beam is reflected off a fixed mirror while the other is reflected off moveable mirror which adjust the optical path length of

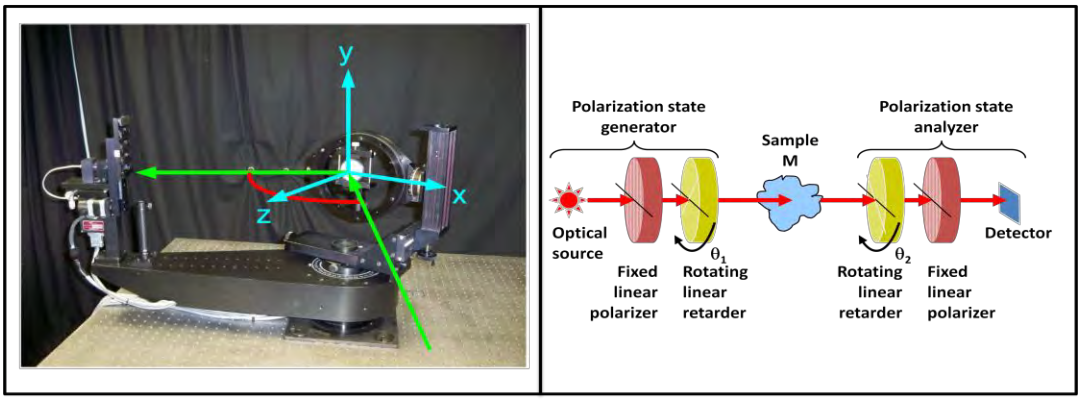

Figure 11. (right) AFIT's Schmitt Measurement Services CASI photograph. (left) DRR Mm polarimeter schematic.

that beam. The two beams are then recombined and scattered off the measurement sample. The scatter is collected by a detector and sampled at discrete time intervals corresponding to movements of the adjustable mirror, allowing the temporal coherence of the light, *i.e.* an interferogram, to be measured. The optical frequency spectrum of the scatter can then be determined from a Fourier transform of the interferogram.

These measurement instruments provided the empirical data to validate the analytical and simulation results for this research effort.

Summary

This chapter provided a brief theoretical background for this research effort including an overview of the theory of the novel nano-/micro-structured materials studied, PC photonic bandgap and SPP surface waves, the computational tool used, Lumerical's FDTD EM solver algorithm and software, and measurement instruments used to collect the data for this research including the BSDF physical definition, polarimetric terms and the Mm representation. These are all used in the following

analyses of a PC guided mode resonant filter and a SPP extraordinary transmission filter, and their scatter characteristics for off-normal incident radiation.

III. Guided Mode Resonance Filter Measurement, Analysis and Simulation Results

Guided mode resonance filters (GMRFs) are PCs which are designed to cause resonance with incident light at specific wavelengths. When these structures are illuminated, a portion of the beam is transmitted while the rest is diffracted and trapped in a waveguide structure. A portion of the trapped light is then diffracted back out of the waveguide and constructively or destructively interacts with the transmitted radiation. Resonance takes place when, at certain frequencies and incident angles, there is complete interference and no light is transmitted [5].

GMRF samples were provided by Prof. Brian Cunningham of the University of Illinois at Urbana Champaign. Fabrication of these structures can be found in publications by Prof. Cunningham [2, 3, 28]. The BDRFs of these structures were measured by Capt Robert Lamott as part of his AFIT MSEE thesis described in [29]. The filter studied here is designed to block incident radiation for normal incidence at 532nm. This structure is a 2-d GMRF like the one shown in Figure 12.

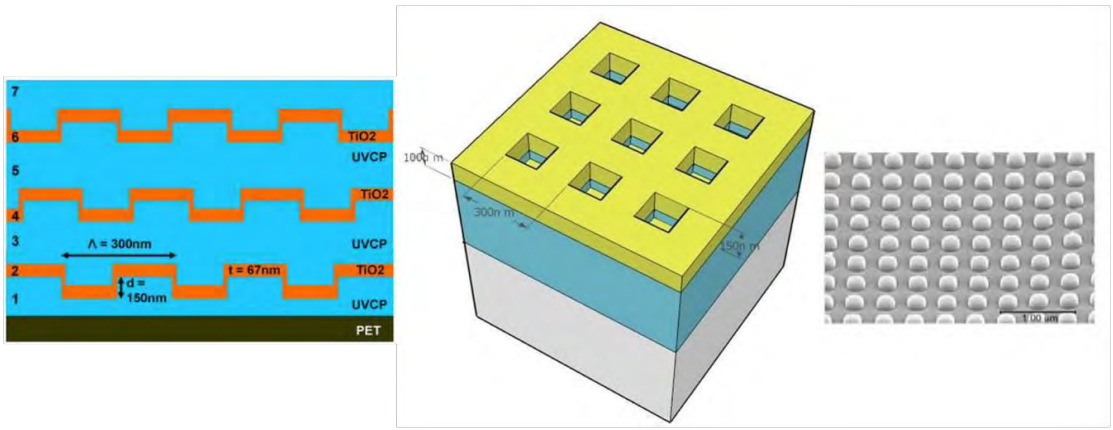

Figure 12. 2-D GMRF example geometry. (left) 2d schematic showing the layers of the filter. (center) Grating layer. (right) Scanning Electron Microscope (SEM) picture of the nano-mold used to fabricate each grating layer [2, 29]**.**

The filter consists of three 2-d grating structures each separated by 5μm of ultraviolet-cured polymer (UVCP) and has a protective plastic coating on both the top and bottom. The high index material used in the gratings is titanium dioxide (TiO_2).

This chapter begins with Capt Lamott's BSDF measurement of off-normal incident radiation at 544nm on this structure and those unique findings. Spectral transmission measurements from a Fourier transform spectrometer are then presented, as are Lumerical FDTD simulations of these measurements. The theoretical method used in the design and characterization of GMRFs is examined; this theory will then be used to characterize the FDTD simulations and measurements, and an explanation for these unique measurements is offered.

CASI and Fourier Transform Spectrometer Measurements

Complete angle scatter measurements of this structure were made with a 544nm laser and showed unique characteristics at θ_i=25.7°, as shown in Figure 13 [29]. As can be seen from the measured BSDF, this results in a unique scatter pattern. Lamott referred to this angle as the resonant angle, since at this angle, the GMRF scattered light in all directions as illustrated in the inset of Figure 13.

For this thesis, spectral transmission measurements were made for off-normal incidence, p-, s- and un-polarized incident light. The polarized measurements were made with the incident azimuthal angle, ϕ, equal to zero, *i.e.* the incident plane was parallel to the grating periodicity. The un-polarized measurement were made for $\phi = 0°$ and $45°$. These measurement are shown in Figures 14 and 15 on contour plots with λ versus angle of incidence. These same measurements were also made by Capt Lamott and are shown

in Appendix A of his thesis [29]. The angular resolution for the these measurements was 5°, except for the un-polarized measurements, where 1° steps were taken from 24°-27°. The measurements made here and those made by Lamott differ only by amplitude, but the locations of the nulls in the transmittance in λ and angle of incidence are the same.

Figure 16 shows the spectral transmission for s-, p- and un-polarized incident light at $\theta_i = 25°$. As can be seen from these measurements, at the angle that created the unique scatter patter, 25.7°, the filter is not in the defined GMRF resonance as described by Wang and Magnusson [30]. In other words, the structure is not completely filtering light at this wavelength and angle.

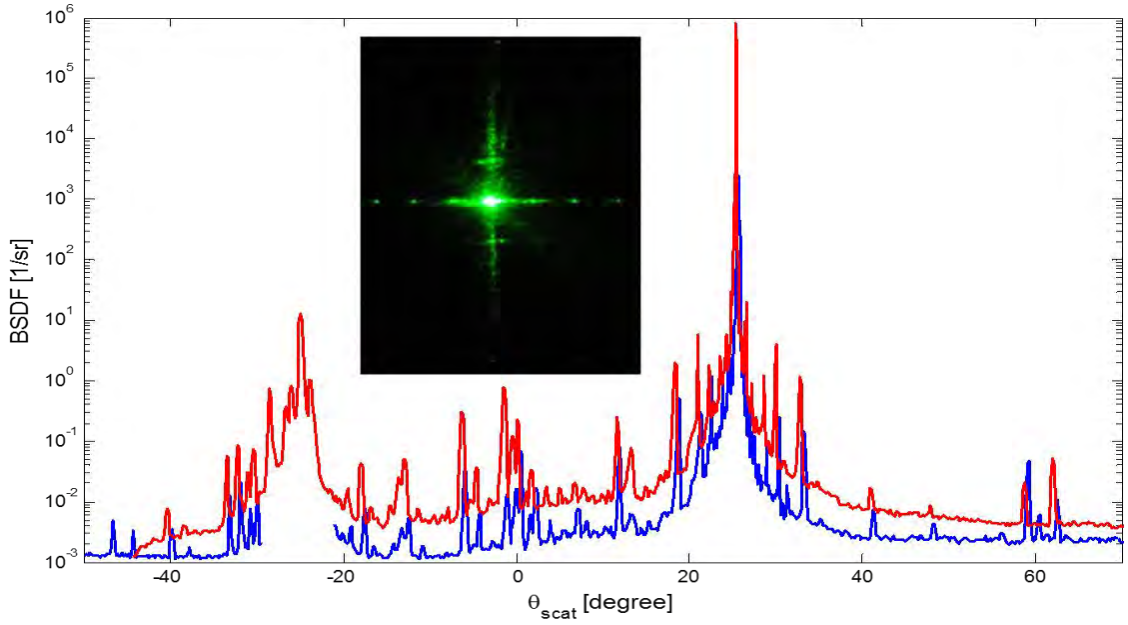

Figure 13. BSDF of 2-D GMRF at "resonant" angle (θ_i=25.7°) showing both transmission (red) and reflection (blue) [29]**. The GMRF was designed to provide filter protection for 532nm light and was measured at 544nm. The inset is a photo of the scatter at the resonant angle.**

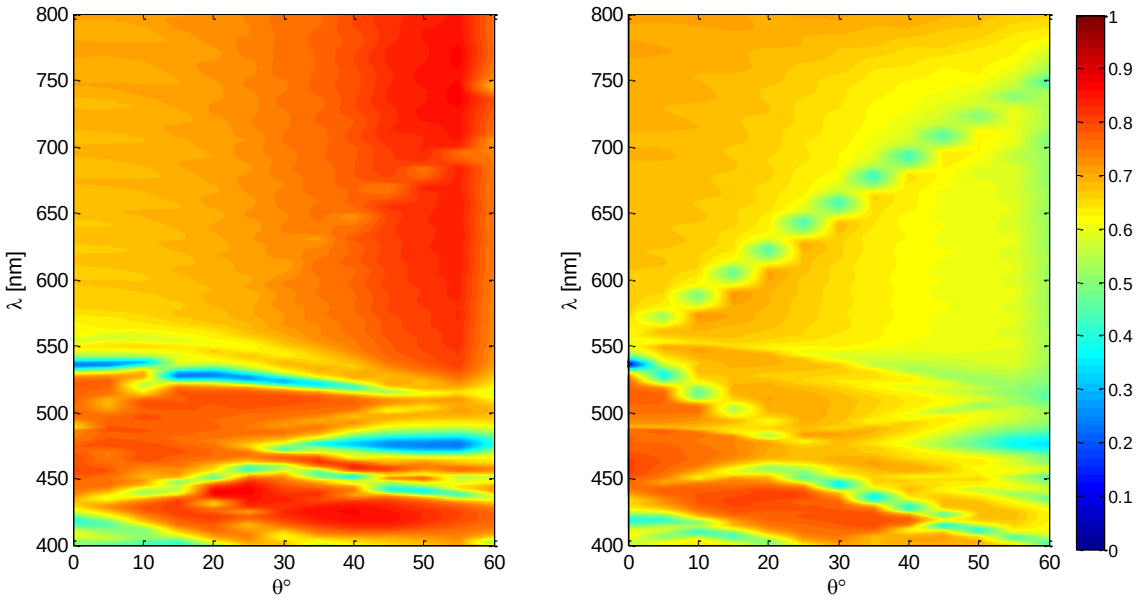

Figure 14. Measured spectral transmittance of the GMRF for p- (left) and s-polarization (right). Angle of incidence, θ_i, steps were made in 5° increments and the incident plane was parallel to the grating periodicity (φ=0°).

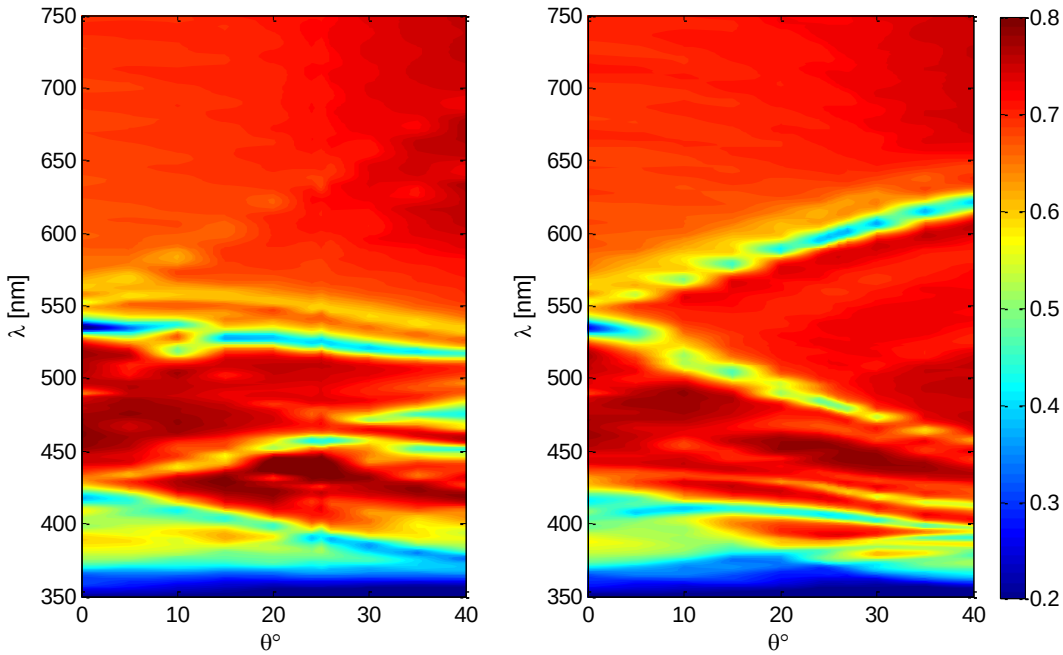

Figure 15. Measured spectral transmittance of the GMRF for un-polarized light with φ=0° (left) and 45° (right). Angle of incidence, θ_i, steps where made with 5° steps except around the angle of interest, 25°, where 1° steps were taken.

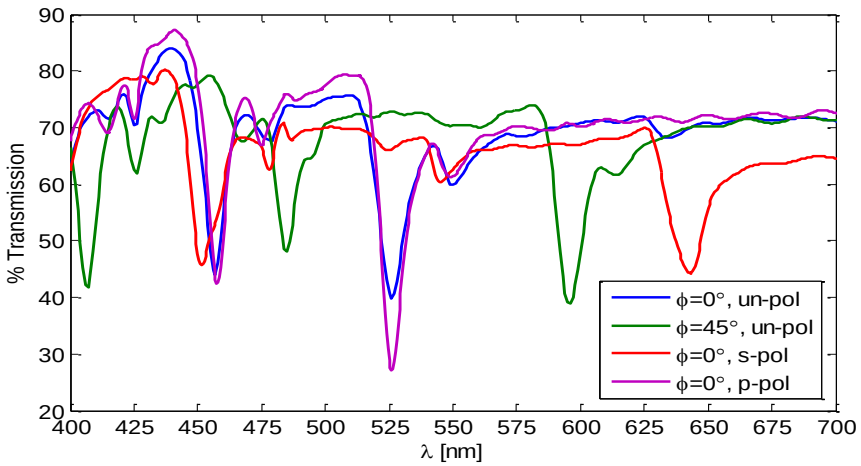

Figure 16. Measured spectral transmittance of the GMRF for all measured polarizations with θ_i=25°.

Theoretical Analysis

To fully understand and characterize the GMRF phenomena, consider a 1-d slab grating waveguide which has a modulated dielectric along the grating as shown in Figure 17. If light couples into the waveguide structure, it is possible to excite a guided mode. The guided mode will propagate in the x-direction but due to the periodic modulation, the structure is leaky; thus, guided modes cannot be sustained on the waveguide grating. The theoretical analysis of this phenomenon has been described by Wang and Magnusson for this simple example [30]. The electric permittivity in the grating is,

$$\varepsilon(x) = \varepsilon_g + \Delta\varepsilon \cos(Gx) \tag{3.1}$$

where ε_g is the average relative amplitude, $\Delta\varepsilon$ is the modulation amplitude and G is the grating momentum vector and $G = 2\pi / \Lambda$. In solving for the electric field in the grating, they let $\Delta\varepsilon \to 0$ and the solution then resembles that of a dielectric slab waveguide.

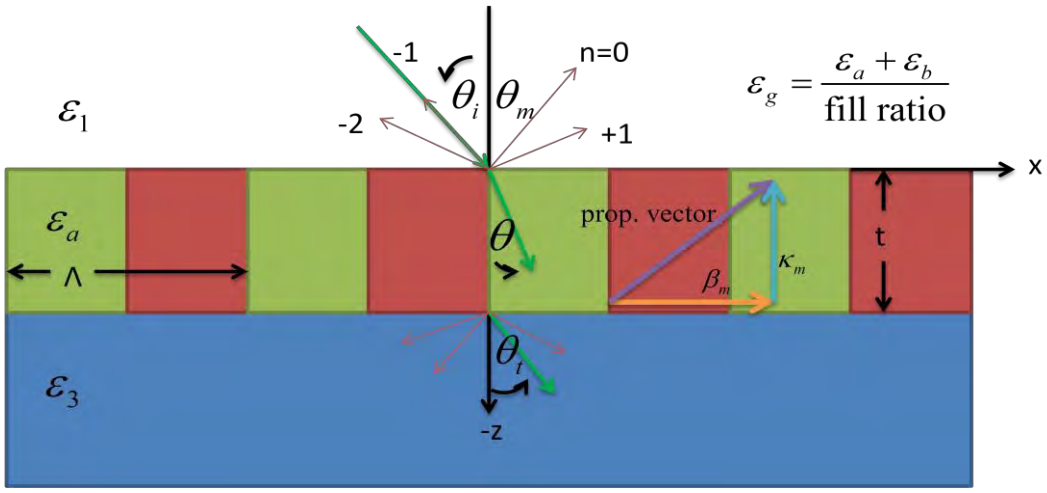

Figure 17. Basic 1-d slab GMRF. For certain incident angle and wavelength, there can exist a guided mode which propagates along the x-axis inside the grating structure, but due to the modulated dielectric, it acts as a leaky waveguide and allows the guided mode to scatter out.

Following their example, via rigorous coupled-wave (RCW) theory, the eigenvalue equation for the fields in the guided mode for a 1-d structure with a TM polarized incident field is

$$\tan(\kappa_m t) = \frac{\varepsilon_g \kappa_m (\varepsilon_3 \gamma_m + \varepsilon_1 \delta_m)}{\varepsilon_1 \varepsilon_3 \kappa_m^{\,2} - \varepsilon_g^{\,2} \gamma_m \delta_m} \tag{3.2}$$

where

$$\begin{aligned} \kappa_m &= \sqrt{\varepsilon_g k^2 - \beta_m^{\,2}}, \quad \gamma_m = \sqrt{\beta_m^{\,2} - \varepsilon_1 k^2} \\ \delta_m &= \sqrt{\beta_m^{\,2} - \varepsilon_3 k^2}, \quad \beta_m = k(\sqrt{\varepsilon_g}\sin(\theta) \pm m\lambda/\Lambda) \end{aligned} \tag{3.3}$$

and κ_m is the z-component of the propagating vector of the *m*th mode, γ_m and δ_m are the decay constants into the top and bottom lower index media, respectively, and β_m is the x component of the propagation vector of the *m*th mode, shown in Figure 17. For TE polarization, the eiganvalue equation is

$$\tan(\kappa_m t) = \frac{\kappa_m(\gamma_m + \delta_m)}{\kappa_m{}^2 - \gamma_m \delta_m} \tag{3.4}$$

By approximating the measured GMRF structure as a 1-d PC, shown in Figure 18, and using these equations, the guided modes can be estimated. Using $\Lambda = 0.3\mu m$, $\varepsilon_1 = \varepsilon_2 = 2.13$, $t = 0.25\mu m$, fill-ratio = 40% and $\theta_i = \sin^{-1}[\varepsilon_g{}^2 / \varepsilon_1{}^2 \sin(\theta)]$, a dispersion relation can be plotted, shown in Figure 19. Although the measured GMRF has two separate grating layers, this approximation still compares well to the FDTD simulation shown in the next section.

Figure 19, the dispersion relation of this 1-d approximation, shows where the left and right sides of Equations (3.2) and (3.4) are equal for angle of incidence, θ_i , and λ . As can be seen from this plot and comparing it to Wang and Magnusson's results, the m = ±1 mode is the most effective mode at filtering incident light. What needs to be determined is the mode that is causing the unique BSDF (Figure 13) that was measured by Lamott in the 2-d GMRF.

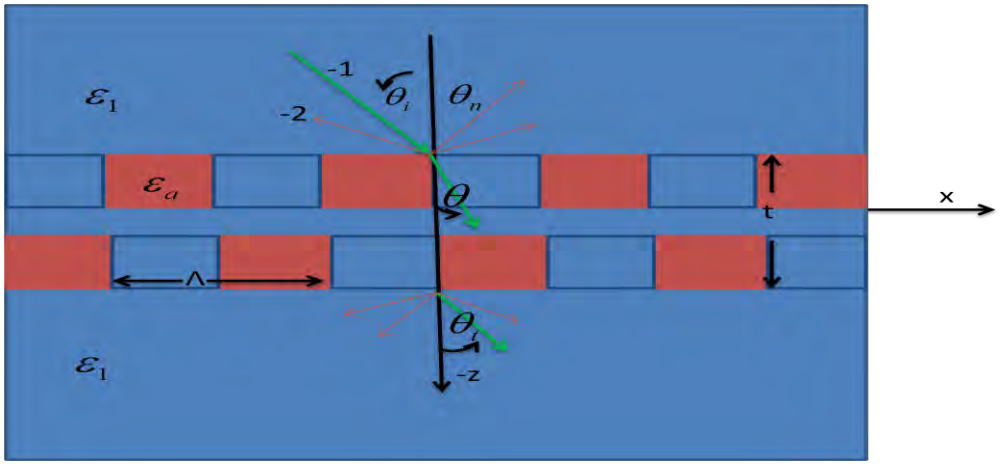

Figure 18. 1-d approximation of the GMRF that was measured (Figure 12) .

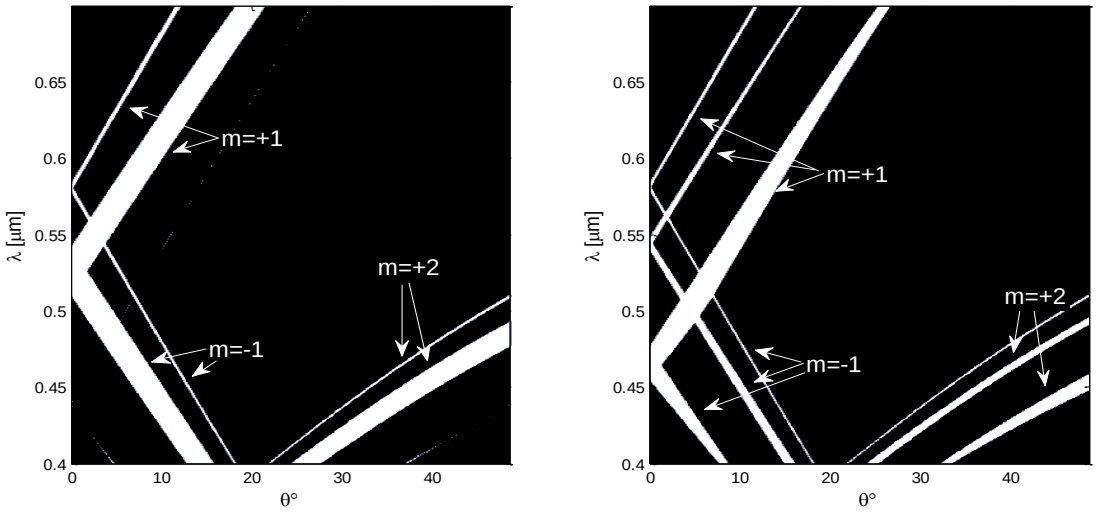

Figure 19. Dispersion relation of the structure depicted in Figure 18. TM polarization is shown on the left and TE on the right. These plots show where the left side and right side of Equations (3.2) and (3.4) are equal, resulting in the solutions of the eigenvalue equations for θ_i and λ.

A method for approximating the resonant modes in 3-d can be developed by treating the structure like a waveguide coupler. The equation for the modes of a waveguide coupler with s-polarization is

$$k\sin(\theta_{inc}) \pm m\frac{2\pi}{\Lambda} = \beta_m = \frac{2\pi}{\lambda} n_{eff} \tag{3.5}$$

For this case, n_{eff} can be approximated from $\lambda/\Lambda = n_{eff}$ since the m=1 mode for $\theta_{inc} = 0°$ is known to be at $\lambda = 532\text{nm}$. By following a similar development as that described for finding the modes of an SPP structure in Chapter 2 and defining

$$\vec{\beta}_{i,j} = \vec{k}_x + \vec{k}_y \pm i\vec{G}_y \pm j\vec{G}_x \tag{3.6}$$

where $\frac{2\pi}{\Lambda} = \left|\vec{G}_x\right| = \left|\vec{G}_y\right|$, $\vec{k}_x = \hat{x}\left|\vec{k}_{0,i,j}\right|\cos\phi_{inc}\sin\theta_{inc}$, $\vec{k}_y = \hat{y}\left|\vec{k}_{0,i,j}\right|\sin\phi_{inc}\sin\theta_{inc}$,

$\left|\vec{k}_{0,i,j}\right| = 2\pi/\lambda_{i,j}$, $\left|\beta_{i,j}\right| = 2\pi n_{eff}/\lambda_{i,j}$, and $\hat{x}$ and $\hat{y}$ are unit vectors. Hence, a 3-d approximation for the location of the guided modes can be expressed as

$$\lambda_{i,j}(\theta_{inc},\phi_{inc}) = \frac{n_{eff}}{\sqrt{\left(\frac{1}{\lambda_{i,j}}\sin\phi_{inc}\sin\theta_{inc} \pm \frac{i}{\Lambda}\right)^2 + \left(\frac{1}{\lambda_{i,j}}\cos\phi_{inc}\sin\theta_{inc} \pm \frac{j}{\Lambda}\right)^2}} \tag{3.7}$$

This relation is shown in Figure 20. For this relation, the (1,0) mode corresponds to s-polarization and the (0,1) mode corresponds to p-polarization since the definition for the grating coupler equation is for s-polarization. While this may seem like a very simple solution compared to the numerical methods used in literature, it compares very well with both the RCW approximation in 2-d and the measured results shown in Figures 14 and 15 for the (1,0) and (0,1) modes. The simulation results will also be shown to compare fairly well with this approximation for the higher modes.

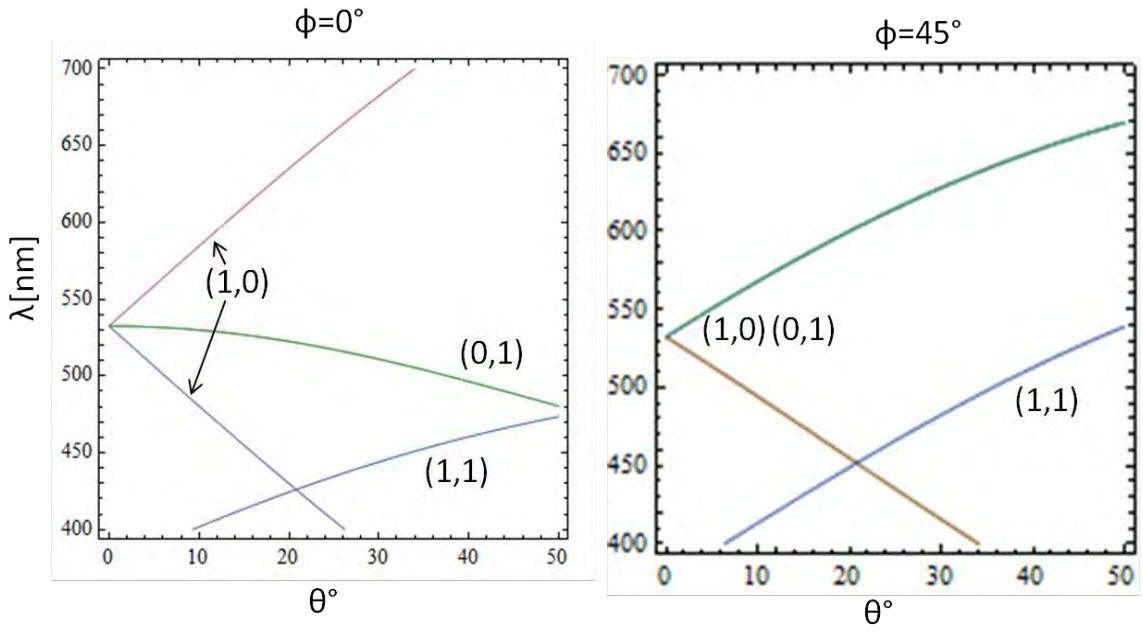

Figure 20. Solutions to Equation (3.7), for ϕ =0° and 45°, giving the approximate location of the lower order modes. The (1,0) mode for this representation corresponds to s-polarization and the (0,1) mode to p-polarization.

FDTD Simulation

Lumerical FDTD simulation of this structure proved challenging, especially when trying to simulate the unique BSDF measurement at 25.7° incident angle. While the simulation software does have the capability to measure angular transmission and reflection, the spatially very narrow peaks off-specular only appeared for one location in θ_s , ϕ_s , polarization and λ. On the other hand, spectral transmission simulations were readily developed to be compared to the measured data.

The first simulation was that of the 1-d geometry shown in Figure 18. This model is a 2-d model in x and y (instead of x and z as shown in the depiction). The transmittance from this simulation is shown Figure 21. As can be seen from the nulls (blue) areas from these plots, the m = ±1 mode, from Equations (3.2) and (3.4), is the most efficient at filtering radiation, while the m = +2 mode seems to have little, if any, effect on the transmittance. The location of the m= - 2 mode is out of the range of these plots. Note the close agreement between the simulation, which simulated the exact structure depicted in Figure 18, and the slab waveguide approximation dispersion relation (Figure 19), which approximated the two offset grating layers as a waveguide with an effective index of refraction equal to the average index in the two grating layers. The 1-d GMRF is much better at filtering TM polarization than TE, for this reason, the 2-d GMRF was designed to reduce the reflection differences due to polarization [2].

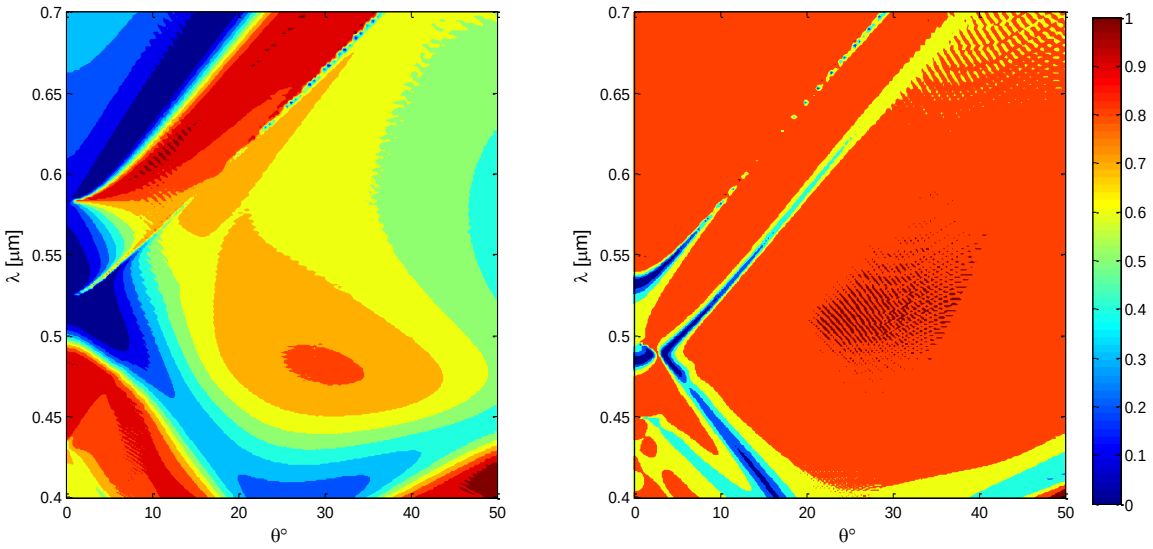

Figure 21. Simulated transmittance as a function of incident angle and wavelength of the 1-d GMRF depicted in Figure 18. TM polarization is shown on the right and TE on the left. Compare these plots with the slab waveguide approximation dispersion relation shown in Figure 19.

The next action in the modeling and simulation development was ensuring that the normal spectral transmission model of the 2-d GMRF compared well with measured and published results for this structure. The model's geometry was built using circular holes instead of the square ones depicted in Figure 12 since the fabrication of this structure used a silicon nano-mold with posts to form the holes. Two definitions for the refractive indices were tried. The one given by Palik in "Handbook of Optical Constants" included an imaginary component which always resulted in diverging fields in the simulation [20]. The best results came from using those published by Yang in his PhD dissertation (Prof. Cunningham was his advisor) [28]. The first model simulated one period in the x- and y-directions using Bloch BCs, and a 600nm span in the z-direction with a PML BC. Using this configuration, the plane wave excitation begins inside the

UVCP. Therefore, the wavelength was adjusted accordingly. Also, when comparing this simulated data to the measured data, θ_i needs to be adjusted by Snell's law.

$$\theta_{sim} = \sin^{-1}\left(\frac{1}{1.46}\sin\theta_{meas}\right) \tag{3.8}$$

where θ_{sim} is the incident angle shown in the simulations and θ_{meas} is the incident angle shown in the measurements. The simulated and measured spectral transmissions are compared in Figure 22, where the measured data is the same as that depicted in Figure 16.

This model was then used to simulate a sweep in θ_i and λ for s- and p-polarizations and $\phi = 0°$ and 45°, where the hemispherical transmission and reflection was measured with two FDPM planes with their normals in the z-direction. The transmission monitor was placed below the structure and the reflection monitor was placed above the source. In order to sweep θ_i from 0° to 50°, a two dimensional sweep was used as described in Chapter 2. The results from this simulation are shown in Figures 23-26. The simulated reflectance for $\phi = 0°$ is shown in Figure 24 but left out for $\phi = 45°$ for brevity.

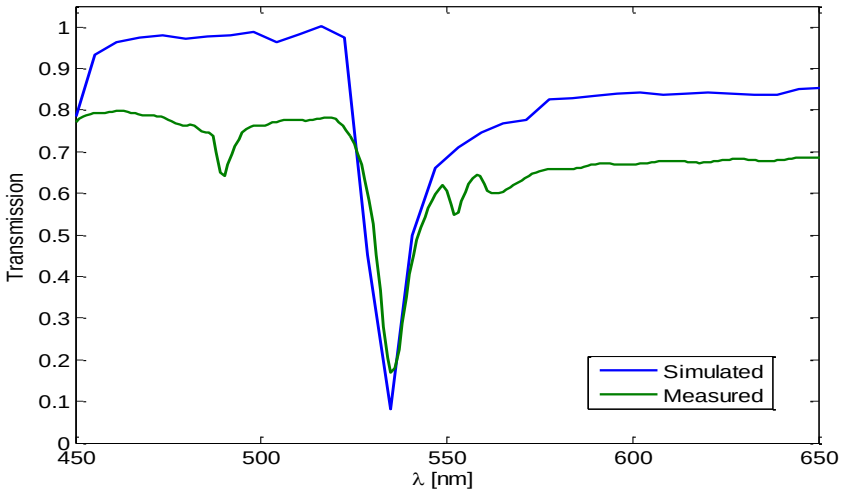

Figure 22. Measured (green) vs. simulated (blue) spectral transmission for un-polarized light for normal incidence.

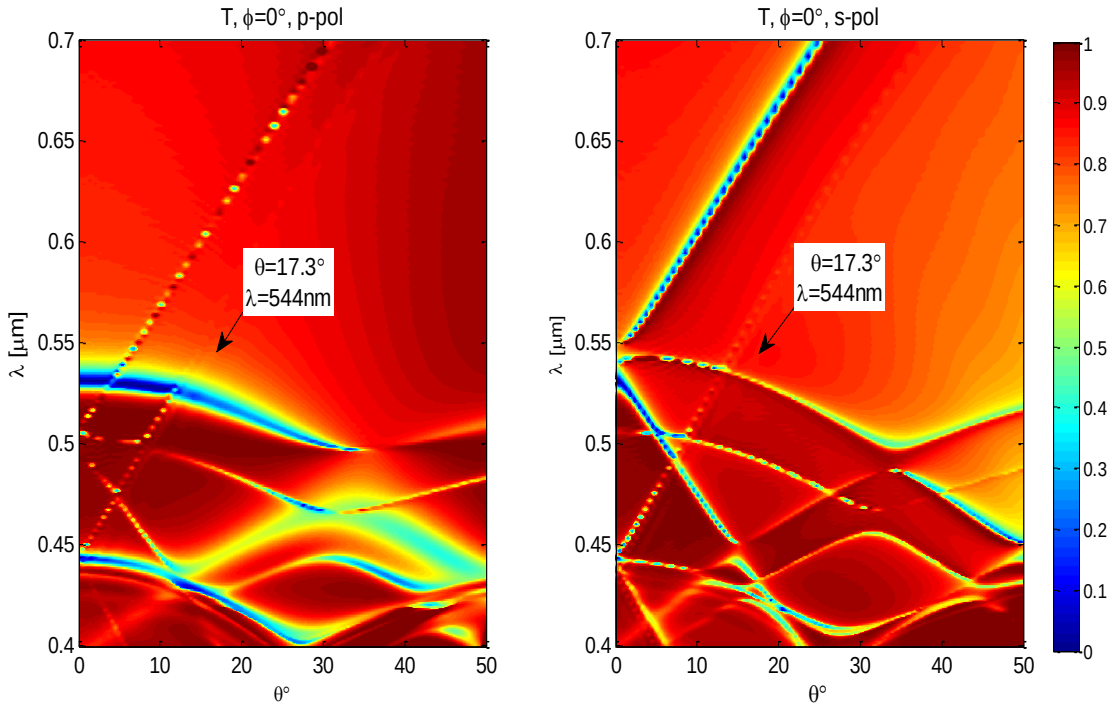

Figure 23. Simulated transmittance as function of incident angle and wavelength of a 2-d GMRF with φ=0°. The data cursor shows the location of the resonant angle (scaled by Snell's law) as measured by Lamott.

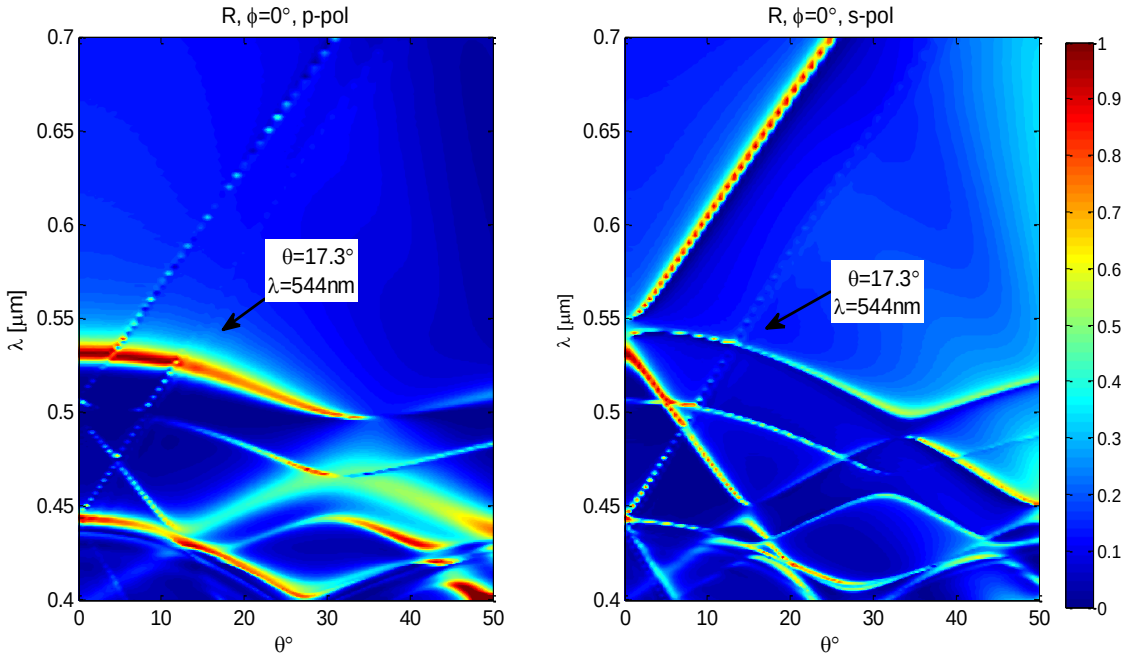

Figure 24. Simulated reflectance as function of incident angle and wavelength of a 2-d GMRF with φ=0°. The data cursor shows the location of the resonant angle (scaled by Snell's law) as measured by Lamott.

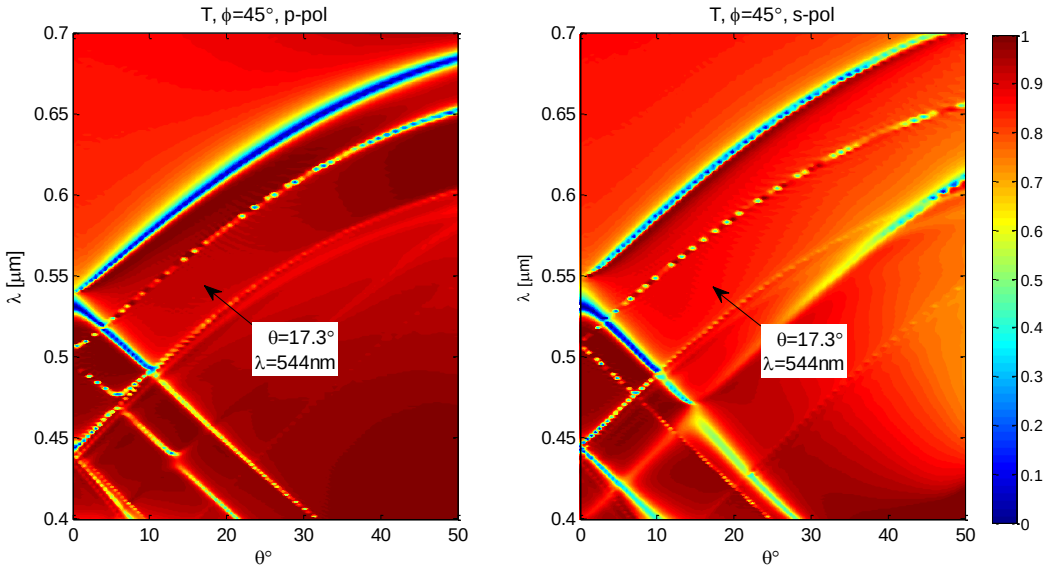

Figure 25. Simulated transmittance as function of incident angle and wavelength of a 2-d GMRF with φ=45°. The data cursor shows the location of the resonant angle (scaled by Snell's law) as measured by Lamott.

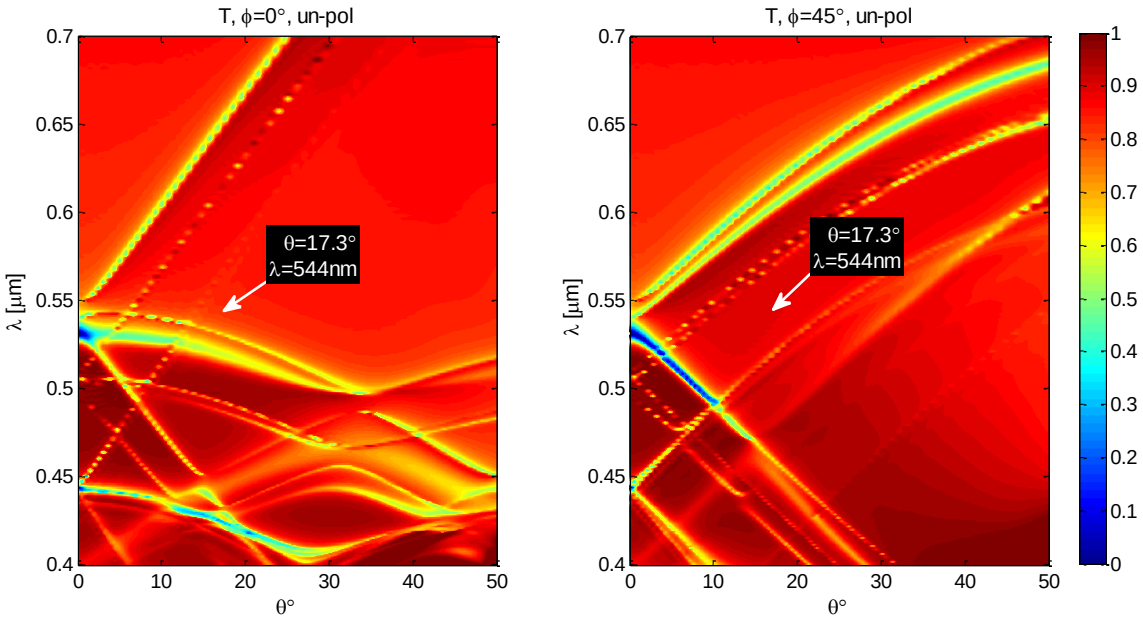

Figure 26. Simulated transmittance as function of incident angle and wavelength of a 2-d GMRF with un-polarized source and φ=0° and 45°. The data cursor shows the location of the resonant angle (scaled by Snell's law) as measured by Lamott.

Figure 23 can be compared to Figure 14 if the angle of incidence is scaled as mentioned above. However, it can be directly compared to the approximation made by Equation (3.7) and Figure 20. For s-polarization they compare well. These figures show a data cursor pointing to the location where Lamott measured the unique BSDF.

As can be seen in Figure 25, incidence at an azimuthal angle of φ=45° is not going to excite a coupled mode at the location in θ_i and λ where the unique BSDF pattern was measured.

Figure 26 shows the simulated transmittance for un-polarized radiation following the description given in Chapter 2; the simulated transmittance for p-polarization and s-polarization were averaged. These simulation results can be compared to the un-polarized angular measurements shown in Figure 15.

Figure 27 shows the measured and simulated spectral transmittance for s-, p- and un-polarized light. As mentioned in Equation (3.8), the simulated incident angle was scaled by Snell's law. The measured and simulated data do not compare well. While the null around 525nm is close for the measurements and simulations, the simulation does a poor job at predicting the null around 544nm.

Another simulation was done that approximates the structure as a one-layer grating covered with 500nm of UVCP on the top and bottom. The source excitation was placed above the UVCP and the reflection and transmission monitors were placed outside the UVCP. The results of this simulation are shown in Figure 28. Notice the location of the measured unique BSDF corresponds to the (0,1) mode in Equation (3.7) (plotted in Figure 20) for s-polarization.

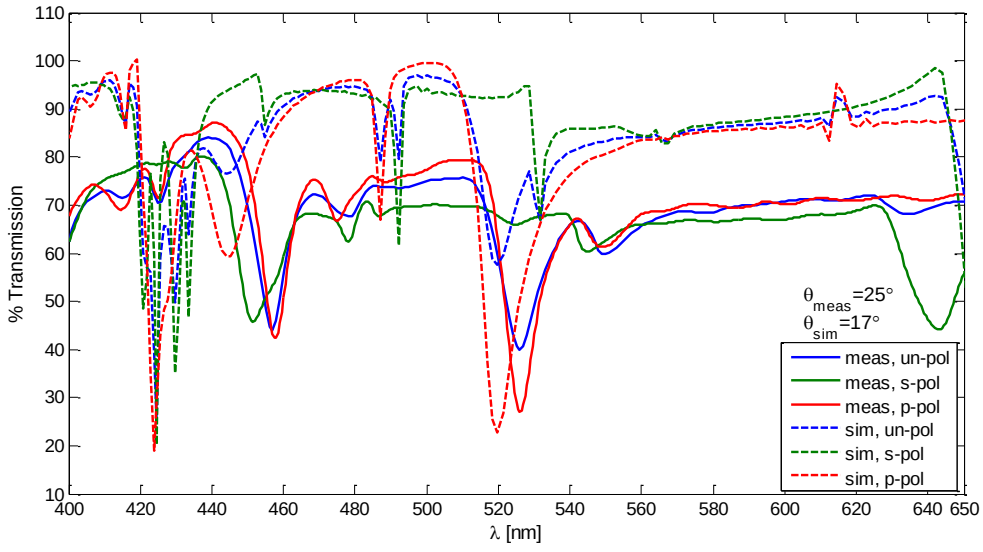

Figure 27. Simulated and measured transmittance of the 2-d GMRF for all measured and simulated polarizations with θ_{meas}=25° and θ_{sim}=17°.

Equation (3.7) is developed with incident angle and wavelength inside the UVCP. Snell's law of refraction (Equation (3.8)) was applied to this approximation and the result is shown in Figure 29. Notice the resemblance between this approximation and the simulations shown in Figure 28. From these results, it can be seen that the (1,0) mode causes the resonance as defined by Wang and Magnusson, and the (0,1) mode causes the unique BSDF as measured by Lamott. Since the resonant angle was measured at λ = 544nm and $\theta_i = 25°$, which intersects a coupled mode at one location, it is reasonable to assume that any guided-mode will result in a similar scatter pattern as measured by Lamott.

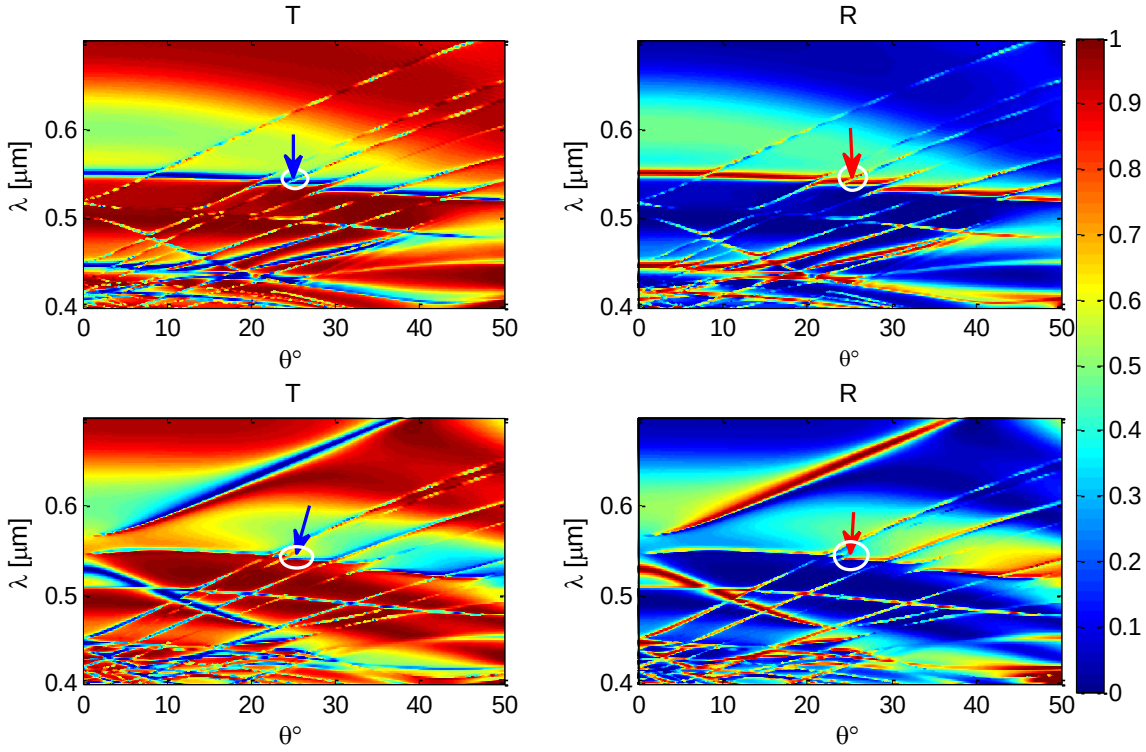

Figure 28. Reflectance and transmittance as functions of angle of incidence and wavelength of the GMRF approximated as a single layer with 500nm of UVCP on the top and bottom and with the source and monitors placed in free space. Top row depicts p-polarization and the bottom, s-polarization. The arrows point to the location of the unique measured BSDF.

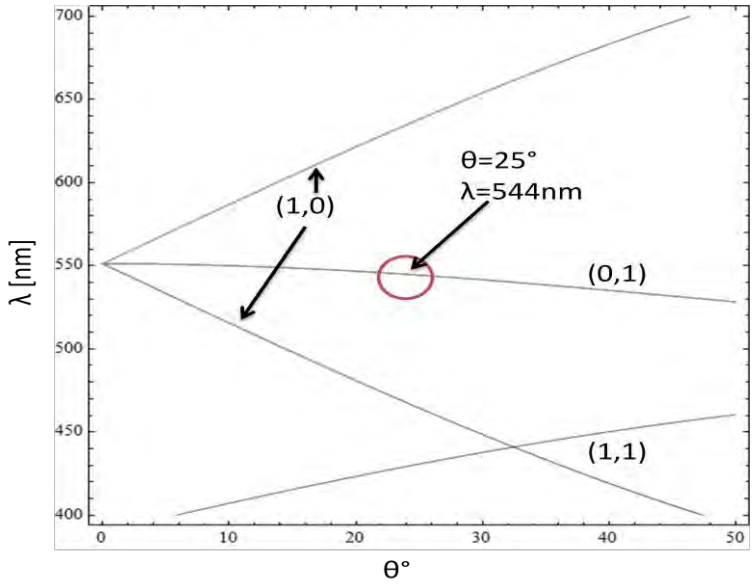

Figure 29. The solution of Equation (3.7) scaled by Snell's law. Note the resemblance to Figure 28 and the agreement between the (0,1) mode at θ_i=25° and λ=544nm.

Another simulation of this structure was done where the grating orders and their strengths were measured in all directions. In the z-direction, only specular grating orders were determined. However, in the x-/y-direction, multiple grating orders were calculated and their strengths were multiplied by the transmission in the respective direction to represent power propagating parallel to the grating periodicity. The results from this simulation are shown in Figure 30 where the normalized x/y transmission is plotted for points in λ and θ shown in the inset. The x/y transmission increases with incident angle at the locations of the guided modes.

The orders and their directions for three points, A, B and C (shown in the inset of Figure 30), were then plotted on spherical plots shown in Figure 31. The black dotted line represents the incident light, blue lines represent the specular reflection and the red and green lines represent power transmitted in the x-/y-directions. For normal incidence at

532nm, there is essentially no power transmitted in the x-/y-direction. For off-normal incidence at wavelengths not corresponding to coupled modes, the x/y transmission is minimal, and for wavelengths corresponding to coupled-modes with off-normal incidence, the x/y transmission is significant as shown in Figure 31 (C).

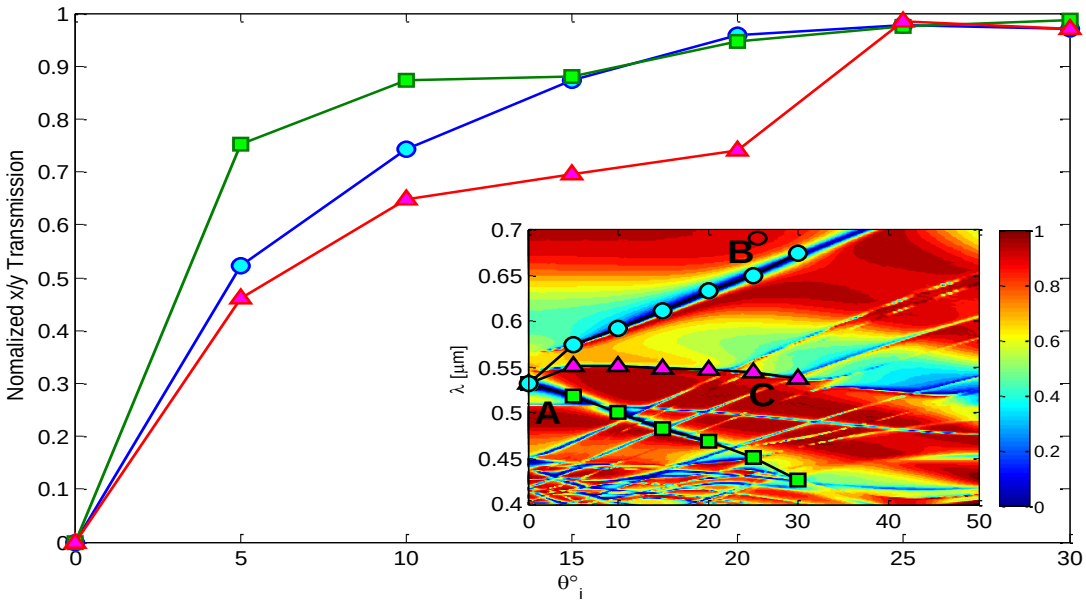

Figure 30. Normalized x/y transmission for seven points along the (±1,0) mode the (0,1) mode. The points are shown in the inset plot of the transmission from Figure 28. The points A, B, and C show where the grating orders were calculated and are plotted in Figure 31.

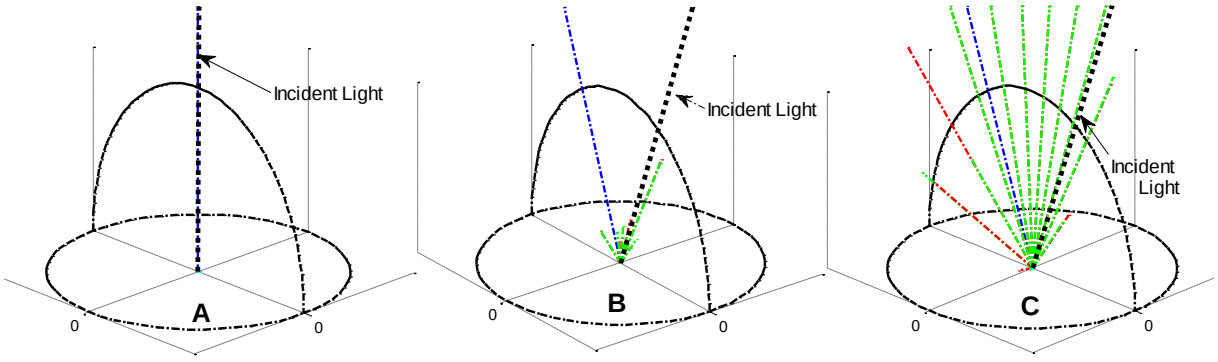

Figure 31. Spherical plots showing the grating orders and their direction for (A) λ=532nm and θ_i=0°, (B) λ=700nm and θ_i=25° and (C) λ=544nm and θ_i=25°.

These results provide evidence that at incident angles higher than approximately 5° and wavelengths corresponding to coupled modes, the structure will exhibit the unique BSDF pattern measured by Lamott.

Conclusion

A unique scatter pattern not previously mentioned in the literature was measured by Lamott for a GMRF [29]. The analysis and results of this chapter provide evidence that this unique BSDF pattern of the measured GMRF corresponds to any coupled mode defined by Equation (3.7) for incidence angles higher than 5°. Since these structures are designed as spectral filters, their performance is often characterized by spectral transmission/reflection measurements and the angular scatter has not been examined in the literature. The effects of this mode are hard to determine in spectral transmission measurements and simulations, but the effect this mode has in angular reflection and transmission patterns is of great consequence, as demonstrated by Capt Lamott. This pattern should scale with angle and frequency, providing a single challenge to the development of a parameterized BSDF model for these types of structures. Such a model would need to approximate this extraordinary scatter pattern only at the location of this mode, and elsewhere, with the pattern of a 2-d reflective/transmissive grating. The development of Equation (3.7) does provide an approximation to predict the mode in measured data. To further test the accuracy of this approximation, more measurements at different angles of incidence and wavelengths could be done. If Equation (3.7) can be substantiated through measurement-based analysis, then it could be incorporated into a

BSDF model for GMRF structures. Since Equation (3.7) is easy to derive and evaluate, it could provide the framework for a computationally fast BSDF model.

IV. Surface Plasmonic Extraordinary Transmission Filter Measurement, Analysis and Simulation Results

A collection of surface plasmonic extraordinary transmission filters was provided by Dr. Zahyun Ku of the University of New Mexico and Materials and Manufacturing Directorate, Air Force Research Laboratory (AFRL/RX). These structures are a series of 2-d square titanium (Ti)/gold (Au) hole arrays with various periods (Λ=1.79, 1.89, 2.00, 2.08, and 2.33 μm) on 1μm of heavily n-doped GaAs (free electron concentration n= 2×10^{18} cm^{-3}) on a substrate of semi-insulating (un-doped) GaAs. The nominal diameter of the holes was 0.5Λ. A description of the fabrication of these structure can be found in Dr. Ku's PhD dissertation [15]. Dr. Ku got good results when simulating this structure in CST Microwave Studios for normal incidence with the approximation, $n_{d,eff} = \sqrt{\varepsilon_d'} \sim \lambda_{1,0} / \Lambda$, given in Equation (2.28). These filters were designed to be integrated with an intersubband quantum-dots-in-a-well structure to be used as a mid-infrared focal plane array. Figure 32 shows a scanning electron microscope (SEM) image of the filter with a period of 2.08μm.

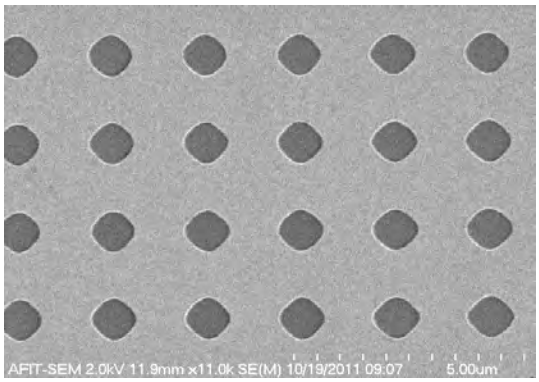

Figure 32. SEM image of the SPP transmission filter with Λ=2.08μm.

The scatter analysis of this structure will focus on the sample with a period of $2.08\mu m$. While the periodicity does change the spectral characteristics, for brevity, only one case is presented but the results can be generalized to any of the others. This chapter will present the measured results and findings for off-normal spectral polarimetric transmission of this structure. Then, an analytical approach will be taken to explain the measured results. Finally, the results from FDTD simulations will be used to enforce the analytical explanations.

Measurements

Dr. Ku showed that the spectral nature of the extraordinary transmission at normal incidence is dependent on the periodicity of the rectangular hole array. As mentioned in Chapter 2, extraordinary transmission is attributed to SPPs since the thin perforated films that exhibit this behavior are optically thick. The transmission peaks are orders of magnitude larger than can be explained by aperture theory since the size of the holes are much smaller than the wavelengths of these peaks. To verify this, spectral transmission was measured for all five structures, shown in Figure 33. The locations of the peaks correspond to Equation (2.27), simplified for $\theta_i = 0°$

$$\lambda_{i,j} = \frac{\Lambda \left| \sqrt{\frac{\varepsilon_m(\lambda_{i,j})\varepsilon_d(\lambda_{i,j})}{\varepsilon_m(\lambda_{i,j}) + \varepsilon_d(\lambda_{i,j})}} \right|}{\sqrt{i^2 + j^2}} \tag{4.1}$$

This is the form of the SPP modes most often published, rather than the more general forms in Equations (2.27) and (2.31) [17, 18, 31].

Spectral transmission measurements were made on the structure with a period of 2.08μm for $\lambda = 2-12\mu m$, angles of incidence, $\theta_i = 0°, 20°$ and $40°$, and un-polarized, p-polarized and s-polarized light. The transmission of these filters at the resonant peak is approximately 30% which is orders of magnitude higher than the classically expected result [31]. In this document, all transmission measurements of SPP structures are normalized for comparing spectral characteristics unless otherwise noted. The results from these measurement are shown in Figures 34-37. The transmission spectra from these measurements show that for s-polarization and $\phi = 0°$, the spectral peaks shift with θ_i, and for s-polarization, the peaks remain essentially unchanged. On the other hand, for $\phi = 45°$ both polarizations appear to split the spectral peak with increasing θ_i.

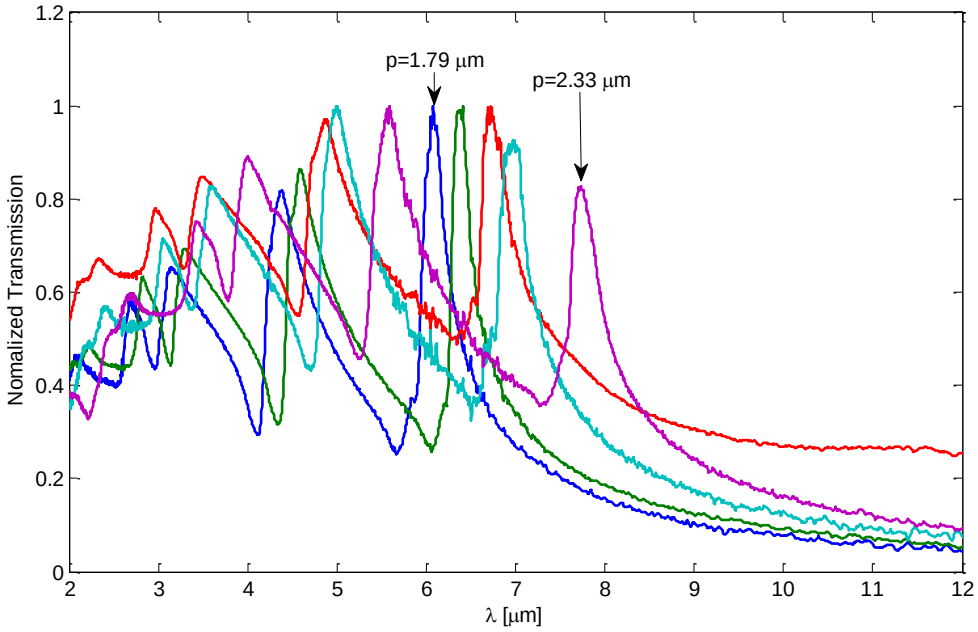

Figure 33. Measured spectral transmission of five different SPP structures with Λ=1.79, 1.89, 2.00, 2.08 and 2.33μm.

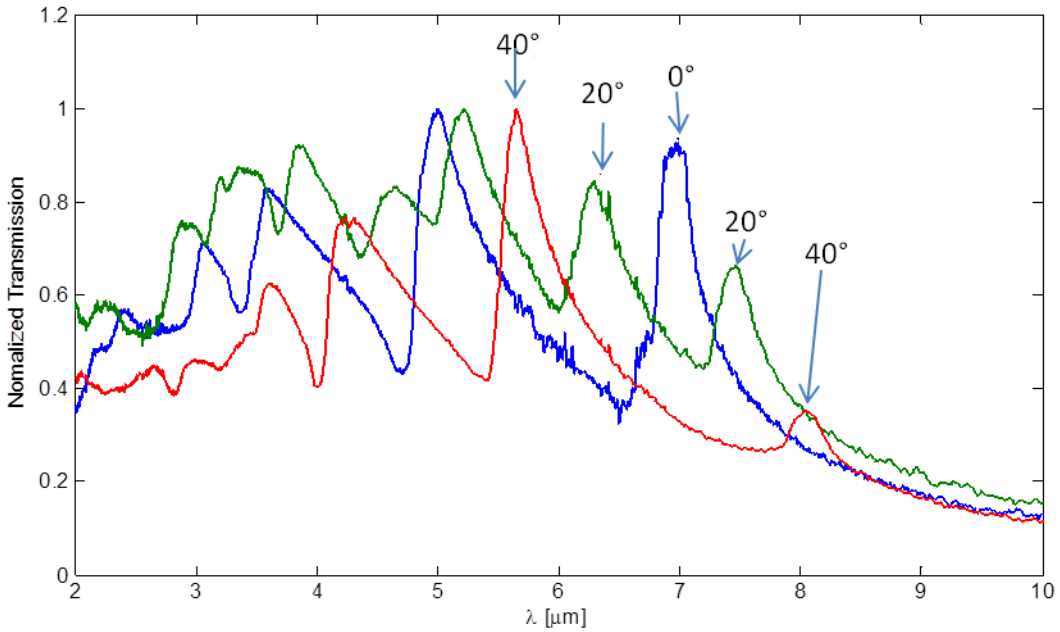

Figure 34. Measured spectral transmission of the 2.08μm period filter with φ=0° and p-polarization for θ_i=0°, 20° and 40°.

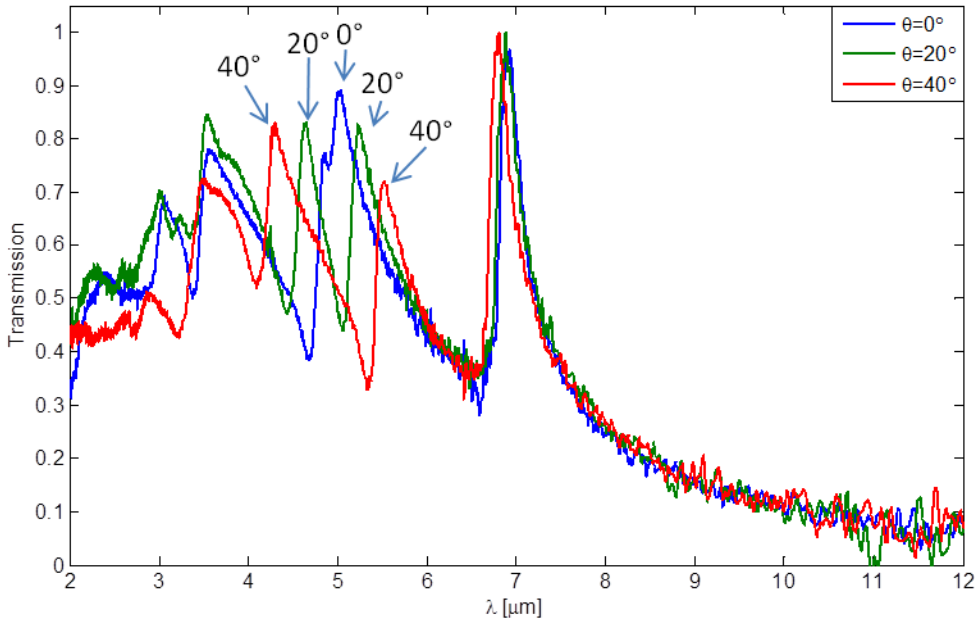

Figure 35. Measured spectral transmission of the 2.08μm period filter with φ=0° and s-polarization for θ_i=0°, 20° and 40°.

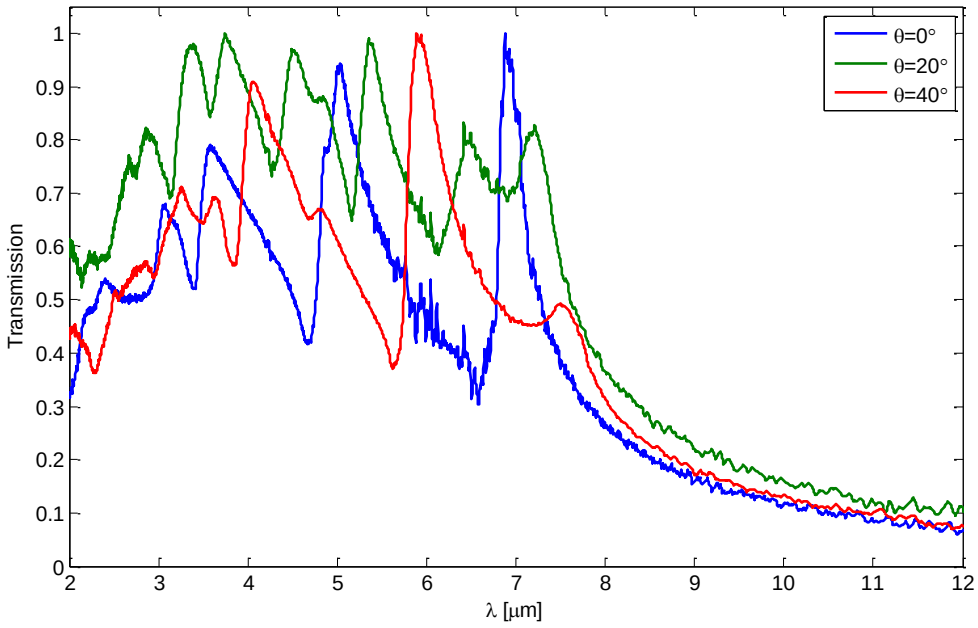

Figure 36. Measured spectral transmission of the 2.08μm period filter with φ=45° and p-polarization for θ_i=0°, 20° and 40°.

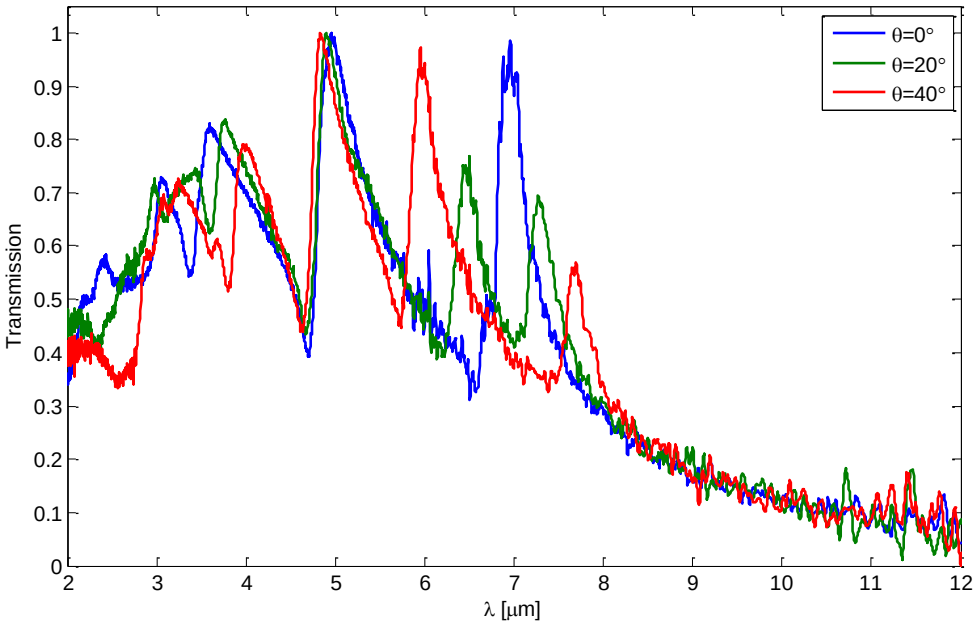

Figure 37. Measured spectral transmission of the 2.08μm period filter with φ=45° and s-polarization for θ_i=0°, 20° and 40°.

Polarimetric spectral transmission measurements were also made on this structure, giving a measured Mm. These measurements are shown in Figures 38-41. Recall Equations (2.54) and (2.55) for polarization preserving and depolarizing Mms. The green dashed lines represent a polarization preserving Mm. It can be seen that, when resonant, this structure is slightly depolarizing.

To investigate if this phenomenon is apparent in reflection, AFIT post doctoral researcher, Dr. Stephen Nauyoks, made a polarimetric BRDF measurement for $\theta_i = 20°$, $\lambda = 4.3\mu m$ and p-polarization. This measurement is shown in Figure 42 as the angular-dependant reflected Stokes vectors of three different filters, the 1.79μm (sample 1), 2.08μm (sample 2) and 2.33μm (sample 3) period structures. The s_1 and s_2 components measured and the s_3 component was calculated from

$$s_3 = \sqrt{s_o{}^2 - s_1{}^2 - s_2{}^2} \tag{4.2}$$

If this structure were not depolarizing, a $[1,1,0,0]^T$ Stokes vector would be returned, depicted by the red lines. However, these measurements show depolarization upon reflection. The x-axis is centered at the specular reflection angle (20°) and scaled by

$$x_{axis} = -\left(\log_{10}\left(\left|\theta_{reciever} - \Delta\theta_{step}\right|\right) + \pi/2 + 2*0.40103\right) \tag{4.3}$$

where $\theta_{reciever}$ is the scattered elevation angle in degrees offset by 20° and $\Delta\theta_{step}$ is the instrument step size at specular. This scaling makes the central "flat region" about ±1° around specular. The increasing depolarization at scatter angles greater than approximately ±1° has been associated with systematic apparent depolarization due to very low signal-to-noise ratio. Notice the 1.79μm period sample displays the highest

amount of depolarization. This is because the $\lambda_{1,1}$ mode for this periodicity is located at 4.3μm for $\theta_i = 20°$ from Equation (2.27).

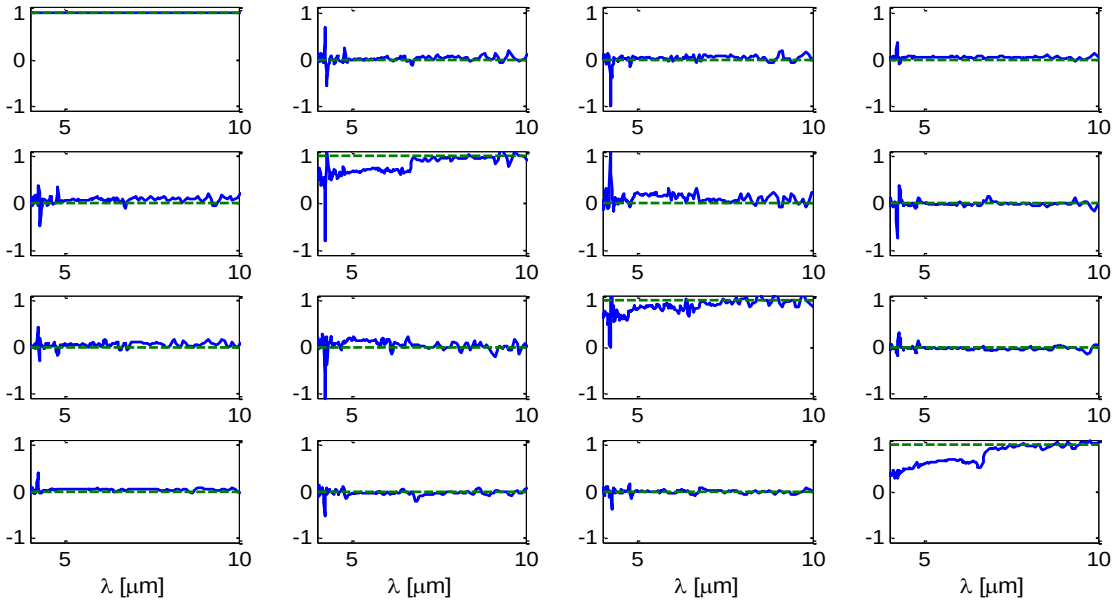

Figure 38. Measured Mm of the structure with Λ=2.08μm, φ=0° and θ_i=0°

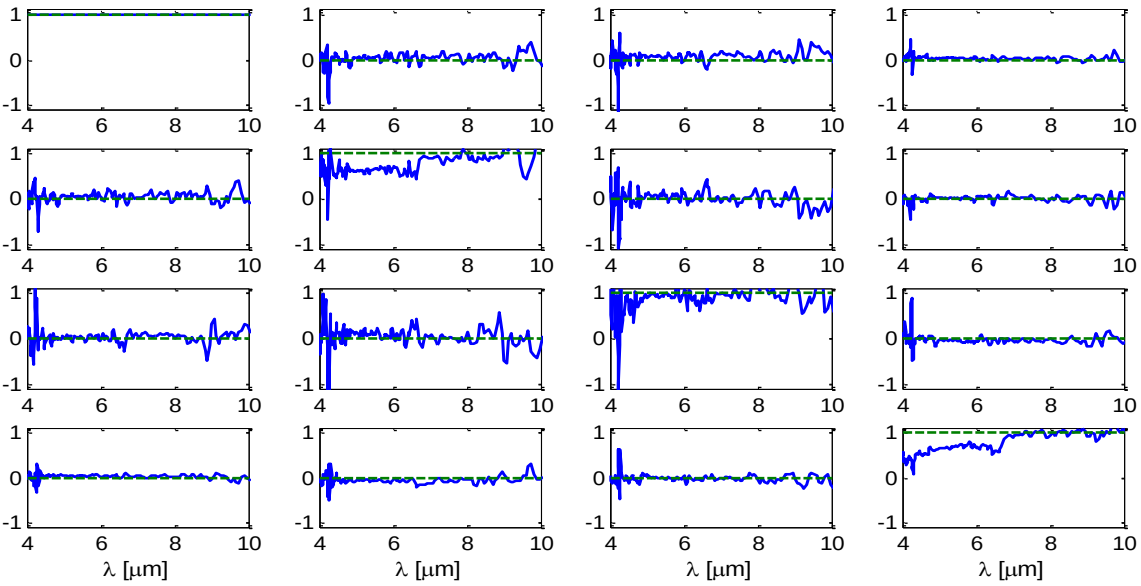

Figure 39. Measured Mm of the structure with Λ=2.08μm, φ=45° and θ_i=0°

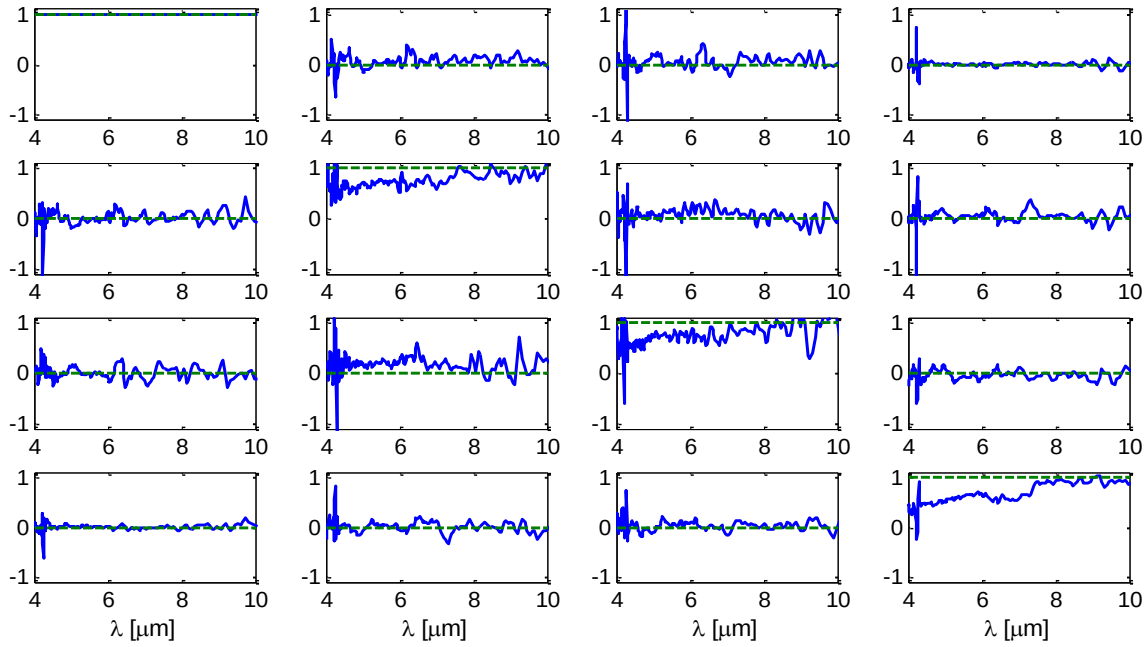

Figure 40. Measured Mm of the structure with Λ=2.08μm, φ=0° and θ_i=20°

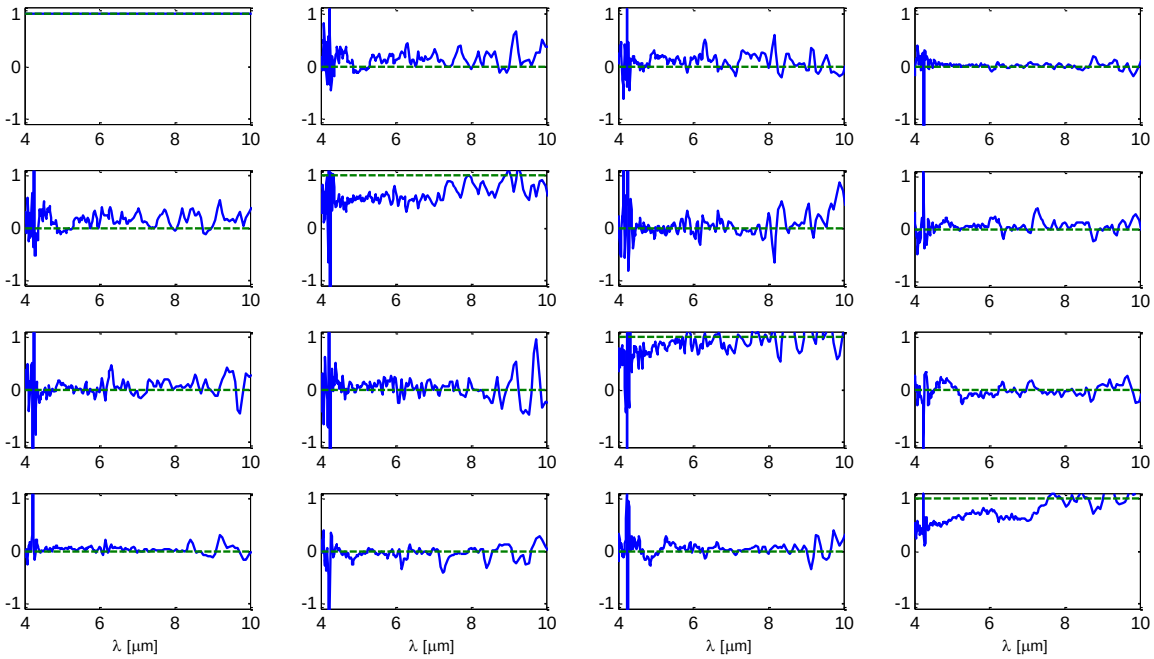

Figure 41. Measured Mm of the structure with Λ=2.08μm, φ=45° and θ_i=20°

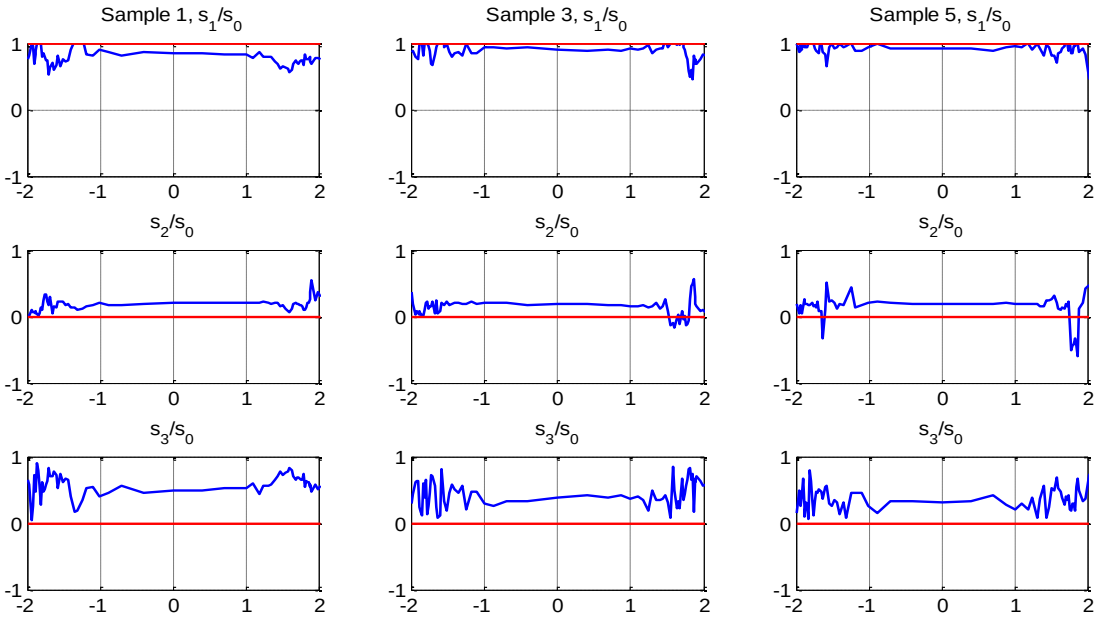

Figure 42. Measured polarimetric BRDF at λ=4.3μm of SPP structures with Λ=1.79μm (left), 2μm (middle) and 2.33μm (right). All components are normalized by dividing by s_0. The horizontal axis scaled by Equation (4.3) and centered at the specular reflection angle (20°). The red line represents a polarization preserving reflector.

Analysis

An analytical expression for the spectral location of the SPP extraordinary transmission modes was developed in Equations (2.27) and (2.31), repeated here for convenience

$$\lambda_{i,j}(\theta_{inc}) = \frac{\Lambda\left|\sqrt{\frac{\varepsilon_m(\lambda_{i,j})\varepsilon_d}{\varepsilon_m(\lambda_{i,j})+\varepsilon_d}}\right|}{\sqrt{\left(i \pm \frac{\Lambda}{\lambda_{i,j}}\sin\theta_{inc}\right)^2 + j^2}} \tag{4.4}$$

where i, j are integers, $\varepsilon_m(\lambda)$ is the permittivity of the metal film and ε_d is the permittivity of the dielectric of the interface. Also recall, if the structure coordinates are

aligned with spherical coordinates where the x-axis is aligned with $\phi_{inc} = 0$, then if $\phi_{inc} = 45°$, the resonant modes are

$$\lambda_{i,j|\phi_{inc}=45°}(\theta_{inc}) = \frac{2\left|\sqrt{\frac{\varepsilon_m(\lambda_{i,j})\varepsilon_d}{\varepsilon_m(\lambda_{i,j})+\varepsilon_d}}\right|}{\sqrt{\left(\frac{\sqrt{2}}{\lambda_{i,j}}\sin\theta_{inc} \pm i\frac{2}{\Lambda}\right)^2 + \left(\frac{\sqrt{2}}{\lambda_{i,j}}\sin\theta_{inc} \pm j\frac{2}{\Lambda}\right)^2}} \tag{4.5}$$

Also mentioned in Chapter 2, the Wood's anomaly may be apparent in the transmission spectrum, given by Equation (2.32). For this structure, the Wood's anomaly modes line up with the (1,0) and (2,0) modes with $\phi_{inc} = 0°$.

These analytical expressions are plotted in Figure 43. A careful comparison of the spectral peaks in Figures 34-37 shows that these expressions match what was measured.

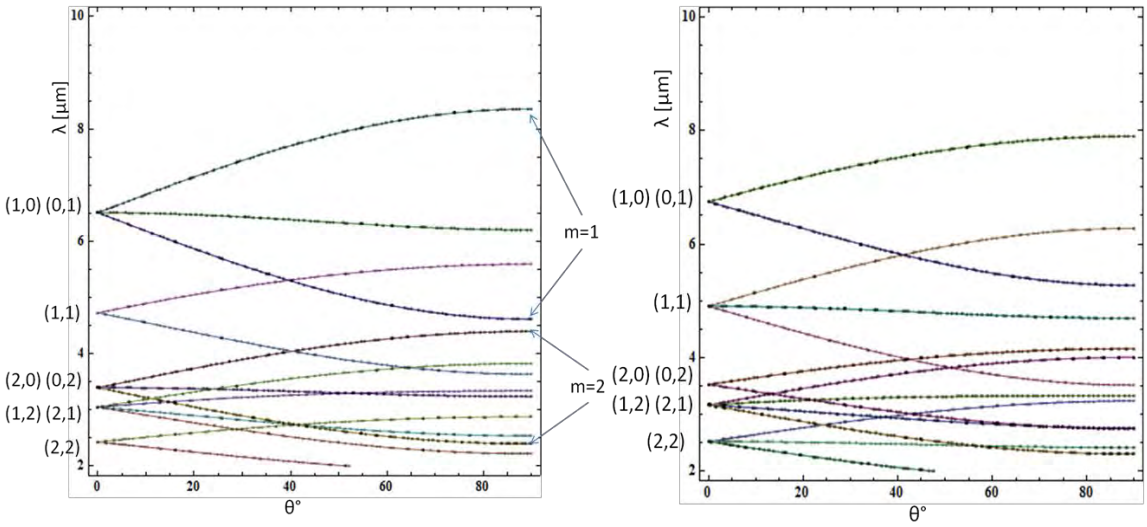

Figure 43. Calculated SPP modes for the extraordinary transmission filter with Λ=2.08μm where φ_{inc}=0° (right) and φ_{inc}=45° (left). In parentheses are the mode orders (*i, j*) and *m* is the Wood's anomaly modes. Note that the Wood's anomaly modes line up with the SPP (1,0) and (2,0) modes and the resulting transmission spectrum is a superposition of these phenomena.

Note the resemblance of this result and that of the GMRF. A closed form analytical expression for the dispersion relation of SPP extraordinary transmission is straight forward since the phenomena result from surface waves. However, the 2-d GMRF dispersion relation can only be determined numerically since its behavior is due to coupled waves in a volume. Although the theories describing the bound electric field to the gratings are different, both structures have rectangular periodicity that interacts with an incident radiation source giving similar dispersion relation forms.

FDTD Simulation

Building the FDTD simulation for as SPP extraordinary transmission filter presented some complications that were addressed before simulations matched measured results. An overview of these complications and the steps taken to overcome them is presented to provide a reference for future implementation of Lumerical's FDTD software to design and analyze this type of structures.

The FDTD model for this SPP structure has built to match the physical properties of the structure measured as prescribed by Dr. Ku. Initially, the model included the 5nm of Ti between the Au and the n-type GaAs. However, this layer did not change results. The mesh size was then increased such that the Ti was not recognized in the simulations, resulting in faster simulation run times.

Another complication was correctly estimating the refractive index of the dielectric GaAs at the metal-dielectric interface. The refractive index was first defined using the GaAs definition in Lumerical's material database, resulting in the poor results

shown in Figure 44 (left). While the overall spectrum looked similar, the location of the specular peaks did not line up with the measurements.

Recall Equation (2.28) from Chapter 2,

$$n_{d,eff} = \sqrt{\varepsilon_d'} \approx \frac{\lambda_{1,0}}{\Lambda} = \frac{7\mu m}{2.08\mu m} = 3.365 \tag{4.6}$$

This approximation defines the GaAs refractive index as un-doped as can be seen in Figure 44 (left) and did not produce good results.

A third definition for the n-type GaAs refractive index was calculated from the relation given by Zoroofchi as

$$\Delta n(E) \approx -9.6\times10^{-21} N / nE^2 \tag{4.7}$$

where N is the electron concentration, n is the refractive index of un-doped GaAs and E is the photon energy [32]. This definition resulted in simulation results closer to the measured data, but at λ=5μm, the results still did not fit well as shown in Figure 44 (right).

The fourth definition was calculated for the change in refractive index given by Bennett as

$$\Delta n = \frac{-6.9\times10^{-22}}{nE^2}\left[\frac{N}{m_e} + P\left(\frac{m_{hh}^{1/2} + m_{lh}^{1/2}}{m_{hh}^{3/2} + m_{lh}^{3/2}}\right)\right] \tag{4.8}$$

where N is the electron concentration, P is the hole concentration, E is the photon energy, m_e is the effective mass of the conduction band electrons and m_{hh}, m_{lh} are the heavy and light hole effective masses, respectively [33]. The results of these calculations are also shown in Figure 44 (right). This resulted in simulation results very close to those from Zoroofchi's definition.

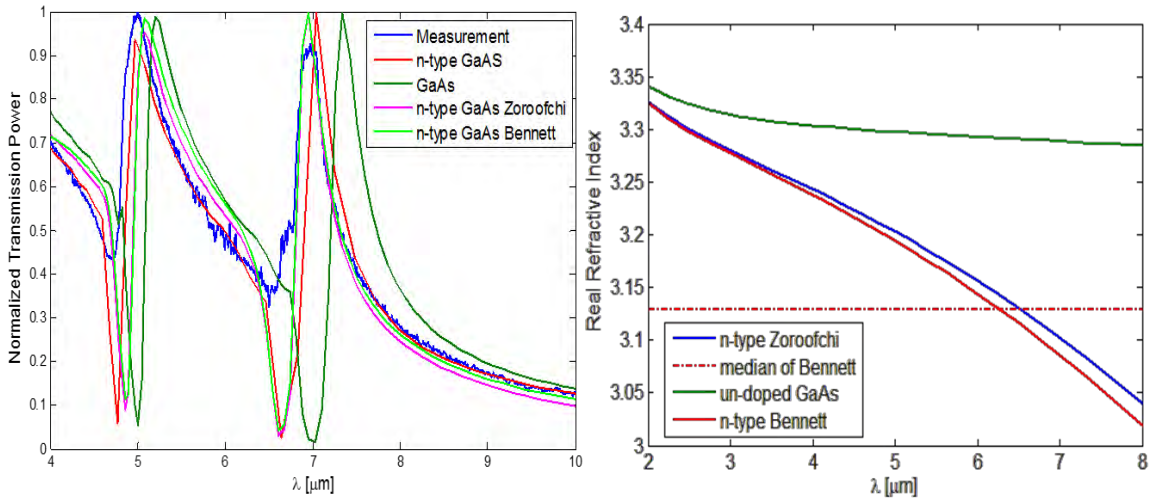

Figure 44. (left) Simulated spectral extraordinary transmission compared with the measured data comparing the fitness of simulated data with definition for the refractive index of the GaAs from Lumerical. (right) Spectral refractive index of GaAs defined by Lumerical, Zoroofchi and Bennett.

Finally, the GaAs refractive index was set to a constant $n = 3.129$ in the band of interest which is the median of Equation (4.8) across the band. This gave the best results.

After the correct model parameters were found, a full λ, θ_i sweep was run for $\phi = 0°$ and 45°, and s- and p-polarizations. The spectral transmittance and reflectance was collected with FDPMs and is shown in Figures 45 and 46. A comparison of these results to Equations (4.4) and (4.5), which are plotted in Figure 43, shows good agreement.

The absorptance of this structure was calculated from Kirchhoff's law

$$\alpha(\lambda) = 1 - \rho(\lambda) - \tau(\lambda) \tag{4.9}$$

where ρ and τ are the reflectance and transmittance and is shown in Figure 47. This structure also has selective emission properties at the lowest order mode; also from Kirchhoff's law $\alpha(\lambda) = \varepsilon(\lambda)$ where ε is the emittance. An inspection of Figure 47 shows

that the directional spectral absorptance is highest at the (1,0) and (0,1) modes. Figures 48-51 show the simulated transmission spectrums plotted with the measured data. Shown previously in Figures 34-37.

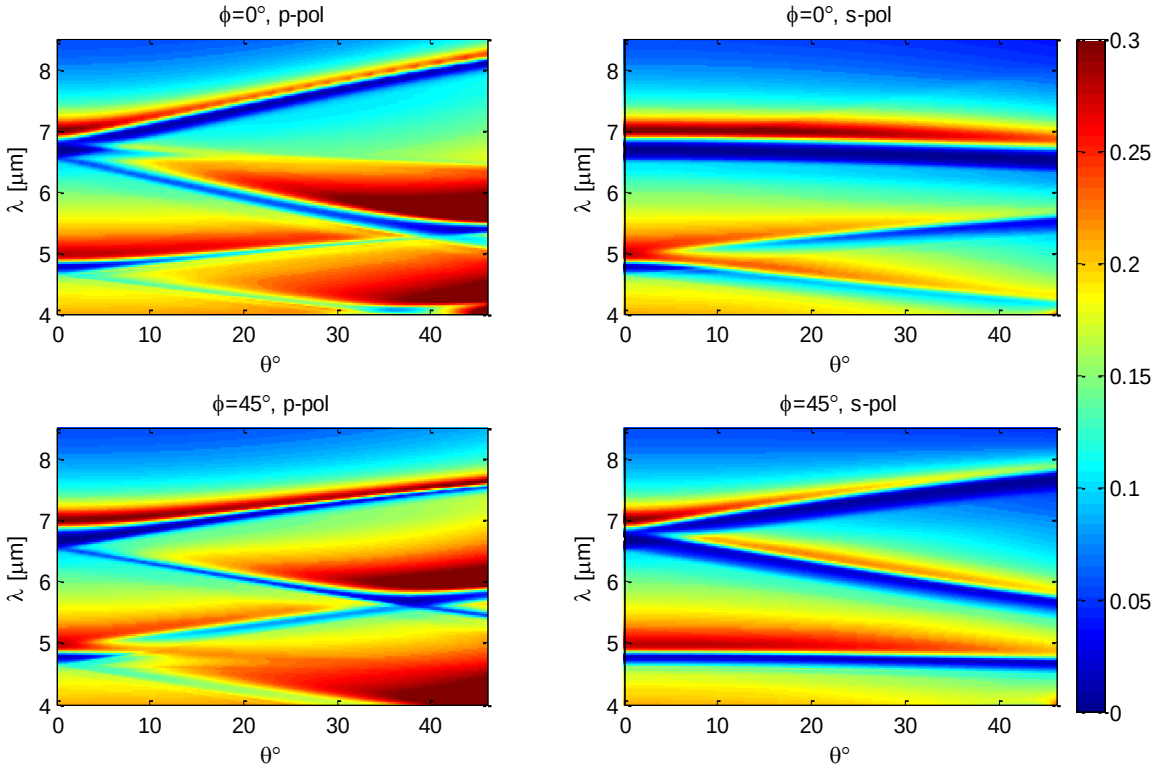

Figure 45. Simulated transmittance of the SPP filter as a function of incident angle and wavelength. Note these values are not normalized..

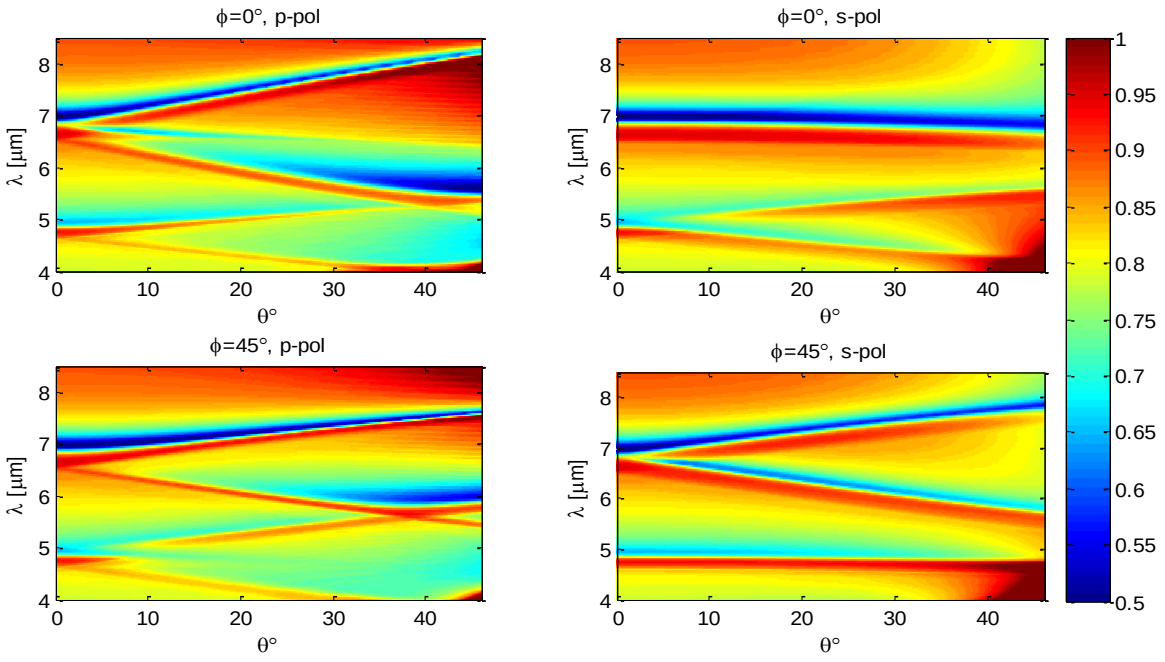

Figure 46. Simulated reflectance of the SPP filter as a function of incident angle and wavelength. Note these values are not normalized.

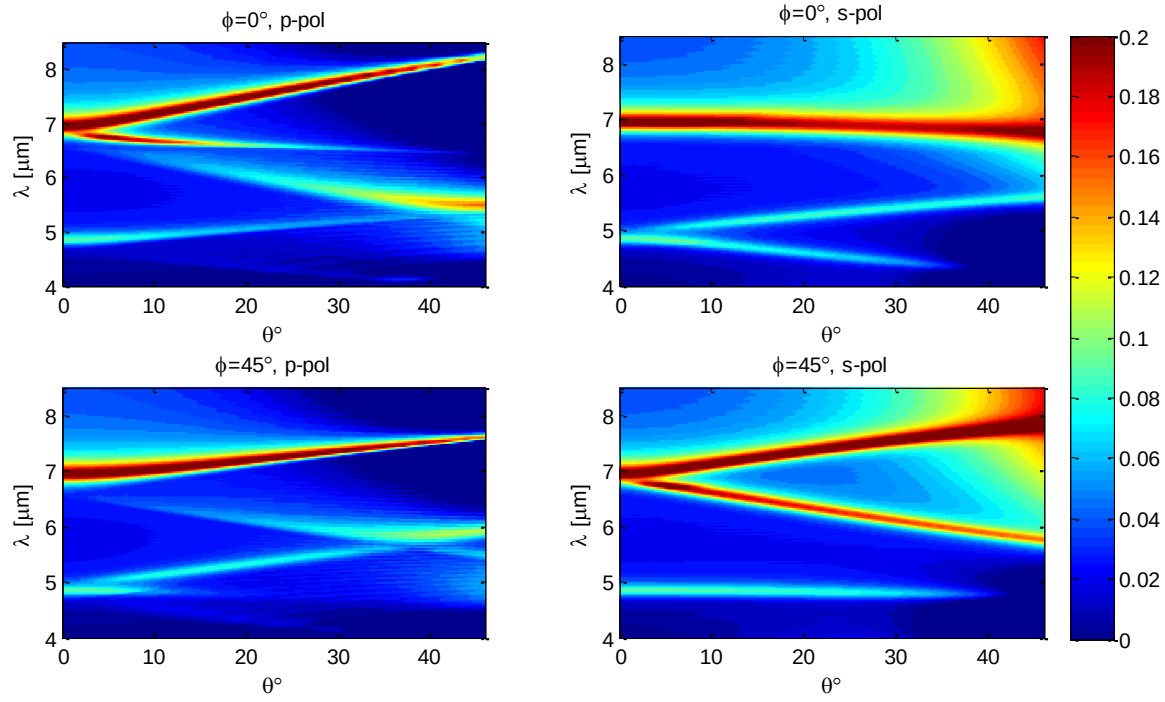

Figure 47. Simulated absorptance of the SPP filter as a function of incident angle and wavelength. Note these values are not normalized.

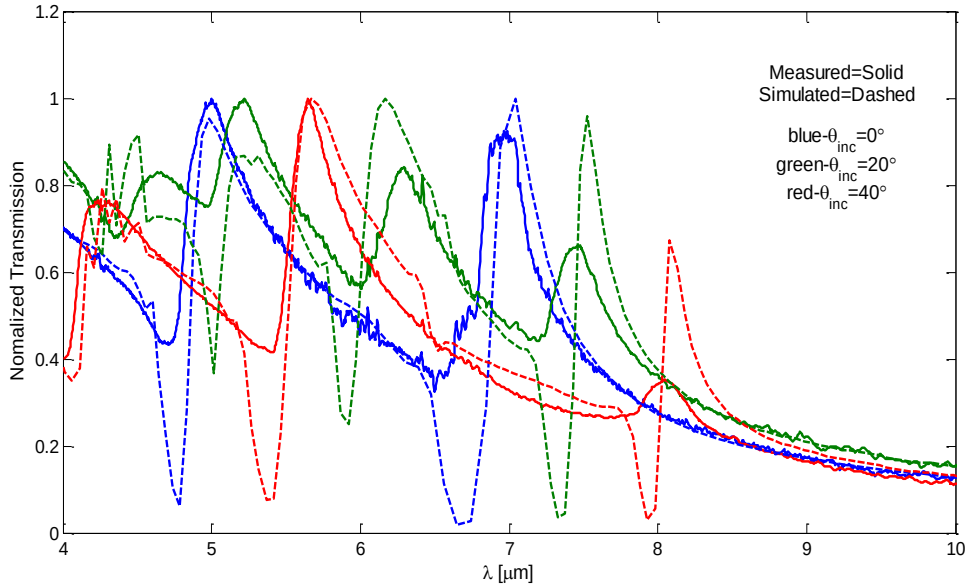

Figure 48. Simulated (dashed) and measured (solid) spectral transmission for θ_i=0° (blue), θ_i=20° (green) and θ_i=40° (red) with p-polarization and φ=0°.

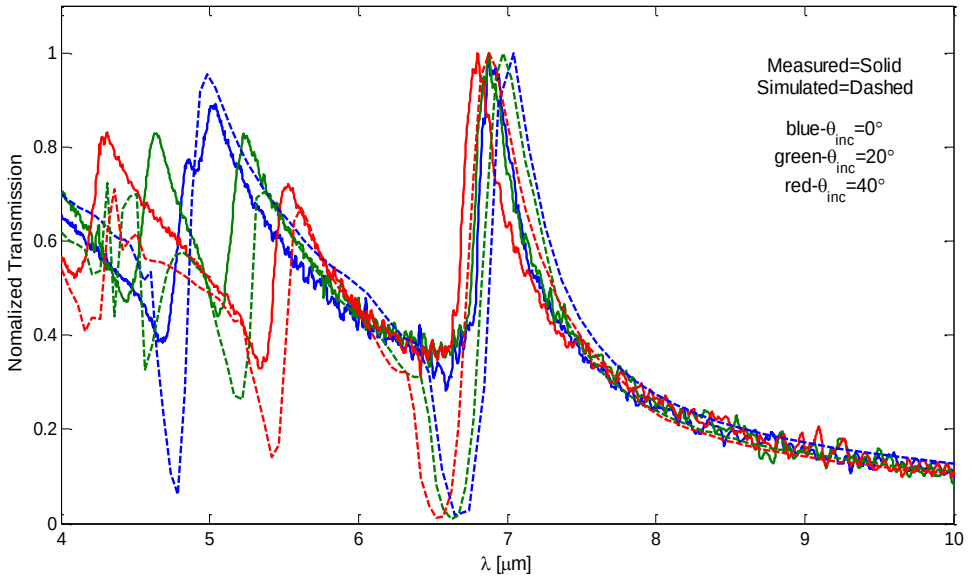

Figure 49. Simulated (dashed) and measured (solid) spectral transmission for θ_i=0° (blue), θ_i=20° (green) and θ_i=40° (red) with s-polarization and φ=0°.

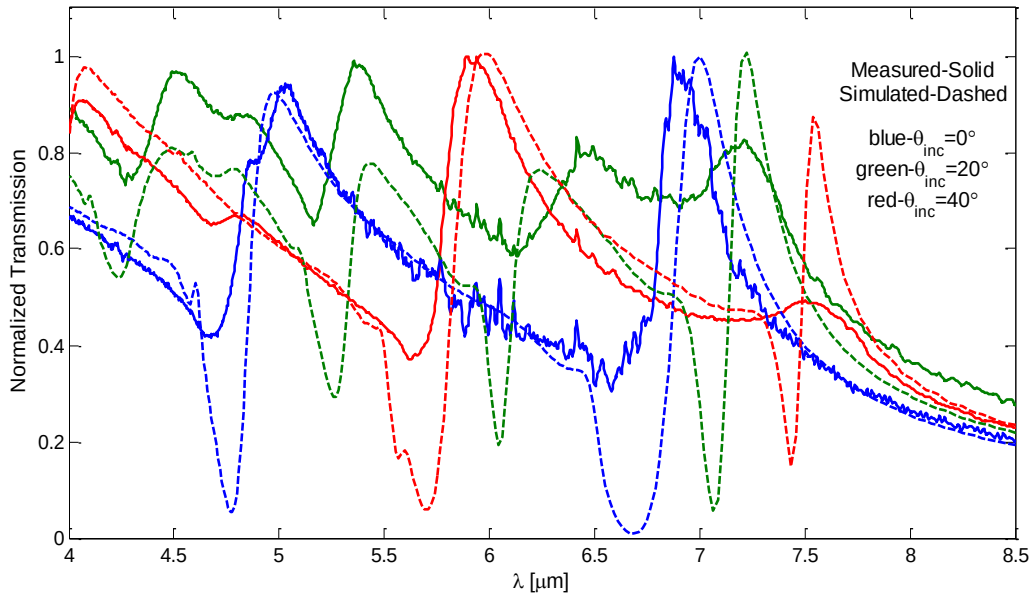

Figure 50. Simulated (dashed) and measured (solid) spectral transmission for θ_i=0° (blue), θ_i=20° (green) and θ_i=40° (red) with p-polarization and φ=45°.

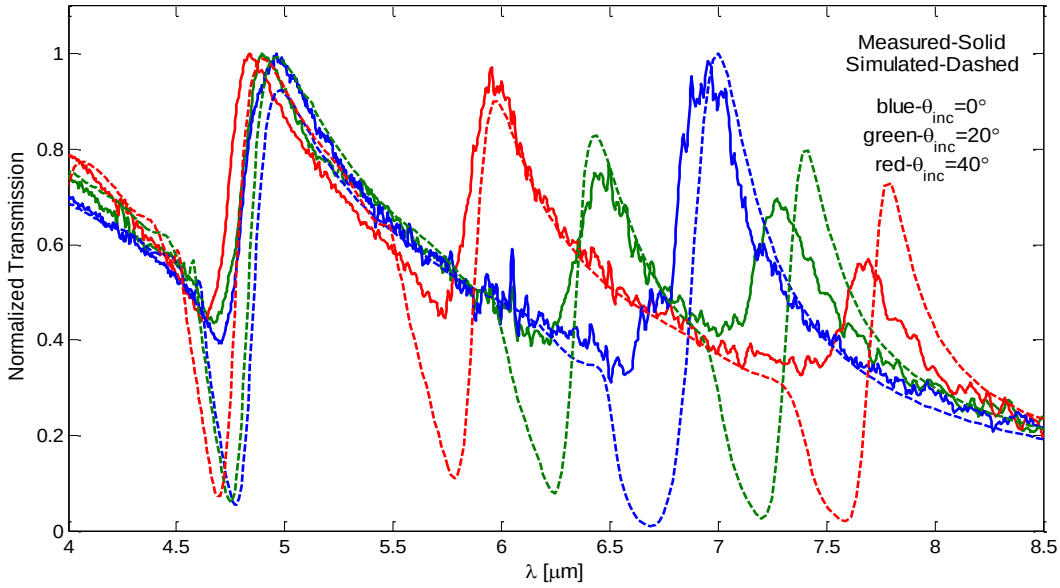

Figure 51. Simulated (dashed) and measured (solid) spectral transmission for θ_i=0° (blue), θ_i =20° (green) and θ_i =40° (red) with s-polarization and φ=45°.

The simulated results agree spectrally and in magnitude with the measurements. There are some differences at the lowest order modes, (1,0) and (0,1), as is shown in Figures 48-51. This difference may be due to the approximation of the index of refraction of the GaAs as a constant. The nulls in the simulation are much deeper than the measurements, but this could be due to the resolution of the measurements. Overall, the simulations show the potential of using Lumerical to predict the extraordinary transmission of SPP filters.

Simulating the Mm measurements also proved challenging in Lumerical, which does not have a pre-defined analysis group for a Mm measurement of a simulation. To define one, the analysis group that calculates the polarization ellipse was used. To solve for all the unknowns in the Mm (Equation (2.49)), 16 equations are required. Four known independent input and output vectors provide the 16 equations. For completeness, this simulation used six, namely, s-, p-, ±45° and right- and left-hand circular polarizations, *i.e.*

$$\begin{bmatrix} 1 \\ \pm 1 \\ 0 \\ 0 \end{bmatrix} = \text{p-/s-pol}, \quad \begin{bmatrix} 1 \\ 0 \\ \pm 1 \\ 0 \end{bmatrix} = \pm 45\text{-pol}, \quad \begin{bmatrix} 1 \\ 0 \\ 0 \\ \pm 1 \end{bmatrix} = \text{RH-/LH-pol} \tag{4.10}$$

The polarization ellipse represented in Figure 10 and repeated here in Figure 52 for convenience was used to calculate the output Stokes vectors from a simulation of one unit cell of the structure with Bloch boundaries in the x and y directions. This group calculates the grating orders' respective strengths in the far field (1 meter from structure) and converts the coordinate system from Cartesian to spherical. The sum of all grating orders

calculated is one. For each grating order, the group returns the polarization ellipse's major axis (ξ), minor axis (η) and axis angle (ψ).

In order to calculate the Stokes vectors from this analysis group, the relations

$$\begin{aligned} s_0 &= |G|^2 \\ s_1 &= p\, s_0 \cos(2\psi)\cos(2\chi) \\ s_2 &= p\, s_0 \sin(2\psi)\cos(2\chi) \\ s_3 &= p\, s_0 \sin(2\chi) \end{aligned} \tag{4.11}$$

were used, where

$$\begin{aligned} G &= \sum \text{grating orders} \\ p &= \text{degree of polarization} \\ \chi &= \frac{\pi}{2} - \tan^{-1}\left(\frac{\xi}{\eta}\right) \end{aligned} \tag{4.12}$$

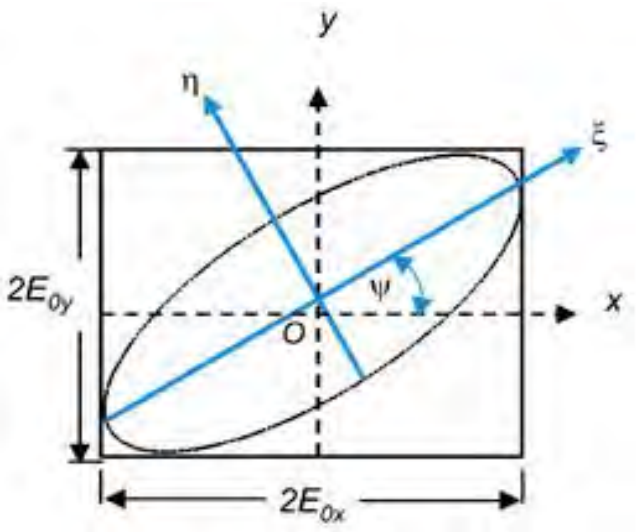

Figure 52. Polarization ellipse [27].

The definition for the degree of polarization, *p,* changes depending on the polarization of the incident field, defined as

$$p_{linear} = \left|\frac{I_\theta - I_\phi}{I_\theta + I_\phi}\right|,\ p_{45} = \left|\frac{I_{-45} - I_{+45}}{I_{-45} + I_{+45}}\right|,\ p_{circular} = \left|\frac{I_{rh} - I_{lh}}{I_{rh} + I_{lh}}\right| \tag{4.13}$$

where

$$\begin{gathered} I_\theta = \left|G_\theta\right|^2,\ I_\phi = \left|G_\phi\right|^2 \\ I_{-45} = \left|\frac{\sqrt{2}}{2}\left(G_\theta - G_\phi\right)\right|^2,\ I_{+45} = \left|\frac{\sqrt{2}}{2}\left(G_\theta + G_\phi\right)\right|^2 \\ I_{rh} = \left|\frac{\sqrt{2}}{2}\left(G_\theta - iG_\phi\right)\right|^2,\ I_{lh} = \left|\frac{\sqrt{2}}{2}\left(G_\theta + iG_\phi\right)\right|^2 \end{gathered} \tag{4.14}$$

and $G_{\theta/\phi}$ is the complex grating order strength. The degree of polarization can be completely characterized from the linear (s and p) components of the incoming radiation's polarization. From Cartesian to spherical coordinates, the linear components are equivalent to

$$\begin{aligned} G_\theta &= G_p \\ G_\phi &= G_s \end{aligned} \tag{4.15}$$

For each wavelength, θ_{inc}, ϕ_{inc} and polarization, the Stokes vector for each grating order was calculated, weighted according to the grating order's strength, and then summed. By performing this type of algorithm, if a particular grating order is scattered into a different polarization state, then the degree of polarization for that order will be less than one and it will show up in the end as depolarizing contribution. To determine the Mm, the input and output Stokes vectors were stacked into two 4×6 matrices, and

the input Stokes matrix was then inverted via the Moore-Penrose pseudoinverse to give the Mm solution.

$$\begin{bmatrix} s'_{0,p} & s'_{0,s} & s'_{0,+45} & s'_{0,-45} & s'_{0,rh} & s'_{0,lh} \\ s'_{1,p} & s'_{1,s} & s'_{1,+45} & s'_{2,-45} & s'_{1,rh} & s'_{1,lh} \\ s'_{2,p} & s'_{2,s} & s'_{2,+45} & s'_{3,-45} & s'_{2,rh} & s'_{2,lh} \\ s'_{3,p} & s'_{3,s} & s'_{3,+45} & s'_{4,-45} & s'_{3,rh} & s'_{3,lh} \end{bmatrix} = \bar{M}m \begin{bmatrix} s_{0,p} & s_{0,s} & s_{0,+45} & s_{0,-45} & s_{0,rh} & s_{0,lh} \\ s_{1,p} & s_{1,s} & s_{1,+45} & s_{2,-45} & s_{1,rh} & s_{1,lh} \\ s_{2,p} & s_{2,s} & s_{2,+45} & s_{3,-45} & s_{2,rh} & s_{2,lh} \\ s_{3,p} & s_{3,s} & s_{3,+45} & s_{4,-45} & s_{3,rh} & s_{3,lh} \end{bmatrix}$$

$$\Rightarrow \bar{M}m = \bar{S}'\,\bar{S}^{\dagger} \tag{4.16}$$

where $\bar{S}$ is the input Stokes matrix, $\bar{S}'$ is the output Stokes matrix and $\bar{S}^{\dagger}$ is the pseudoinverse of $\bar{S}$.

The simulated results of this analysis are shown in Figures 53-56 along with the measured results previously shown in Figures 38-41 and the representation of a polarization preserving Mm (from Equation (2.54)) by the green dashed line.

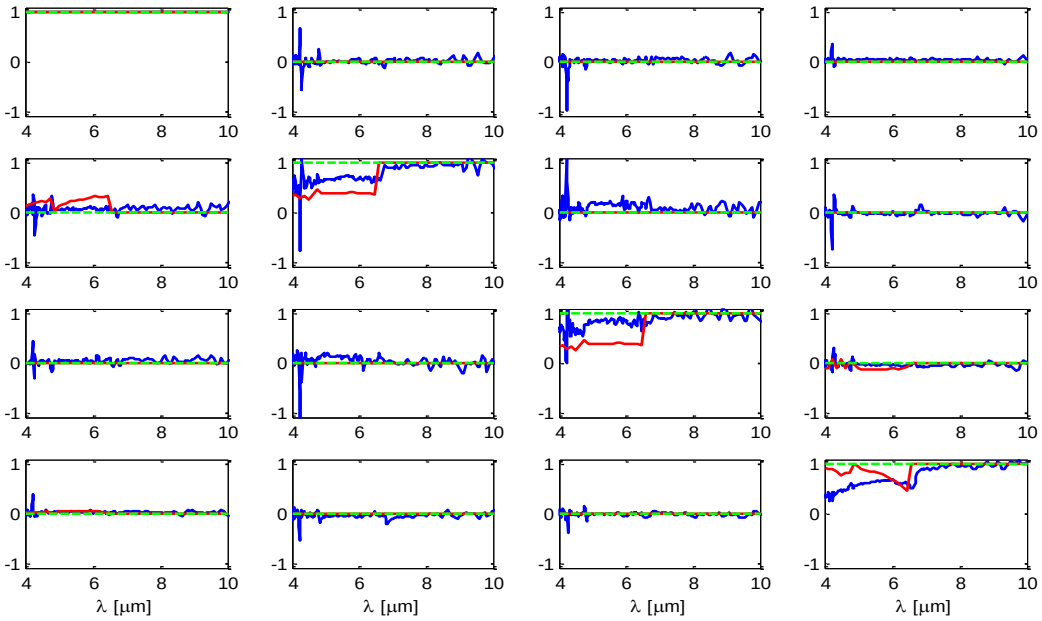

Figure 53: Measured (blue) and simulated (red) Mm of the SPP structure with Λ=2.08μm, φ=0° and θ_i=0°

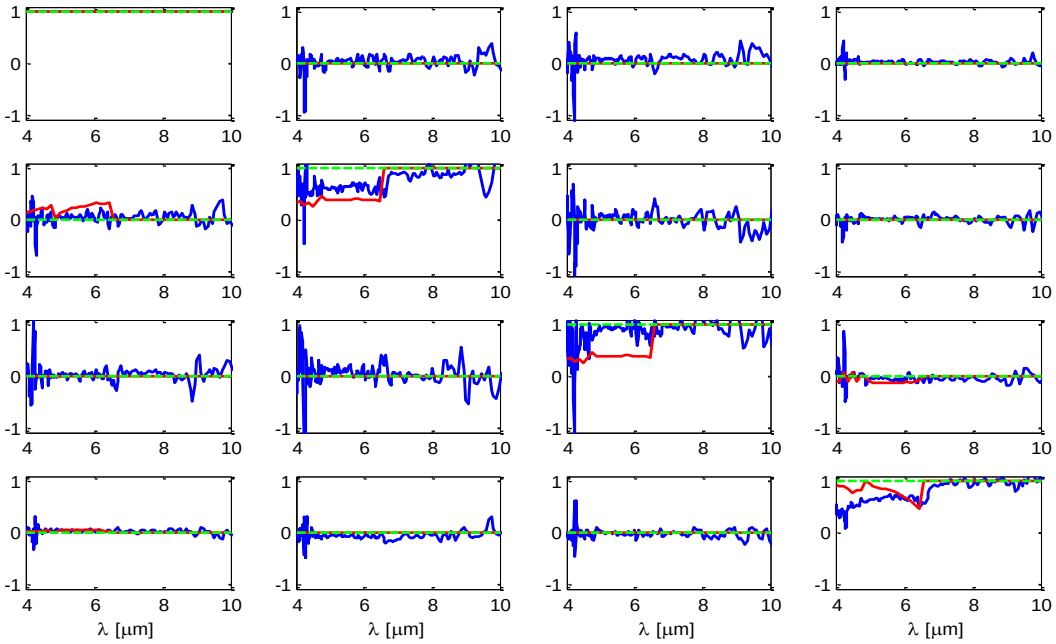

Figure 54. Measured (blue) and simulated (red) Mm of the SPP structure with Λ=2.08μm, φ=45° and θ_i =0°

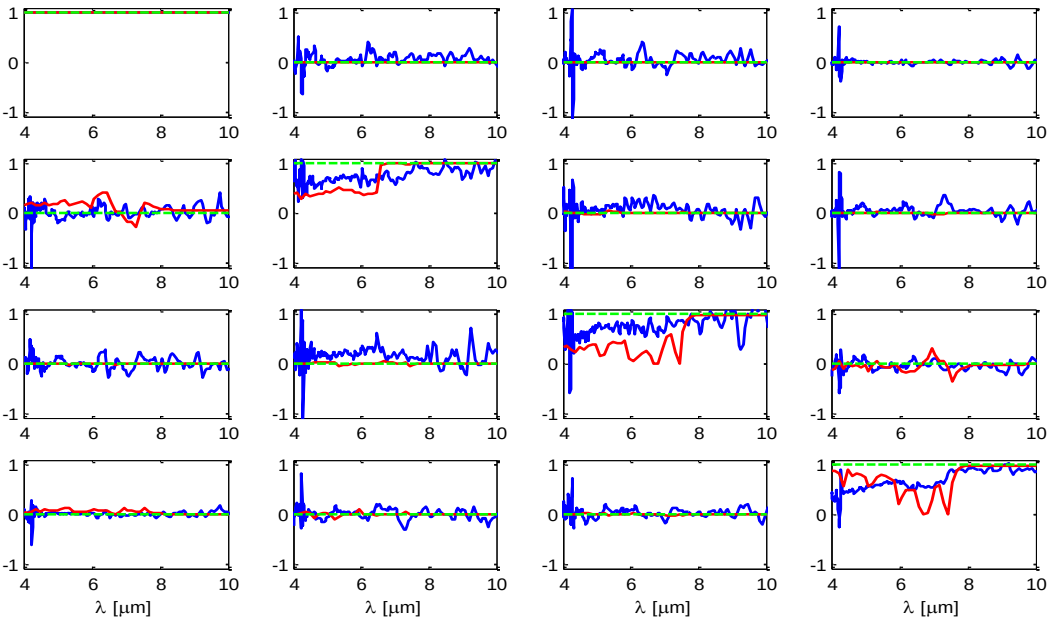

Figure 55. Measured (blue) and simulated (red) Mm of the SPP structure with Λ=2.08μm, φ=0° and θ_i =20°

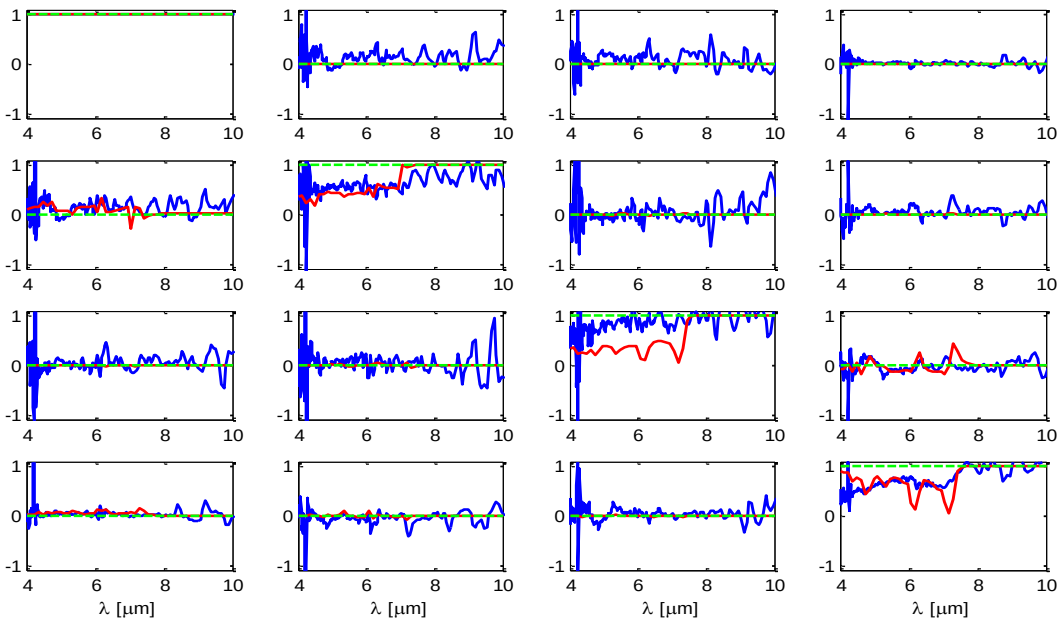

Figure 56. Measured (blue) and simulated (red) Mm of the SPP structure with Λ=2.08μm, φ=45° and θ_i =20°

The condition number was computed for the input Stokes matrix. A useful interpretation of the condition number of a matrix is that the reciprocal, $1/\mathrm{cond}(A)$, measures, in a relative sense, how close A is to being singular. The condition number of the identity matrix is 1, and the condition number of a singular matrix is +∞. [34]. Using the matrix 2-norm and the pseudoinverse the condition number for a matrix is

$$\mathrm{cond}(A) = \|A\| \|A^{\dagger}\| \tag{4.17}$$

The condition number of these matrices was 1.7, indicating they are relatively non-singular.

While there is reasonable agreement between the measured and simulated results, the simulation results do not align exactly with the measured results. There are two reasons suspected for this discrepancy. First, the uncertainty and variance in the measured

data is not known. These measurements were made by AFIT post doctoral researcher, Dr. Stephen Nauyoks, and PhD student, Capt Jason Vap, at Munitions Directorate, AFRL (AFRL/RW), Eglin AFB Florida. The advice from the AFRL/RW was to interpret the data as a general trend and not an exact measured data set. To gain an idea of how much uncertainty and variance were in the measured data, the degree of polarization, *p*, for six different Stokes vectors was examined for each measured Mm. This was calculated by multiplying the measured Mm by four independent polarization states, for example

$$\bar{S}_{in} = \begin{bmatrix} 1 & 1 & 1 & 1 & 1 & 1 \\ 1 & -1 & 0 & 0 & 0 & 0 \\ 0 & 0 & 1 & -1 & 0 & 0 \\ 0 & 0 & 0 & 0 & 1 & -1 \end{bmatrix}$$
$$\bar{S}_{out} = \bar{M}m\,\bar{S}_{in} \tag{4.18}$$

p can then be directly calculated from

$$p = \frac{1}{s_{0,i}}\sqrt{{s_{1,i}}^2 + {s_{2,i}}^2 + {s_{3,i}}^3} \tag{4.19}$$

where $[s_{0,i}, s_{1,i}, s_{2,i}, s_{3,i}]^T = \vec{s}_i$ and i =1-6 representing each input polarization. This calculation results is six $p(\lambda)$ for each Mm, one for each polarization input, totaling the 24 $p(\lambda)$ shown in Figure 57. The expected result is $0 < p(\lambda) < 1$. Figure 58 shows the simulated $p(\lambda)$ using the same calculation. Figure 59 shows the average degree of polarization for all four Mms as functions of wavelength for the measurement and simulation.

The depolarizing nature of this SPP extraordinary filter when resonant can be seen from Figure 59. Although the noise in the measured data makes this effect less

noticeable, both the measured and simulated data show a depolarizing effect through the SPP modes range of resonance (<7.5μm).

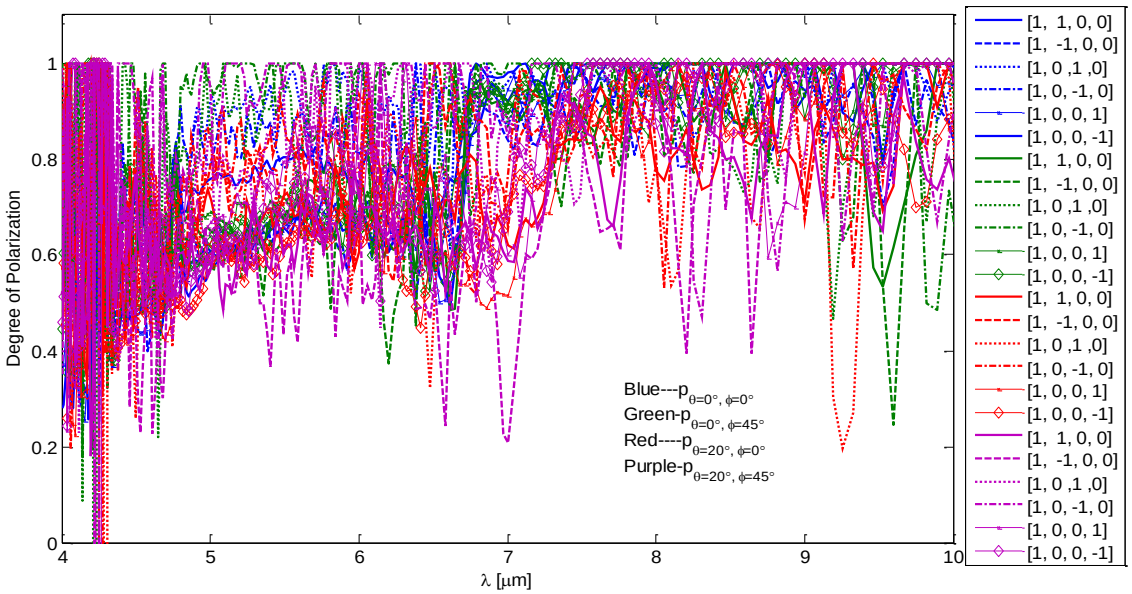

Figure 57. Calculated degree of polarization, *p*, of the measured Mms for 6 different polarization inputs.

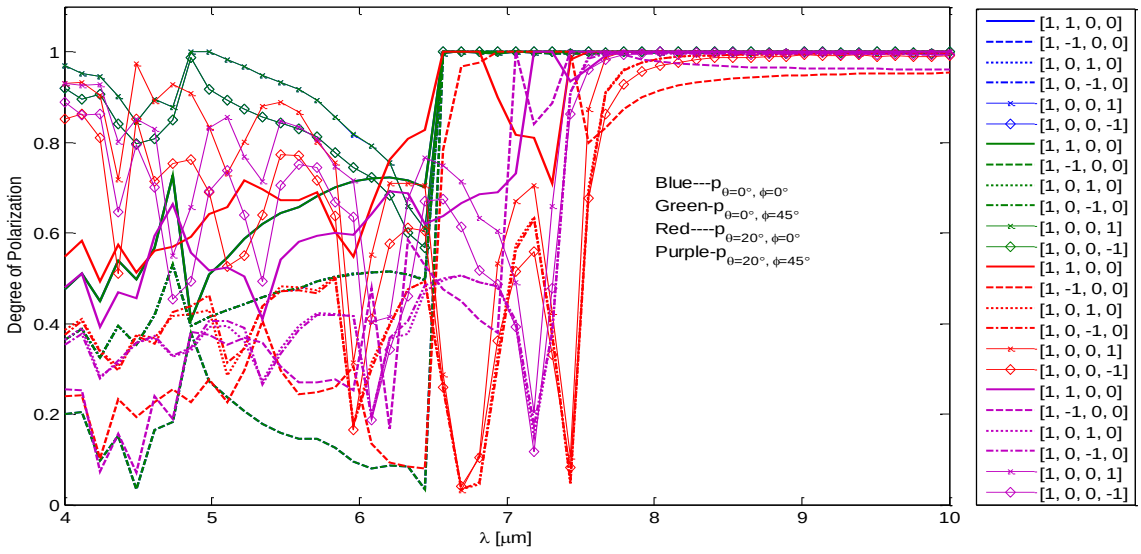

Figure 58. Calculated degree of polarization, *p*, of the simulated Mms for 6 different polarization inputs.

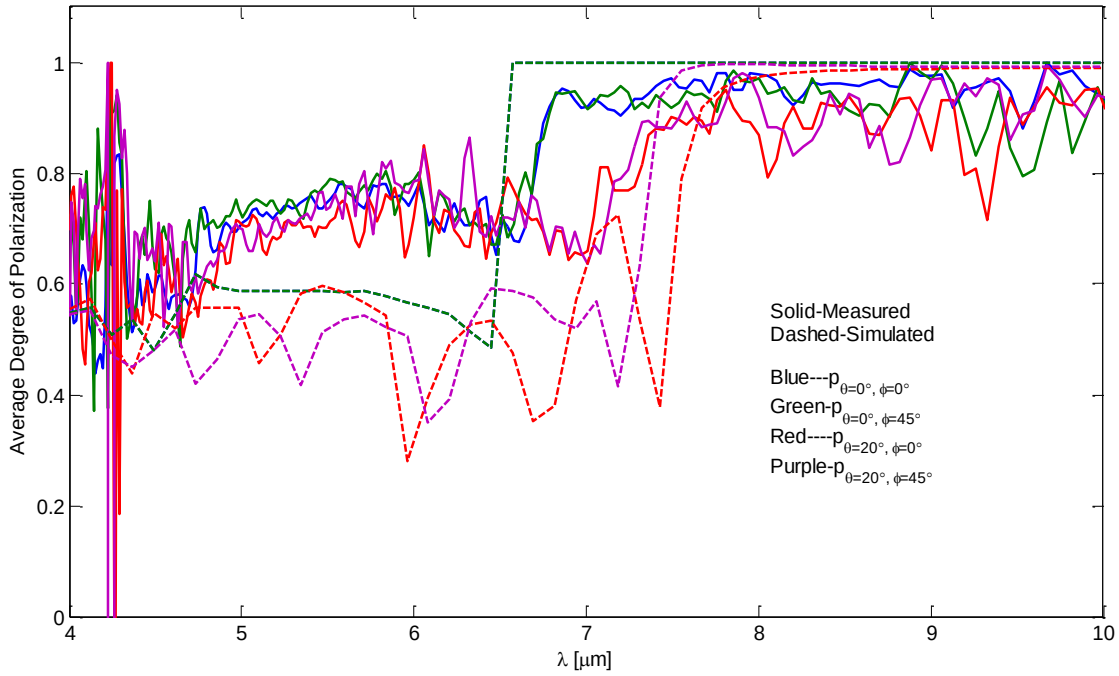

Figure 59. Average calculated degree of polarization, *p*, of the simulated and measured Mms.

Since this SPP filter is not expected to be circular polarizing, the degree of linear polarization was calculated from

$$p_{lin} = \frac{1}{s_0}\sqrt{s_1^{\,2} + s_2^{\,2}} \tag{4.20}$$

Only linearly polarized input Stokes vectors were used (s-/p- and ±45-polarizations). The results for each Stokes vector were averaged for each Mm and are plotted in Figure 60. This result emphasizes the depolarizing nature of the SPP filter when resonant, which can be seen by comparing the degree of polarization (Figure 59) to the degree of linear polarization (Figure 60).

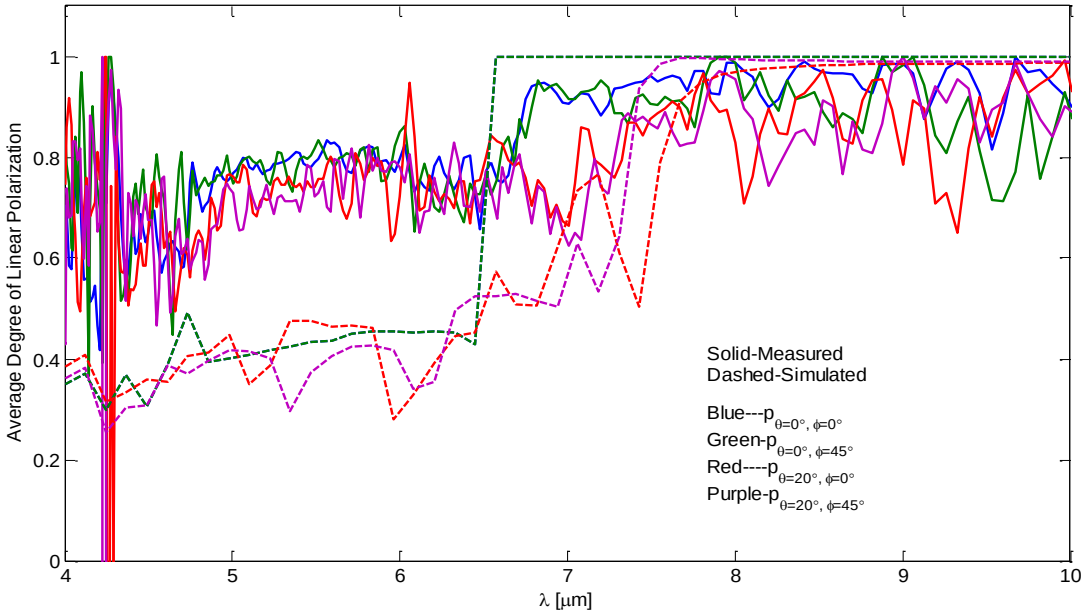

Figure 60. Average degree of linear polarization of the measured and simulated Mms for 4 different linear polarization inputs.

A second possible reason for the discrepancy between the measured and simulated Mm results is a difference between the measured and simulated collected grating orders. The technique used in the simulation includes all grating orders scattered into the transmission hemisphere while the measurement only includes grating orders scattered onto the detector. However, in conclusion, while the measured and simulated results of the Mm do not exactly match, they do both show that the SPP structure is slightly depolarizing when resonant.

Conclusion

This chapter showed that the theoretical analysis of Chapter 2 and the relations presented for off-normal incidence of light on an SPP structure give a good prediction for the location of the peaks in the measured and simulated extraordinary transmission

spectrum. This relation can easily be extended to any SPP structure with a corrugated surface by adjusting the grating momentum vectors, highlighting the fact that the location of these modes is determined by the interaction between the grating and the incident electric field. Also shown was the depolarizing characteristics of SPP structures when resonant.

While these results are very intuitive when explained in the framework presented in this chapter, at the time of this research, a similar presentation of all these concepts brought together could not be found. All of these phenomena need to be considered if integrating an SPP into an optical system, especially if off-normal incidence is a possibility. This chapter provides a complete compilation of analysis for off-normal incident light on corrugated-surface SPP structures.

V. Conclusions and Recommendations

The goal of this research was to analyze unique optical measurements of off-normal incidence radiation upon nano-/micro-structured materials and provide insight into their operational characteristics. Two different types of structured materials were obtained and measured to determine angular and frequency spectrums. These measurements were then compared to rigorous EM simulation models which essentially duplicated the characteristic spectra. From these data, analytical theory was developed to describe the characteristics exhibited for off-normal incident light. The theoretical model yielded very good results for the SPP structure. An approximation was also developed for the GMRF PC that predicted the location in angle of incidence and wavelength of the unique BSDF measured by Lamott. To further corroborate this result, more measurements are needed.

Contributions of Research

The GMRF showed a unique scatter pattern in the BSDF at a specific wavelength and angle of incidence. FDTD simulation and spectral transmission measurements showed that this phenomenon could not be attributed to the theoretically defined resonant mode typically used for a GMRF. Through a simulation-based analysis, it was determined that this phenomenon could be attributed any lower order coupled mode for off-normal incidence greater than 5°. This phenomenon scales dependent on angle of incidence and wavelength in simulations and is expected to in measurements.

The SPP structure's resonant surface modes were shown to shift spectrally with incidence angle depending on polarization. For incident light parallel to the grating

periodicity, it was shown that the asymmetric modes split with incident angle for p-polarization and remain essentially unchanged for s-polarization, while the symmetric modes split regardless of polarization. When light is incident 45° from the grating periodicity, the symmetric modes split for p-polarization and remain unchanged for s-polarization, while the asymmetric modes split. These results were shown in measurements, simulations and analytical solutions. Mm measurements and simulations for this structure were also presented. This structure is slightly depolarizing when the SPP modes are resonant.

Conclusion of Research

While there are many theoretical publications on the highly touted unique optical properties possible with nano-/micro-structured materials, it is not clear how these properties extend to angles of incidence off-normal. One example of this is the use of GMRFs as laser protection filters. Given the results of this and other research done at the Air Force Institute of Technology, the implications of exciting a "resonant angle" mode in the filter within an operational environment need to be considered. Complete characteristics of this particular structure were not noticed before the unique measurement based analysis done by the Air Force Institute of Technology. This research provided an approximation to predict the mode that caused the unique BSDF pattern. This approximation could be incorporated into a BSDF model to predict scatter from GMRFs.

Even intuitive characteristics like the slightly depolarizing nature of SPP filters when resonant, if not considered, could impact potential design parameters. The process

of determining the off-normal characteristics compiled in this thesis can be extended to any nano-/micro-structured material. Determining the angle and polarimetric dependant characteristics of these materials is vital as they become incorporated into operational systems.

Recommendations for Future Research

As part of this research effort, a BSDF searching and fitting algorithm was developed, described in Appendix A, to fit the BSDFs of these and other nano-/micro-structured materials to models loaded in the National Institute of Standards and Technology (NIST) ScatMech BSDF library. Due to time constraints and the resulting scope of this research, it was not included in the body of this document. This algorithm can be incorporated into a dynamic data driven BSDF data collection system. This system measures a small set of data, then uses this data to search a BSDF library for a set of BSDFs that best fit the data. By determining the variance between these models, it gives the measurement system the next best set of measurements to take. By iterating this process, the system converges on the best BSDF model. The development of this system will provide much better fits BSDF in much less data collection time. This type of BSDF model fitting algorithm could also be extended to defining and fitting periodic structure specific models to measured samples.

The development of a BSDF model for the GMRF, SPP filter and other nano-/micro-structured devices was an initial goal of this research effort. For the GMRF, the exact characteristics of the unique scatter pattern where not simulated here. The development of an equation that predicts this unique pattern would be key to developing

a BSDF model. Spectral reflection measurements could then be used to identify the specific angle/wavelength dependence of any unique pattern. This dependence could then be incorporated into a RCW effective BSDF model like those contained in ScatMech.

Summary

This research considered off-normal incidence of light on two separate types of nano-/micro-structured materials. By incorporating the methods, analyses and results presented, the design of future materials can be improved by considering this angular dependence, and the desired or undesired results. While the Air Force Institute of Technology continues to increase its nano-/micro-fabrication capabilities with the Air Force Research Laboratory, the results from this research will enable a better understanding of these structures and lead to better designs.

Appendix A. Particle Swarm Optimization Algorithm

In order to validate the need for a new BSDF model for these structure a complete evaluation of existing models needs to be done. Dr. Thomas Germer at The National Institute of Standards and Technology has developed a BSDF library in C++ called ScatMech, which contains multiple BSDF model classes, sub-classes and distribution functions. A hierarchy representation of ScatMech is shown in Figure 61. Each model has multiple parameters for fitting. ScatMech was developed as a tool to model scatter from structures with known physical parameters, such as surface roughness, and as a calibration tool for use with BSDF measurement systems . To fit measured BSDFs to this immense search space the particle swarm optimization (PSO) algorithm was adjusted to fit the particulars of the search space. The basic theory for the PSO algorithm was initially developed to model the movement of insect swarms or bird flocks. Robinson and Rahnat-Samii extended the algorithm to electromagnetic optimization problems [35]. PSO randomly initializes a set of agents or particles at different locations or parameters sets within the search space, each with random velocity vectors or step sizes to the next set of parameters. Each particle then determines its own fitness value and the best overall fitness is also determined, these values are then used to determine the next velocity vectors for each particle defined by

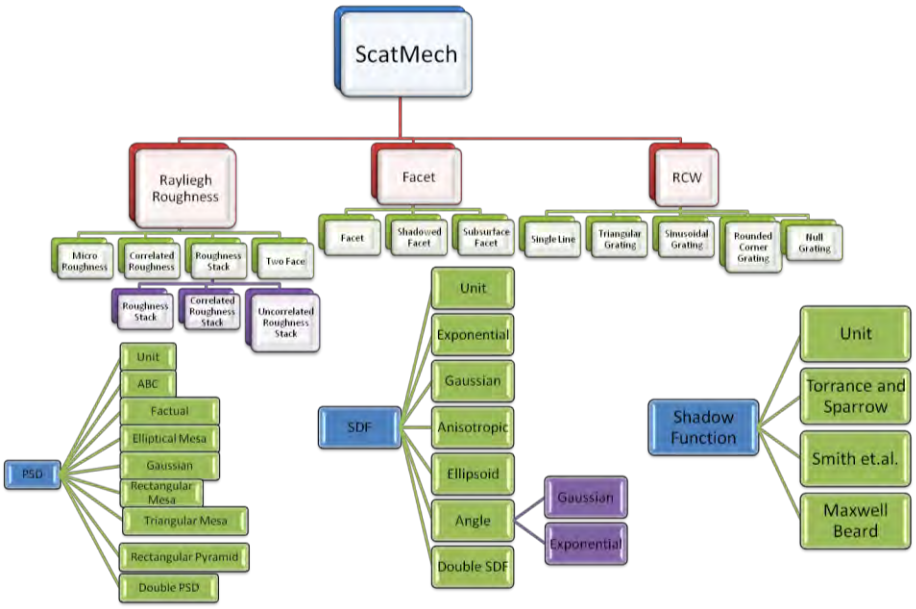

Figure 61. Hierarchy representation of ScatMech, a BSDF model library developed by Thomas Germer at The National Institute of Standards and Technology.

$$v_{n+1} = w * v_n + c_1 * \text{rand} * (p_{best,n} - x_n) + c_2 * \text{rand} * (g_{best,n} - x_n) \tag{6.1}$$

where w is the inertial weight and steps from 0.9 to 0.4 linearly as the PSO runs, it determines the amount of time each particle explores its own location compared to the global search space. c_1 and c_2 are scaling factors which determine the relative pull between each agents personal best and the global best and rand is a randomly generated number between 0 and 1. At the end of each generation each particle's location is updated by

$$x_{n+1} = x_n + \Delta t * v_n \tag{6.2}$$

where Δt is the time step, for this research chosen to be 1. Figure 62 shows a flow diagram of the algorithm. When using this algorithm in physically defined problems it becomes imperative to set boundary conditions which constrict the movement of the

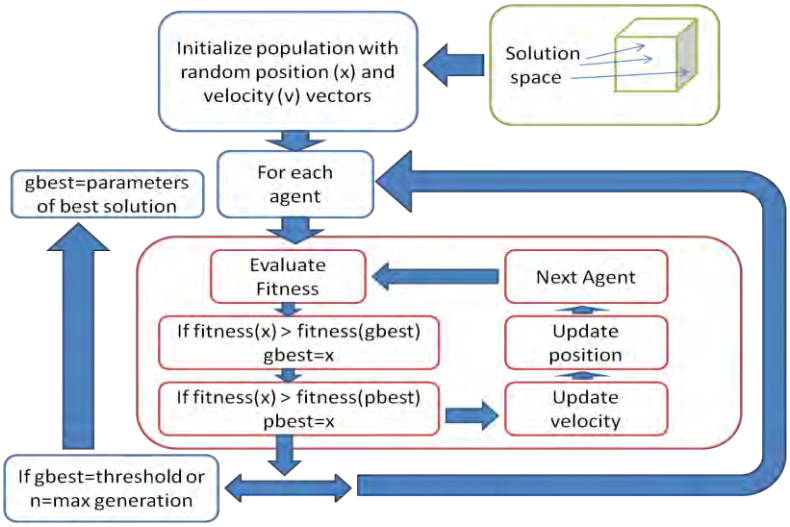

Figure 62. Flow diagram of the particle swarm optimization (PSO) algorithm used to search and fit BSDF models to the ScatMech library.

particles to physically meaningful parameters within the search space or ignoring solutions for those parameters. Both methods were tested in this development and it was found that a hybrid worked best for searching ScatMech. The parameters that represent lengths or areas are bounded while other parameters such as exponential variables aren't bounded but if they produce an unphysical solution they are ignored. The results from this effort are shown in Figures 67-71.

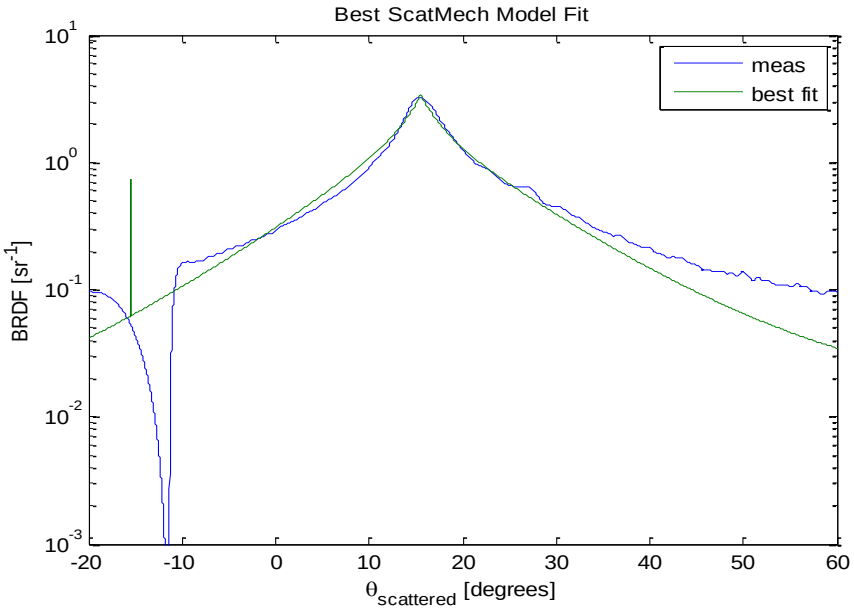

Figure 63. ScatMech model fit to measurement of diffuse aluminum plate with λ=633nm and θ_i=18°.

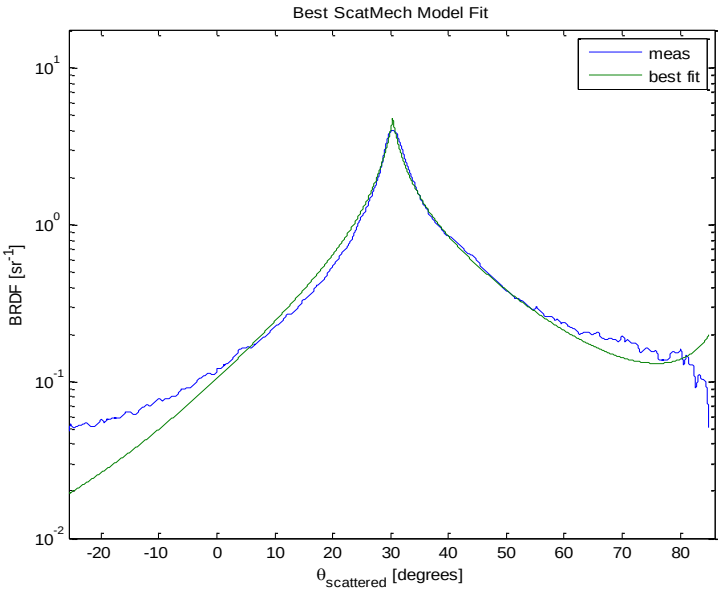

Figure 64. ScatMech model fit to measurement of diffuse aluminum plate with λ=633nm and θ_i=30°.

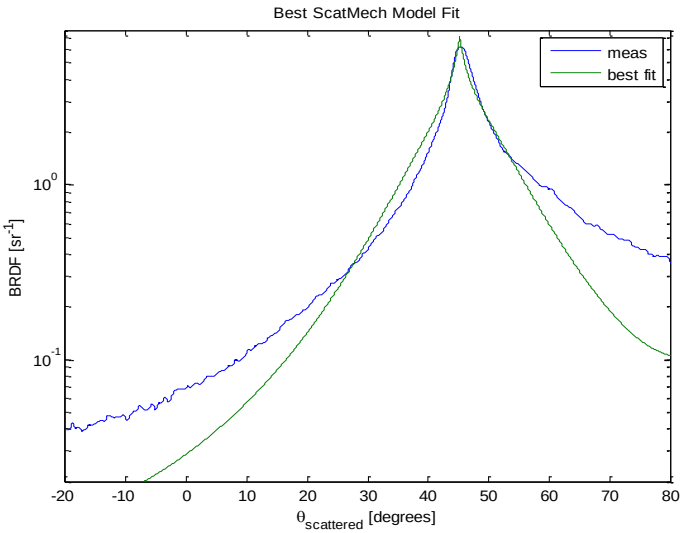

Figure 65. ScatMech model fit to measurement of diffuse aluminum plate with λ=633nm and θ_i=50°.

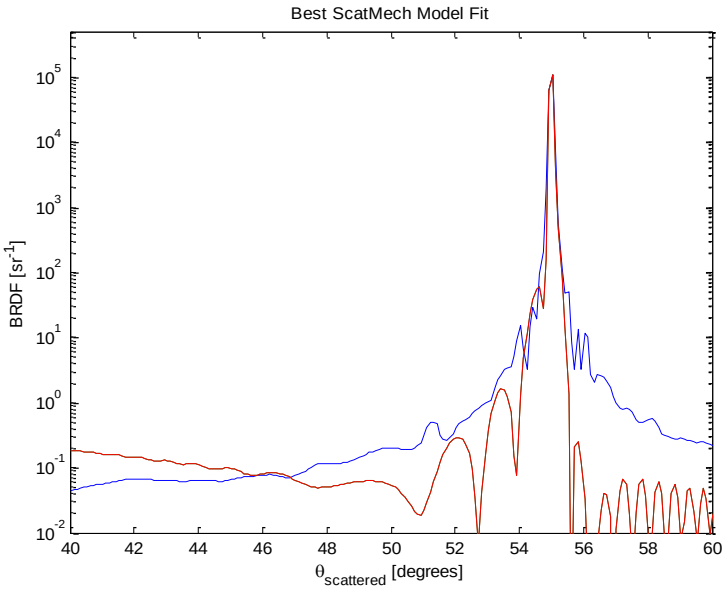

Figure 66. ScatMech model fit (red) to measurement (blue) of SPP structure with λ=4.3μm and θ_i=55°.

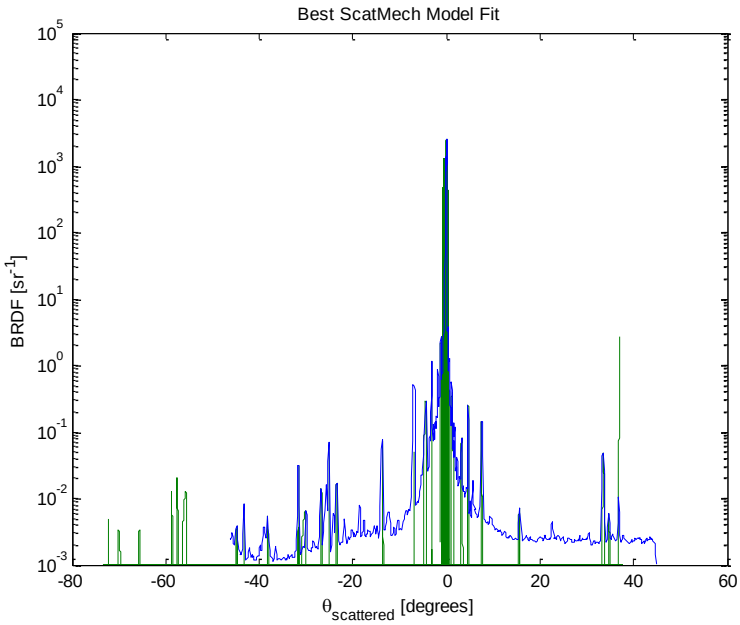

Figure 67. ScatMech model fit (green) to measurement (blue) of GMRF structure with λ=544nm and θ_i=25.7°, note that the θ_i-axis of this plot is centered at the specular angle.

Bibliography

[1] United States Air Force Chief Scientist (AF/ST). "Technology horizons: A vision for air force science & technology during 2010-203". 2010[http://www.af.mil/information/technologyhorizons.asp].

[2] F. Yang, G. Yen and B. T. Cunningham. "Integrated 2D photonic crystal stack filter fabricated using nanoreplica molding," *Optics Express 18(11),* pp. 11846. 2010.

[3] D. W. Dobbs and B. T. Cunningham. "Optically tunable guided-mode resonance filter," *Appl. Opt. 45(28),* pp. 7286. 2006.

[4] D. L. Brundrett, E. N. Glytsis, T. K. Gaylord and J. M. Bendickson. "Effects of modulation strength in guided-mode resonant subwavelength gratings at normal incidence," *Journal of the Optical Society of America A 17(7),* pp. 1221. 2000.

[5] T. Sun and D. Wu. "Guided-mode resonance excitation on multimode planar periodic waveguide," *J. Appl. Phys. 108(6),* pp. 063106. 2010.

[6] P. B. Catrysse and S. Fan. "Propagating plasmonic mode in nanoscale apertures and its implications for extraordinary transmission," *Journal of Nanophotonics 2(1),* pp. 021790. 2008.

[7] H. Fu, Y. Jiang, M. Tsai, S. Lee and Y. Chen. "A thermal emitter with selective wavelength: Based on the coupling between photonic crystals and surface plasmon polaritons," *J. Appl. Phys. 105(3),* pp. 033505. 2009.

[8] J. D. Joannopoulos, S. L. Johnson, J. N. Winn and R. C. Meade. *Photonic Crystals: Molding the Flow of Light* 2008Available: http://www.loc.gov/catdir/enhancements/fy0806/2007061025-b.html.

[9] C. G. Bostan, "dispersion1dPC.m," vol. http://cgbostan.evonet.ro;http://www.mathworks.com/matlabcentral/fileexchange/21810-one-dimensional-photonic-crystal-dispersion-relations;, 2008.

[10] S. A. Maier. *Plasmonics Fundamentals and Applications* 2006.

[11] W. L. Bade. "Drude-Model calculation of dispersion forces. I. general theor," *J. Chem. Phys. 27(6),* pp. 1280-1284.

[12] Y. Teng and E. Stern. "Plasma radiation from metal grating surfaces," *Phys. Rev. Lett. 19(9),* pp. 511-514. 1967.

[13] J. M. Pitarke, V. M. Silkin, E. V. Chulkov and P. M. Echenique. "Theory of surface plasmons and surface-plasmon polaritons," *Reports on Progress in Physics 70(1),* pp. 1-87. 2007; 2006.

[14] H. Raether. *Surface Plasmons on Smooth and Rough Surfaces and on Gratings* (1st ed.) 1988*(1/6/2012).*

[15] Z. Ku, "All-optical metamaterial modulators: Fabrication, simulation and characterization " 2010.

[16] J. E. Kihm, Y. C. Yoon, K. G. Yee, D. J. Park, D. S. Kim, C. Ropers, C. Lienau, J. W. Park, J. Kim and Q. Park. Positive and negative band gaps, rayleigh-wood's anomalies in plasmonic band-gaps structures. Presented at Conference on Lasers and Electro-Optics/Quantum Electronics and Laser Science and Photonic Applications Systems Technologies. 2005, Available: http://www.opticsinfobase.org/abstract.cfm?URI=QELS-2005-QMK6.

[17] T. W. Ebbesen, H. J. Lezec, H. F. Ghaemi, T. Thio and P. A. Wolff. "Extraordinary optical transmission through sub-wavelength hole arrays,". *Nature 391(6668),* pp. 667-669. 1998. Available: http://dx.doi.org/10.1038/35570.

[18] P. B. Catrysse, H. Shin and S. Fan. Propagating modes in subwavelength cylindrical holes *Journal of Vacuum Science & Technology B: Microelectronics and Nanometer Structures 23(6),* pp. 2675. 2005.

[19] C. A. Balanis, *Advanced Engineering Electromagnetics.* Hoboken, NJ: John Wiley & Sons, Inc, 1989.

[20] E. D. Palik. *Handbook of Optical Constants of Solids* (1st ed.) 1997*5*.

[21] R. E. Hummel and P. Wibmann. *Optical Properties of Materials* (1st ed.) 2000*2*.

[22] Lumerical Solutions, "Lumerical Solutions, FDTD Solutions Knowledge Base," vol. 2012, .

[23] S. G. Johnson, "Notes on Perfectly Matched Layers (PMLs)," vol. 2012, pp. 18, 2007.

[24] T. R. Thomas. *Rough Surfaces* (2nd ed.) 1999.

[25] M. W. Hyde, J. D. Schmidt and M. J. Havrilla. "A geometrical optics polarimetric bidirectional reflectance distribution function for dielectric and metallic surfaces," *Optics Express 17(24),* pp. 22138. 2009.

[26] T. A. Germer, "ScatMech," vol. 2012, 2008.

[27] E. Collett. *Field Guide to Polarization* 2005Available: http://www.loc.gov/catdir/toc/ecip059/2005006346.html;.

[28] F. Yang. *Energy transduction in surface photonic crystals* . 2011.

[29] R. Lamott, "Analysis and Application of the Bi-Directional Scatter Distribution Function of Photonic Crystals " vol. 1, 2009.

[30] S. S. Wang and R. Magnusson. "Theory and applications of guided-mode resonance filters," *Appl. Opt. 32(14),* pp. 2606. 1993.

[31] H. Ghaemi, T. Thio, D. Grupp, T. Ebbesen and H. Lezec. "Surface plasmons enhance optical transmission through subwavelength holes," *Physical Review B 58(11),* pp. 6779-6782. 1998.

[32] J. Zoroofchi and J. K. Butler. "Refractive index of n-type gallium arsenide,". *Journal of Applied Physics 44(8),* pp. 3697-3699. 1973.

[33] B. R. Bennett, R. A. Soref and J. A. Del Alamo. "Carrier-induced change in refractive index of InP, GaAs and InGaAsP,". *Quantum Electronics, IEEE Journal of 26(1),* pp. 113-122. 1990.

[34] R. L. Burden and J. D. Faires, *Numerical Analysis.* Belmont, CA: Thomson Brooks/Cole, 2005.

[35] J. Robinson and Y. Rahmat-Samii. "Particle swarm optimization in electromagnetics," *IEEE Transactions on Antennas and Propagation 52(2),* pp. 397-407. 2004.

REPORT DOCUMENTATION PAGE

Form Approved
OMB No. 074-0188

PLEASE DO NOT RETURN YOUR FORM TO THE ABOVE ADDRESS.

1. REPORT DATE *(DD-MM-YYYY)*	2. REPORT TYPE	3. DATES COVERED *(From – To)*
22-03-2012	Master's Thesis	04 Aug 2010-22 Mar 2012

4. TITLE AND SUBTITLE
Measurement Based Model Of The Bidirectional Scatter Distribution Function Of Unspecified Losses In Infrared Micro-Structured Materials

5a. CONTRACT NUMBER

5b. GRANT NUMBER

5c. PROGRAM ELEMENT NUMBER

6. AUTHOR(S)
Sellers, Spencer R. Capt USAF

5d. PROJECT NUMBER
N/A

5e. TASK NUMBER

5f. WORK UNIT NUMBER

7. PERFORMING ORGANIZATION NAMES(S) AND ADDRESS(S)
Air Force Institute of Technology
Graduate School of Engineering and Management (AFIT/EN)
2950 Hobson Way, Building 640
WPAFB OH 45433-7765

8. PERFORMING ORGANIZATION REPORT NUMBER
AFIT/EE.ABET/ENP/12-M02

9. SPONSORING/MONITORING AGENCY NAME(S) AND ADDRESS(ES)
Intentionally Left Blank

10. SPONSOR/MONITOR'S ACRONYM(S)

11. SPONSOR/MONITOR'S REPORT NUMBER(S)

12. DISTRIBUTION/AVAILABILITY STATEMENT
A: APPROVED FOR PUBLIC RELEASE; DISTIBUTION UNLIMITED

13. SUPPLEMENTARY NOTES
This material is declared a work of the U.S. Government and is not subject to copyright protection in the United States.

14. ABSTRACT

The basic physics of nano-/micro-structured materials must be categorized through measurements and simulation to fully understand their scatter dependence on polarization and angle on incidence before they can be considered for war fighter applications. The off-normal incidence and polarization dependant scatter for a guided-mode resonance filter (GMRF) and a surface plasmonic polariton (SPP) extraordinary transmission filter is measured. The measurements are compared to finite-difference time domain (FDTD) simulations. The GMRF is found to exhibit extraordinary angular scatter at the resonant coupled modes. An approximation is developed to predict the dependence of these modes on wavelength, incident angle and polarization. For the SPP extraordinary filter, the lower-order SPP modes and their dependence on incident angle, polarization and grating momentum vector were identified. Full polarimetric spectral transmission was both measured and simulated, giving a Mueller matrix representation of the spectral transmission of the SPP filter. These results demonstrate the dependence on incident angle and polarization of the extraordinary characteristics of two classes of nano-/micro-structured materials.

15. SUBJECT TERMS
Surface Plasmon Polariton (SPP), extraordinary transmission, guided-mode resonance filter (GMRF), Mueller matrix, Lumerical Solutions FDTD

16. SECURITY CLASSIFICATION OF: U			17. LIMITATION OF ABSTRACT	18. NUMBER OF PAGES	19a. NAME OF RESPONSIBLE PERSON
a. REPORT	b. ABSTRACT	c. THIS PAGE			Marciniak, Michael A., Ph.D, AFIT/ENP
U	U	U	SAR	109 Pages	19b. TELEPHONE NUMBER *(Include area code)* (937) 255-6565, x 4529 (michael.marciniak@afit.edu)

Standard Form 298 (Rev. 8-98)
Prescribed by ANSI Std. Z39-18